UNIVERSITY OF CALIFORNIA, SAN DIEGO

Highly Linear SAW-less Receiver Design Techniques for CDMA

A dissertation submitted in partial satisfaction of the
requirements for the degree
Doctor of Philosophy

in

Electrical Engineering (Electronics Circuits and Systems)

by

Nam Soo Kim

Committee in charge:

Lawrence E. Larson, Chair
Peter M. Asbeck
James F. Buckwalter
Ryan Kastner
Tajana Simunic-Rosing

2010

The dissertation of Nam Soo Kim is approved, and it is acceptable in quality and form for publication on microfilm and electronically:

_____

_____

_____

_____

_____

Chair

University of California, San Diego

2010

DEDICATION

To my wife, Ja Ok Koo, and children, Elise and Patrick,
and my parents.

EPIGRAPH

I have not failed. I've just found 10,000 ways that won't work.

Thomas A. Edison

TABLE OF CONTENTS

LIST OF FIGURES

LIST OF TABLES

ACKNOWLEDGEMENTS

First and foremost, I would like to express my most sincere gratitude to my advisor, Professor Lawrence E. Larson, who took me into his research group, supported my research and gave me his moral support, patience and perseverance. I could have never imagined to finish this dissertation without his support. I am indebted to Dr. Aparin whom I had many lengthy discussions with during the formative stages of my research.

I would also like to thank the members of my committee, Professors Peter M. Asbeck, James F. Buckwalter, Tajana Simunic-Rosing, and Ryan Kastner, for their patience and understanding.

I wish to acknowledge all my colleagues for their inspiring discussions and suggestions. I would especially like to acknowledge: Dr. Himanshu Khatri (Qualcomm), Dr. Mahim Ranjan (Qualcomm), Dr. Sanghoon Park (SamSung), Mr. Myungbo Kwak, and Dr. Sean Kim (Intel). I also sincerely thank Professor Sang-gug Lee who lead me into RF IC design field and inspired me to pursue Ph. D. degree.

I would greatly acknowledge my wife Ja Ok Koo, who left no stone unturned to support my efforts ever since our marriage. I am also thankful to my children, Elise and Patrick, for their patience during this research work.

The text of Chapter Two, in part of in full, is a reprint of, N. Kim, V. Aparin, and L. E. Larson, "Analysis of IM_3 asymmetry in MOSFET small-signal amplifiers," submitted to *IEEE Trans. Circuits Syst. I, Reg. Papers* The text of Chapter Three, in part of in full, is a reprint of, N. Kim, V. Aparin, and L. E. Larson, "A resistively degenerated wide-band passive mixer with low noise figure and +60dBm IIP_2 in 0.18μm CMOS," *Proc. IEEE RF Integrated Circuits Symp., RFIC*, 2008, pp. 185-188, N. Kim, V. Aparin, and L. E. Larson, "A resistvely degenerated wideband passive mixer with low noise figure and high IIP_2," *IEEE Trans. Microw. Theory Tech.*, vol. 58, no. 4, pp. 820-830, Apr. 2010. The text of Chapter Four, in part of in full, is a reprint of, N. Kim, V. Aparin, and L. E. Larson, "A highly linear SAW-less CMOS receiver using a mixer with embedded Tx filtering for CDMA," *IEEE Custom Integrated Circuits Conf.*, CICC, 2008, pp. 729-732., N. Kim, V. Aparin, and L. E. Larson, "A highly linear SAW-less CMOS receiver using a mixer with embedded Tx filtering for CDMA," *IEEE J.*

Solid-State Circuits, vol. 44, no. 8, pp. 2126-2137, Aug. 2009.

VITA

1998	B. S. in Semiconductor Science, Dongguk University, South Korea
2000	M. S. in Electrical Engineering, Information and Communication University(Now KAIST), South Korea
2000-2001	RF IC design engineer, Electronics and Telecommunications Research Institute (ETRI), South Korea
2001-2002	RF/Analog IC design engineer, Ashvattha Semiconductor, FL, United States
2002-present	RF/Analog IC design engineer, Qualcomm, CA, United States
2007-2010	Ph. D. in Electrical and Computer Engineering, University of California, San Diego, CA, United States

PUBLICATIONS

N. Kim, V. Aparin, and L. E. Larson, "A resistively degenerated wide-band passive mixer with low noise figure and +60dBm IIP_2 in 0.18μm CMOS," *Proc. IEEE RF Integrated Circuits Symp., RFIC*, 2008, pp. 185-188.

N. Kim, V. Aparin, and L. E. Larson, "A highly linear SAW-less CMOS receiver using a mixer with embedded Tx filtering for CDMA," *IEEE Custom Integrated Circuits Conf.*, CICC, 2008, pp. 729-732.

N. Kim, V. Aparin, and L. E. Larson, "A highly linear SAW-less CMOS receiver using a mixer with embedded Tx filtering for CDMA," *IEEE J. Solid-State Circuits*, vol. 44, no. 8, pp. 2126-2137, Aug. 2009

N. Kim, V. Aparin, and L. E. Larson, "A resistvely degenerated wideband passive mixer with low noise figure and high IIP_2," *IEEE Trans. Microw. Theory Tech.*, vol. 58, no. 4, pp. 820-830, Apr. 2010

N. Kim, V. Aparin, and L. E. Larson, "Analysis of IM_3 asymmetry in MOSFET small-signal amplifiers," submitted to *IEEE Trans. Circuits Syst. I, Reg. Papers*

ABSTRACT OF THE DISSERTATION

Highly Linear SAW-less Receiver Design Techniques for CDMA

by

Nam Soo Kim

Doctor of Philosophy in Electrical Engineering (Electronics Circuits and Systems)

University of California San Diego, 2010

Lawrence E. Larson, Chair

The proliferation of wireless communication systems has resulted in ever demanding low-cost handsets. The wide adoption of the Homodyne receiver system is a consequence of industrial requirements. Yet, the inter-stage high-Q filter, rejecting the leaked transmit (Tx) signal between the LNA and mixer, is prevalent in frequency division duplexed (FDD) receivers, so that the amplified Tx signal does not corrupt overall receiver performance.

This research is focused on the method of eliminating the inter-stage high-Q filter by adopting new circuit topologies. The main consideration is given to mixer design, since the mixer needs to be either highly linear or to reject the Tx signal by itself. First, a highly linear passive mixer with simple degeneration, in order to improve noise figure (NF) and IIP_2 performance, is researched. A receiver using a proposed passive mixer with degeneration is fabricated in a 0.18 μm Si CMOS process. The operating frequency is from 1.55 to 2.3 GHz. The measured performance shows less than 9.5dB double-sideband (DSB) NF, more than 22dB voltage gain, better than +50dBm uncalibrated IIP_2, and higher than +7dBm of IIP_3, while consuming only 10mW from a 2 V supply.

In the second approach, an embedded filtering passive (EFP) mixer is researched. Unlike a normal passive mixer, the EFP mixer performs narrow band downconversion, which provides filtering for the Tx signal. A complete receiver, consisting of LNA, EFP mixer, transimpedance amplifier (TIA), and local oscillator (LO) path, is fabricated in

a 0.18 μm Si CMOS process. The receiver IC exhibits more than +60dBm of Rx IIP_2, 2.4dB Rx noise figure, and +77dB of triple beat (TB) with 45 MHz offset transmit leakage at 900 MHz Rx frequency while consuming only 18mA from a 2.1 V supply. The proposed receiver IC shows an additional 15dB Tx rejection compared to a conventional receiver. The additional Tx rejection improved the IIP_2 by 10dB and the TB by 30dB.

Chapter 1

Introduction

Many wireless communication systems are based on the concept of a cellular network. A cellular network is a radio network made up of a number of cells, each served by at least one fixed-location transceiver known as a cell site or base station. When joined together these cells provide radio coverage over a wide geographic area. This enables a large number of portable transceivers (mobile phones) to communicate with each other in the network, via base stations, even if some of the transceivers are moving through more than one cell during transmission. A graphical illustration of a typical celluar network is shown in Fig. 1.1.

Minimum Detectable Signal

In wireless communication systems, the signal transfer from the base station to the mobile phones, a.k.a User Equipment (UE), is called the *forward link* and the link from the UE to the base station is called the *reverse link*. A UE has to send the maximum output power to reach the base station when the UE is located at the edge of the cell coverage. This situation is shown in Fig. 1.2. This situation is the scenario used to define the minimum detectable signal (MDS) in wireless network standards.

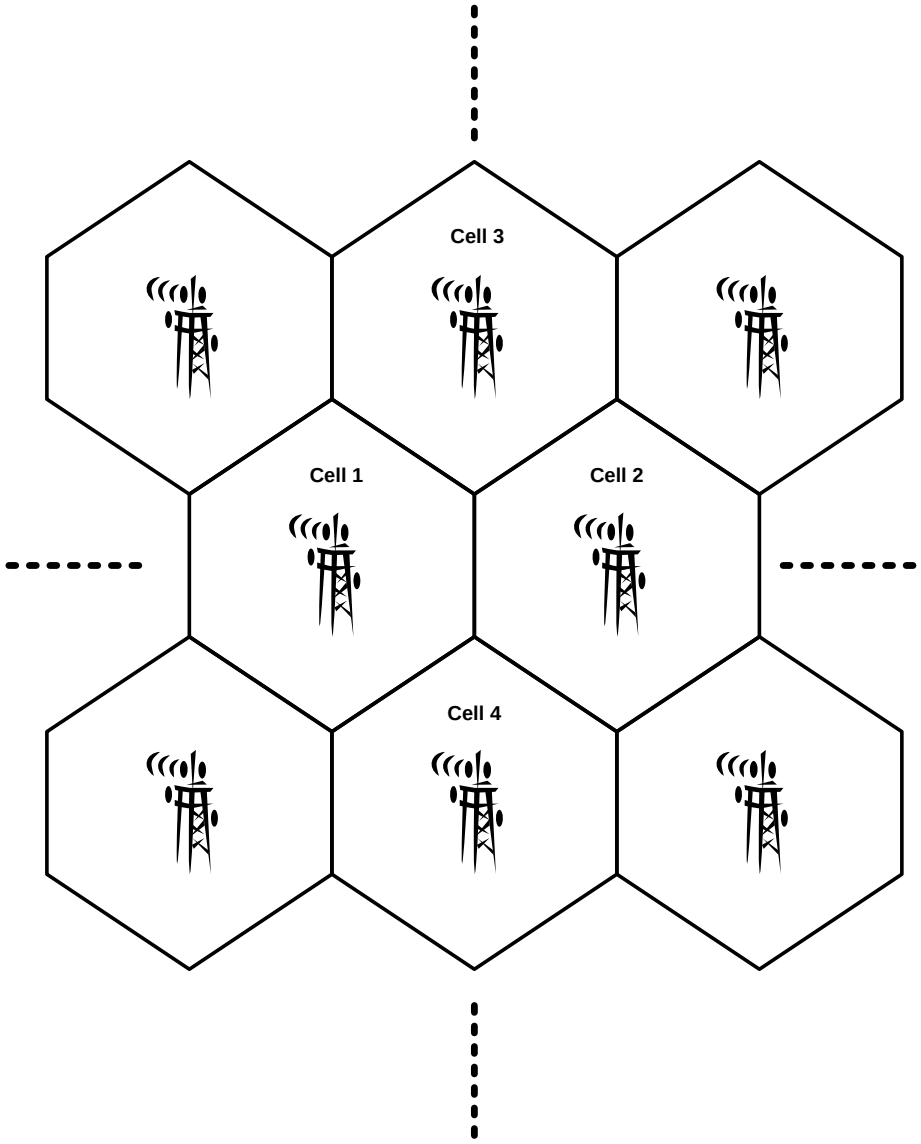

Figure 1.1: Example of celluar network wireless communication system.

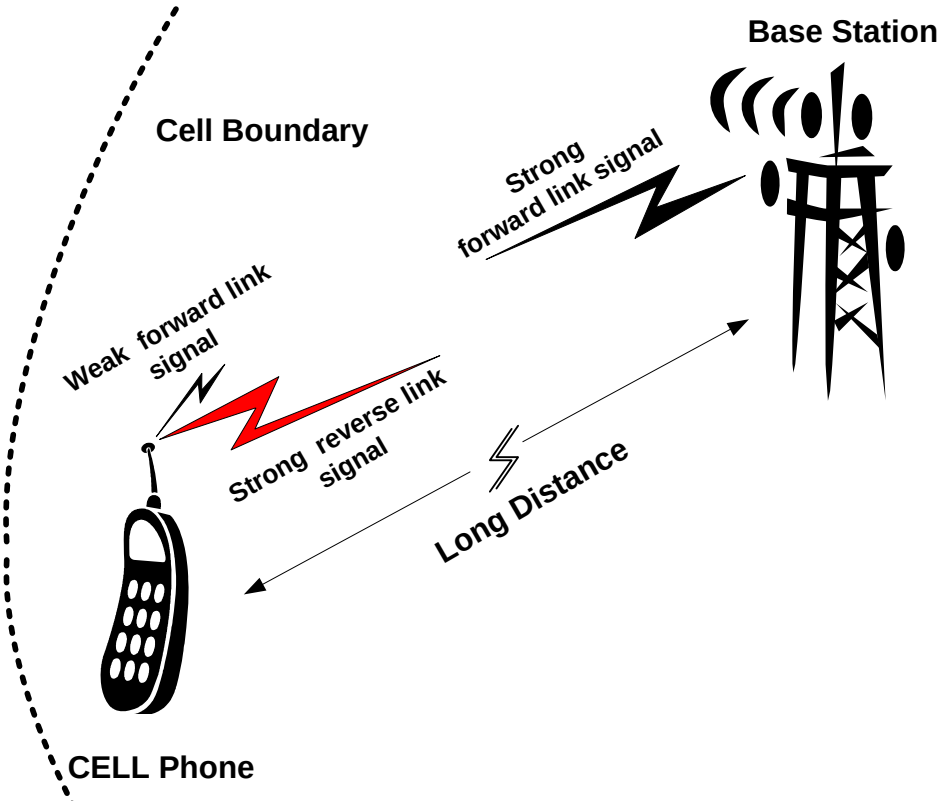

Figure 1.2: Situation where UE is located at the edge of the cell.

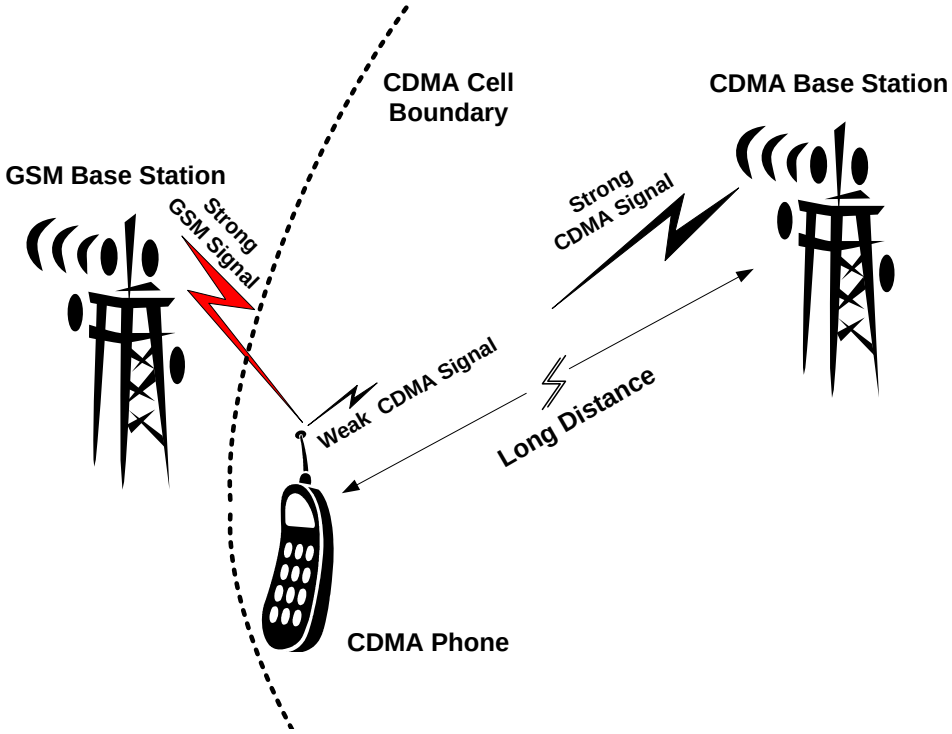

Figure 1.3: Situation where CDMA UE is located at the edge of the cell with nearby GSM base station.

Blocker/Jammer Scenario

There are a number of different digital cellular technologies, including: Advanced Mobile Phone Service (AMPS), Global System for Mobile Communications (GSM), General Packet Radio Service (GPRS), Code Division Multiple Access (CDMA) , Wideband Code Division Multiple Access (WCDMA) or Universal Mobile Telecommunications System (UMTS), Evolution-Data Optimized (EV-DO), Enhanced Data Rate for GSM Evolution (EDGE), 3GSM, UMTS Long Term Evolution (LTE), Worldwide Interoperability for Microwave Access (WiMAX), Digital Enhanced Cordless Telecommunications (DECT), Digital AMPS (IS-136/TDMA), and Integrated Digital Enhanced Network (iDEN). These systems can coexist in the same geographical area, causing a jamming environment for radio systems. A great example of this problem is CDMA and GSM coexistence in United States. Consider a GSM base station, which likely sends the maximum forward link power to reach the edge of the cell, while a CDMA UE is

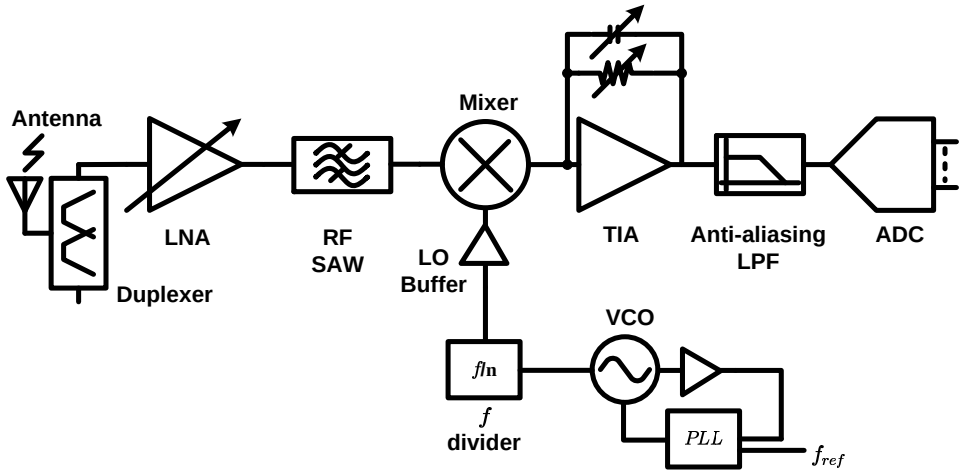

Figure 1.4: A typical zero-IF receiver architecture.

located at the edge of the CDMA cell converage. This situation is shown in Fig. 1.3. The blocker, or jammer, performance requirements in the wireless standards are based on this coexistence scenario.

1.1 CDMA RF Receiver

Zero-IF RF front-end architectures [6–8] are attractive for cellular systems due to their lower cost and Bill-of-Material (BOM). But the external SAW filter after the LNA stage has been an essential component of cellular systems for several reasons. The two main reasons for using an external SAW filter in full duplex communication systems, like CDMA and WCDMA, are the Triple-Beat (TB) and IIP_2 performance requirements at the transmit (Tx) offset frequency. A typical zero-IF receiver is shown in Fig. 1.4.

The Tx power can leak to the LNA input due to the finite duplexer isolation between the receive (Rx) and Tx band. The typical duplexer isolation is 55dB in the CDMA Cellular band, and the maximum Tx power can be as high as +27dBm, resulting in -28dBm of Tx power at the Rx input port. This strong Tx power can cause cross-modulation distortion (XMD) [9]. This distortion is usually dominated by the LNA performance, since the Tx rejection of an external SAW filter reduces the XMD requirement of the mixer following the LNA. More importantly, the reduced Tx power at the

mixer input reduces the mixer IIP_2 requirement at the Tx offset frequency, since the second-order distortion at the Tx frequency offset can increase the noise floor of the receiver in a Zero-IF system.

1.2 SAW-less Receiver

A SAW-less receiver system is desirable, since it eliminates the expensive SAW filter as well as the external matching components between the LNA output and mixer input. In addition, the number of pins can be reduced, since the LNA and mixer can be directly connected inside of the IC. There have been several efforts to implement a SAW-less full-duplex receiver systems.

Active Tx canceller

Recently, the active blocker/Tx cancellation became popular due to the lower area penalty compared to the passive on-chip LC filters and advances in CMOS scaling [1, 2, 10–13]. A Tx canceller for CDMA systems was reported in [1], which used an LMS adaptive filter requiring up/down conversion mixers and integrators in the loop, as shown in Fig. 1.5. This method suffers from several performance problems. First, the noise figure (NF) of the receiver is degraded due to the operation of the LMS loop. Second, the rejection varies depending on the group delay of the external matching network or coupler. The delay between duplexer and external coupler can not be matched, since the Tx reference signal is coupled before the duplexer. Third, the XMD performance of the overall system can be degraded due to the nonlinearity of the LMS loop itself. To overcome the group delay dependency, Aparin [2] introduced a low-pass feedback cancelling architecture, as shown in Fig. 1.6. Here the reference signal is the Tx LO instead of the coupled Tx signal from the Tx path. But the system has inherent stability issues due to the nature of feedback system. Moreover, the amount of rejection is limited due to the trade-off between the loop gain and in-band signal loss. To overcome the stability issue in the feedback system, Darabi [12] introduced a feedforward cancelling technique. The main drawback of using feedforward architecture is that the cancellation loop gain has to match with the main path gain. The substraction operation will add am-

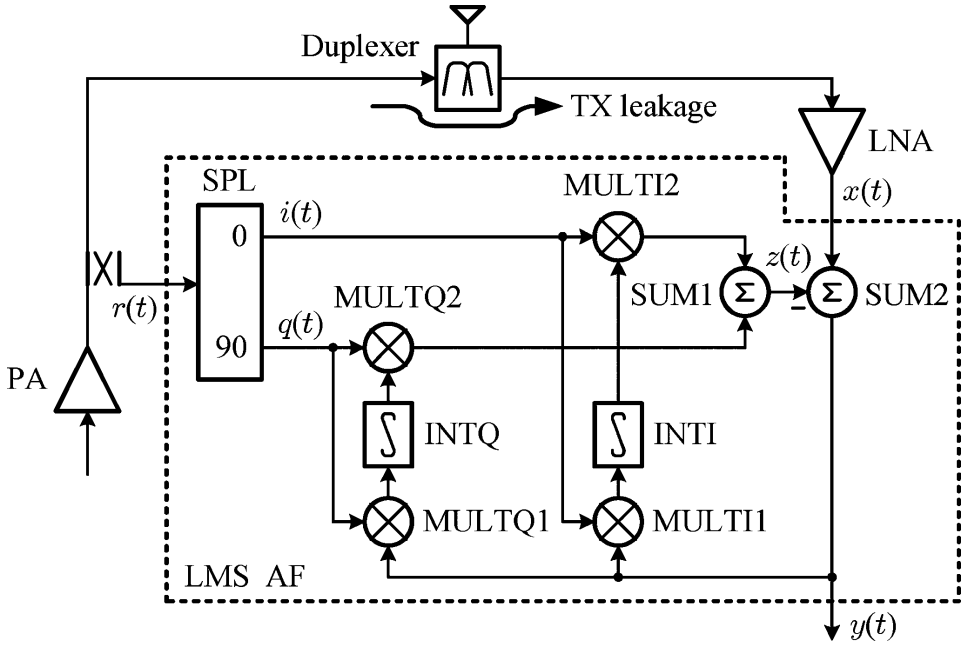

Figure 1.5: LMS adaptive filter architecture used in a CDMA transceiver [1].

plitude, instead of cancelling it, if the cancellation loop gain is higher than main path. The cancellation will not be enough, if the cancellation loop gain is not close enough to the main path gain, due to the substraction. This is why the feedback configuration is used widely, even though it has stability issues.

There are four possible configurations to build a feedback/feedforward active canceller, as shown in Fig. 1.7. Fig. 1.7(a) utilizes feedforward cancelling with the Tx LO and a LPF. This architecture has the advantage of cancelling higher offset blockers, such as Tx leakage, compared to Fig. 1.7(b) [12]. Designing a BPF centered at a far frequency offset is challenging and power hungry. But Fig. 1.7(a) can handle this far frequency offset, since the blocker or Tx leakage will be downconverted to DC, rather than the Rx-Tx offset frequency. Though it can handle the far frequency offset easily, Fig. 1.7(a) has to route the Tx LO from the Tx block, which can cause more current consumption depending on IC layout. For the feedback system, the same advantages and disadvantages will apply between using the Tx LO and the Rx LO. The time domain

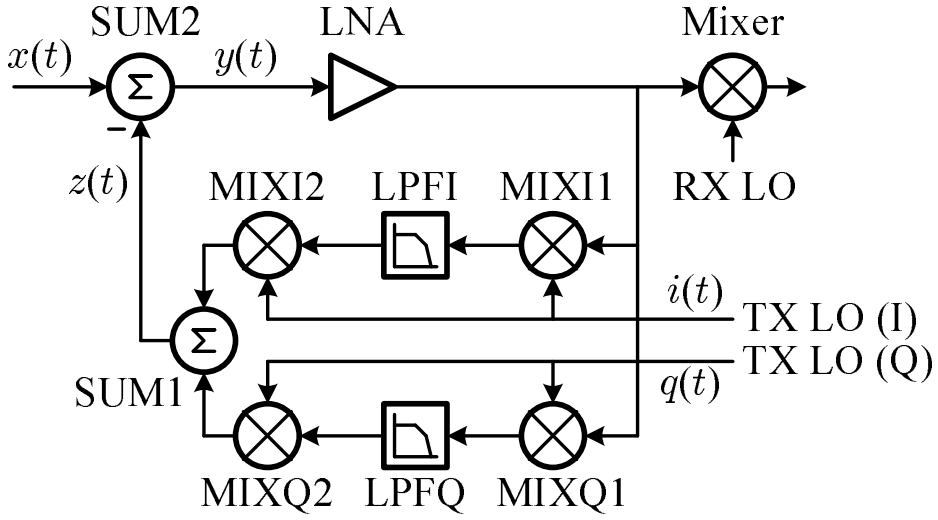

Figure 1.6: Feedback filtering architecture used in a W/CDMA transceiver [2].

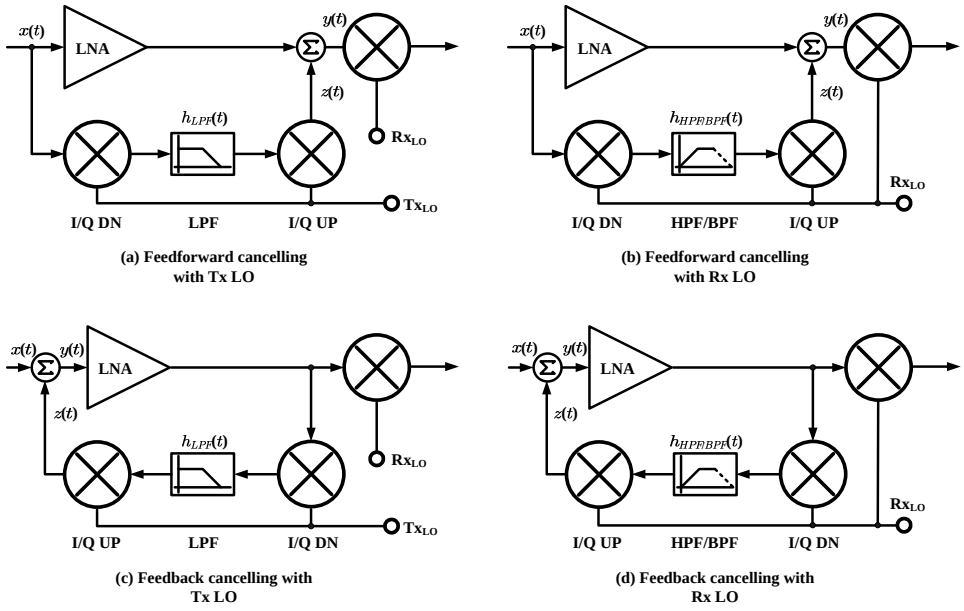

Figure 1.7: Four possilbe active canceller configurations. (a) Feedforward cancelling with Tx LO and LPF. (b) Feedforward cancelling with Rx LO and HPF/BPF. (c) Feedback cancelling with Tx LO and LPF. (d) Feedback cancelling with Rx LO and HPF/BPF.

mathematical model for feedforward and feedback system can be derived from Fig. 1.7. Using the convolution theorem and trigonometric identities,

$$y_{\text{ff}}(t) = G_{\text{LNA}} \cdot x(t) - G_{\text{canc}} \cdot \int x(\tau) \cdot h_{\text{L/H/BPF}}(t-\tau) \cdot \cos\left(\omega_{\text{Tx/Rx,LO}}[t-\tau]\right) d\tau \quad (1.1a)$$

$$y_{\text{fb}}(t) = x(t) - G_{\text{LNA}} \cdot G_{\text{canc}} \int y(\tau) \cdot h_{\text{L/H/BPF}}(t-\tau) \cdot \cos\left(\omega_{\text{Tx/Rx,LO}}[t-\tau]\right) d\tau \quad (1.1b)$$

where, $y_{\text{ff}}(t)$ is the time domain output signal from feedforward architecture, $y_{\text{fb}}(t)$ is the time domain output signal from feedback architecture, $x(t)$ is the input signal, G_{LNA} is the gain of the LNA, G_{canc} is the loop gain from the first downconverter to the last upconverter, $h_{\text{L/H/BPF}}(t)$ is the impulse response of LPF, HPF, or BPF, and $\omega_{\text{Tx/Rx,LO}}$ is the Tx or Rx LO frequency. By taking the Laplace Transform, (1.1) can be expressed in the frequency domain as

$$\frac{Y_{\text{ff}}(s)}{X(s)} = G_{\text{LNA}} - G_{\text{canc}} \cdot H_{\text{L/H/BPF}}\left(s \pm j\omega_{\text{Tx/RxLO}}\right) \quad (1.2a)$$

$$\frac{Y_{\text{fb}}(s)}{X(s)} = \frac{1}{1 + G_{\text{LNA}} \cdot G_{\text{canc}} \cdot H_{\text{L/H/BPF}}\left(s \pm j\omega_{\text{Tx/RxLO}}\right)} \quad (1.2b)$$

The frequecy responses for Tx LO (LPF) and Rx LO (H/BPF) are shown in Fig. 1.8. Both feedforward and feedback will have similar behavior, except for the amount of cancellation, since the feedforward is direct substraction and feedback is attenuation. As can be seen, the Tx LO case exhibits single-side cancellation due to the direct down/up conversion, while the Rx LO shows double-side cancellation due to the IF down/up conversion.

The trade-off between the loop gain and in-band signal loss is a common issue in feedforward and feedback cancellation. Fig. 1.9 shows both Tx LO (LPF) and Rx LO (BPF) cases. Fig. 1.9 illustrates an example where the Rx-Tx separation is 45MHz (US CELL band), 20dB loop gain (either feedforward or feedback), and 2MHz signal BW. As can be seen, the Rx path will be attenuated by only 13dB before the feedback or feedforward signal is subtracted. This implies that, when the loop is closed, the in-band gain will be lost by 2.2dB in feedforward and 1.75dB in feedback architecture,

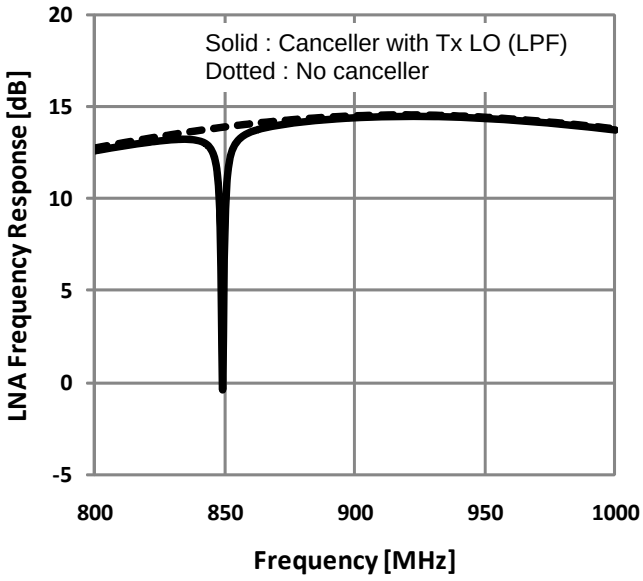

(a) Frequency response with Tx LO (LPF) canceller

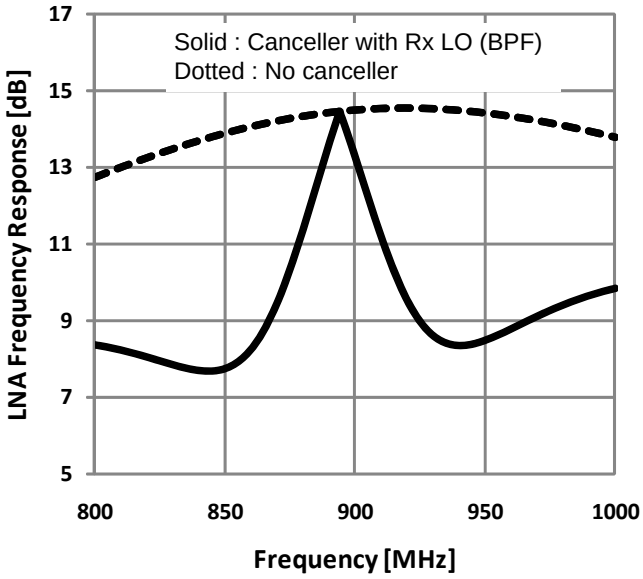

(b) Frequency response with Rx LO (BPF) canceller

Figure 1.8: Tx canceller frequency response. (a) LNA + canceller with Tx LO and LPF. (b) LNA + canceller with Rx LO and BPF.

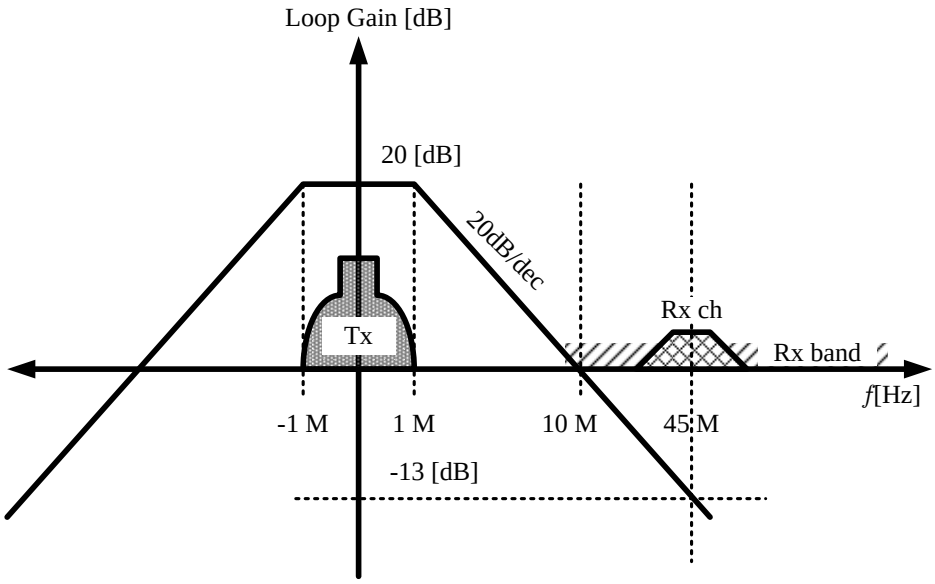

(a) Tx LO (LPF) case

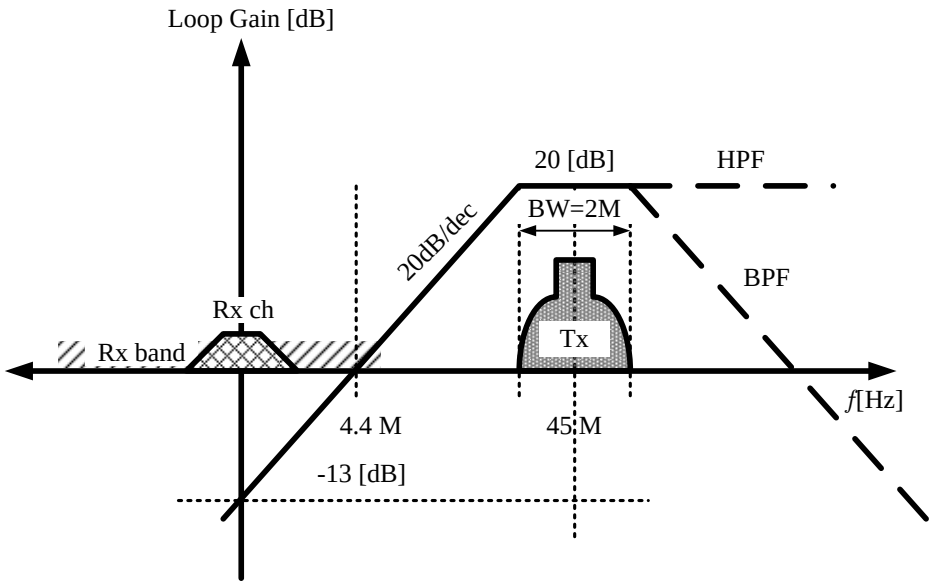

(b) Rx LO (HPF/BPF) case

Figure 1.9: Illustration of the trade-off between loop gain and in-band signal loss. (a) LNA + canceller with Tx LO and LPF. (b) LNA + canceller with Rx LO and BPF/HPF.

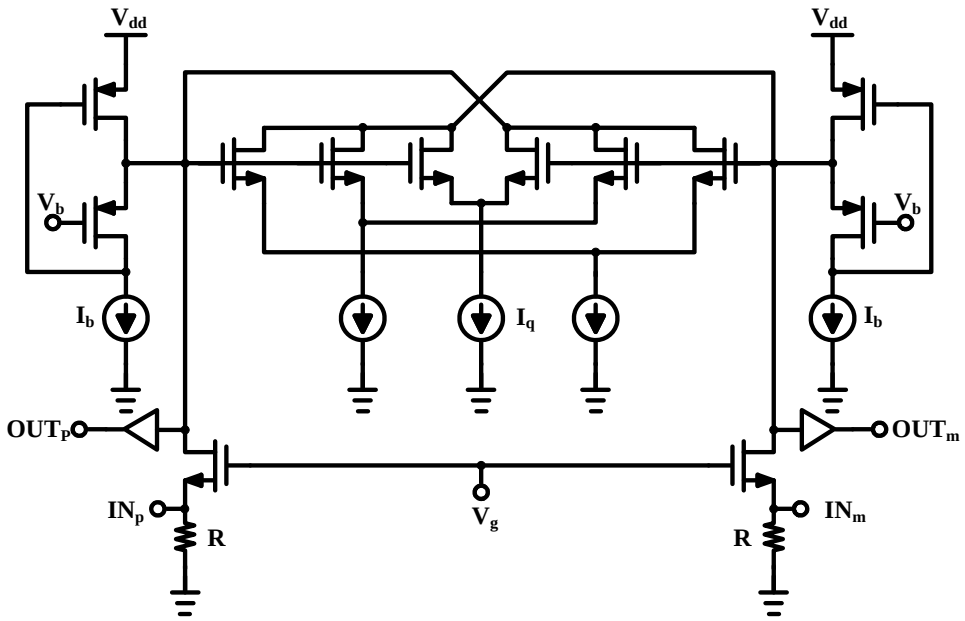

Figure 1.10: RF bandpass filter using active inductor [3].

respectively. This becomes more critical with wide bandwidth applications. This is a main drawback of using active canceller either in feedback or feedforward manner.

Passive Filtering

An on-chip Tx rejection band-pass filter using bond-wire inductors was reported for a WCDMA system in [14]. This method has benefits of saving area compared to an on-chip inductor and increasing the selectivity of the filter due to the high-Q of the bond-wire. But this method may have limited feasibility in real production due to bond-wire variations. There are many monolithic LC filters implemented with Q-enhancement techniques [15–17]. But all of these approaches suffer from large area and poor linearity performance. Wu et. al [3] implmented an on-chip band-pass filter using active inductor to save area, as shown in Fig. 1.10. But it has high insertion loss and increased noise figure penalty, consequently.

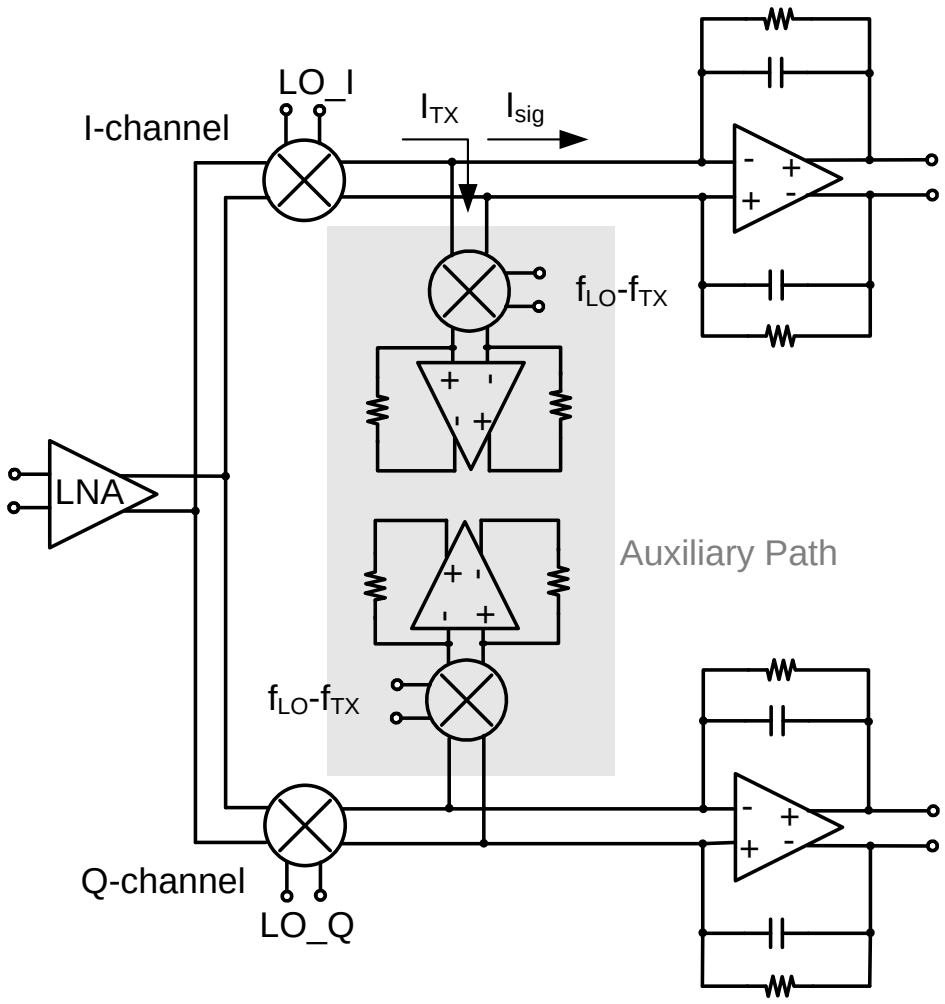

Figure 1.11: WCDMA SAW-less receiver with frequency transformed notch [4].

Frequency Transformed Active Notch

Khatri et. al [4] introduced a new active notch filtering technique by using impedance frequency transformation, as shown in Fig. 1.11. This approach relies on the impedance ratio between the main path TIA input impedance at Tx offset and the auxiliary path TIA input impedance at DC. This approach suffers from the high noise figure penalty due to the auxiliary path TIA noise folding.

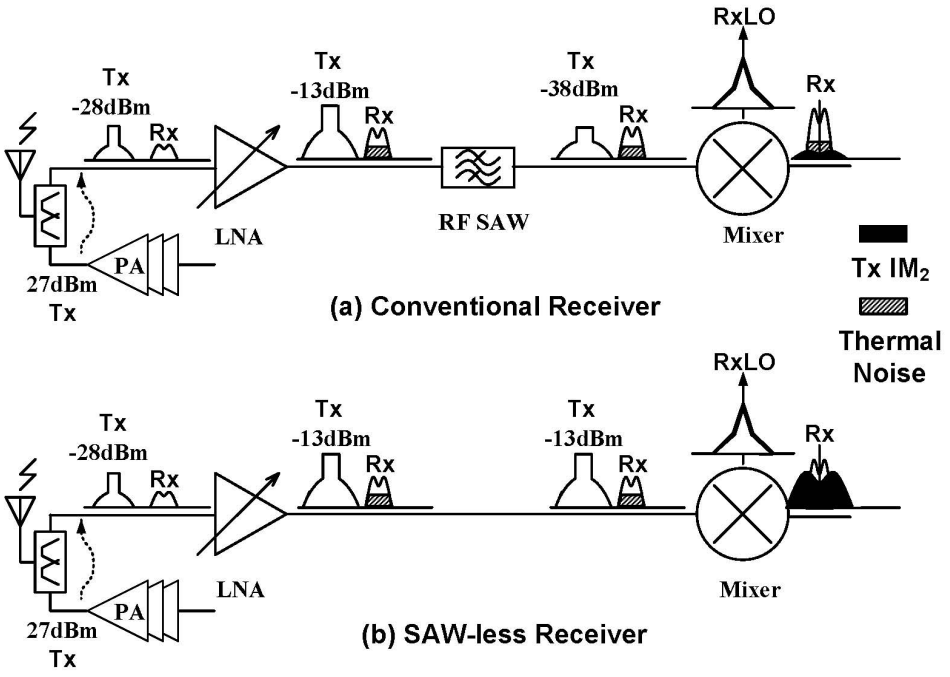

Figure 1.12: Tx IM_2 issue in receiver system (a) Conventional receiver. (b) SAW-less receiver.

1.3 SAW-less Receiver Specification

Receiver Sensitivity Calculation

A conventional Zero-IF receiver in a full-duplex communication system is shown in Fig. 1.12(a). The received Rx signal at the antenna passes through the duplexer, which has approximately 2dB insertion loss and, therefore, degrades the SNR by 2dB. In practice, the total front-end loss can be as high as 3dB including antenna loss, duplexer insertion loss, and transmission line loss. Therefore, assuming the NF of the receiver is 2dB, the total receiver NF referred to the antenna is 5dB. The background thermal noise in the 1.25MHz bandwidth CDMA system is approximately -113dBm. The sensitivity (the minimum detectable signal power) can be calculated as

$$\text{Sensitivity}\,(\text{dBm}) = 10\cdot\log_{10}\left[K\cdot T\cdot B\cdot 10^{3}\cdot 10^{\text{NF}_{\text{ant}}/10}\right](\text{dBm})+\text{CNR}\,(\text{dB}) \quad (1.3)$$

Table 1.1: Test Parameters for CDMA Receiver Sensitivity [5]

Parameter	Units	Value
$\hat{\mathrm{I}}_{\mathrm{or}}$	dBm/1.23MHz	-104
$\frac{\text{Traffic } \mathrm{E_C}}{\mathrm{I_{or}}}$		$10^{-15.6/10}$
Data Rate (DR)	bps	9600
$\frac{\text{Traffic } \mathrm{E_b}}{\mathrm{N_t}}$		$10^{4.5/10}$
Spreading Rate (SR)	cps	1.2288×10^6
Frame Error Rate (FER)	%	0.5

where K is Boltzmann's constant, T is absolute temperature, B is the bandwidth of the system, $\mathrm{NF_{ant}}$ is the noise figure of the receiver system at the antenna, and CNR is carrier-to-noise ratio required at the output of the receiver. The CNR for a CDMA system can be calculated from the standard [18]. The required minimum performance for the *Sensitivity* test is summarized in Table 1.1. $\hat{\mathrm{I}}_{\mathrm{or}}$ is the received power spectral density of the forward link as measured at the mobile station antenna connector. Traffic $\mathrm{E_C}/\mathrm{I_{or}}$ is the ratio of the energy per PN chip in the traffic channel to the total power of the transmitted signal at the base station antenna connector. Traffic $\mathrm{E_b}/\mathrm{N_t}$ is the ratio of the energy per bit in the traffic channel to the effective noise power spectral density. CNR in communication systems can be expressed from the definition.

$$\mathrm{CNR\,(dB)} = 10 \cdot \log_{10}\left[\frac{\mathrm{E_b}}{\mathrm{n_o}}\right] + 10 \cdot \log_{10}\left[\frac{\mathrm{R_b}}{\mathrm{BW}}\right] \tag{1.4}$$

where $\mathrm{E_b}$ is energy per bit, $\mathrm{n_o}$ is noise density within the signal bandwidth, and $\mathrm{R_b}$ is bit rate. In a CDMA system, (1.4) can be modified to (1.5),

$$\mathrm{CNR_{CDMA}\,(dB)} = 10 \cdot \log_{10}\left[\frac{\text{Traffic } \mathrm{E_b}}{\mathrm{N_t} \times \left(\frac{\text{Traffic } \mathrm{E_C}}{\mathrm{I_{or}}}\right)}\right] + 10 \cdot \log_{10}\left[\frac{\mathrm{DR}}{\mathrm{BW}}\right] \tag{1.5}$$

Furthermore, the BW is the same as the spreading rate (SR) in CDMA, which makes (1.5)

$$\begin{aligned}\mathrm{CNR_{CDMA}\,(dB)} &= 10\cdot\log_{10}\left[\frac{\text{Traffic }\mathrm{E_b}}{\mathrm{N_t}\times\left(\frac{\text{Traffic }\mathrm{E_C}}{\mathrm{I_{or}}}\right)}\right]+10\cdot\log_{10}\left[\frac{\mathrm{DR}}{\mathrm{SR}}\right]\\ &= 10\cdot\log_{10}\left[\frac{\text{Traffic }\mathrm{E_b}}{\mathrm{N_t}\times\left(\frac{\text{Traffic }\mathrm{E_C}}{\mathrm{I_{or}}}\right)}\right]+10\cdot\log_{10}\left[\frac{1}{\mathrm{P_G}}\right] \qquad (1.6)\end{aligned}$$

where $\mathrm{P_G}$ is the processing gain, which is SR/DR = 128. Therefore, the CNR for CDMA receiver system is

$$\begin{aligned}\mathrm{CNR_{CDMA}\,(dB)} &= 10\cdot\log_{10}\left[10^{4.5/10}\times 10^{15.6/10}\right]+10\cdot\log_{10}\left[\frac{1}{128}\right]\\ &= 20.1-21.1=-1\,[\mathrm{dB}] \qquad (1.7)\end{aligned}$$

Inserting (1.7) to (1.3) and using 5dB antenna referred receiver NF with -113dBm integrated thermal noise, the sensitivity of the CDMA receiver system is -109dBm, which is 5dB better than the minimum requirement from the standard. This 5dB margin is to account for the variations of process, voltage, and temperature (a.k.a PVT variation) during manufacturing and use.

Sensitivity with Tx $\mathrm{IM_2}$ Distortion

In the above calculation, the effect of second-order intermodulation ($\mathrm{IM_2}$) due to the Tx leakage is ignored, since the inter-stage SAW filter between the LNA output and the mixer input provides 25dB of Tx rejection, so that the $\mathrm{IM_2}$ distortion generated by the mixer will be below the noise floor.

The definition of nth order output intercept point and input intercept point are given by

$$\mathrm{OIP_n} = \mathrm{P_{out}} + \frac{\mathrm{P_{out}}-\mathrm{P_{IMo,n}}}{\mathrm{n}-1} \qquad (1.8a)$$

$$\mathrm{IIP_n} = \mathrm{P_{in}} + \frac{\mathrm{P_{out}}-\mathrm{P_{IMo,n}}}{\mathrm{n}-1} \qquad (1.8b)$$

where $\mathrm{P_{IMo,n}}$ is nth order distortion power at the output and $\mathrm{P_{out}}$ is the fundamental tone output power. By inserting (1.8a) into (1.8b), the input referred nth order intercept point

can be given as

$$\mathrm{IIP_n} = \mathrm{OIP_n} - \mathrm{G} \tag{1.9}$$

where G is the gain (in dB). The other way of expressing the input referred nth order intercept point is

$$\mathrm{IIP_n} = \mathrm{P_{in}} + \frac{\mathrm{P_{in}} - \mathrm{P_{IMi,n}}}{\mathrm{n} - 1} \tag{1.10}$$

where $\mathrm{P_{IMi,n}}$ is input referred nth order intermodulation distortion power. From (1.8b) and (1.10), the input referred nth order intermodulation distortion can be calculated.

$$\mathrm{P_{IMi,n}} = \mathrm{P_{IMo,n}} - \mathrm{G} \tag{1.11}$$

Therefore, any nth order input referred intercept point or intemodulation power can be calculated by simply subtracting the gain from the output intercept point or intemodulation power. This results is very useful for cascaded system calculation. For example, the mixer $\mathrm{IIP_2}$ performance can be thought of as the LNA $\mathrm{OIP_2}$, so that the LNA input referred mixer $\mathrm{IIP_2}$ value can be easily calculated by subtracting LNA gain. From (1.10), the other $\mathrm{P_{IMi,n}}$ expression can be shown as

$$\mathrm{P_{IMi,n}} = (\mathrm{n} - 1) \cdot (\mathrm{P_{in}} - \mathrm{IIP_n}) + \mathrm{P_{in}} \tag{1.12}$$

Due to the filtering action of the SAW filter, the LNA input referred Tx power for the mixer $\mathrm{IIP_2}$ test can be calculated as

$$\mathrm{P_{Tx,referred}}\,(\mathrm{dBm}) = \mathrm{P_{Tx}}\,(\mathrm{dBm}) - \mathrm{L_{SAW}}\,(\mathrm{dB}) \tag{1.13}$$

where $\mathrm{P_{Tx}}$ is the applied Tx power level at the LNA input, $\mathrm{P_{Tx,referred}}$ is the equivalent input referred power at the Tx offset, and $\mathrm{L_{SAW}}$ is the SAW filter rejection at the Tx offset. The LNA input referred $\mathrm{IM_2}$ power due to mixer distortion can be calculated from (1.12)

$$\mathrm{P_{IMi,Tx}}\,(\mathrm{dBm}) = 2 \cdot \mathrm{P_{Tx,referred}}\,(\mathrm{dBm}) - \mathrm{IIP_{2,LNAreferred}}\,(\mathrm{dBm}) \tag{1.14}$$

where $\mathrm{IIP_{2,LNAreferred}}$ is the $\mathrm{IIP_2}$ of the receiver at the Tx offset. For example, by inserting (1.13) into (1.14), and using -31dBm of single tone Tx leakage power and a total

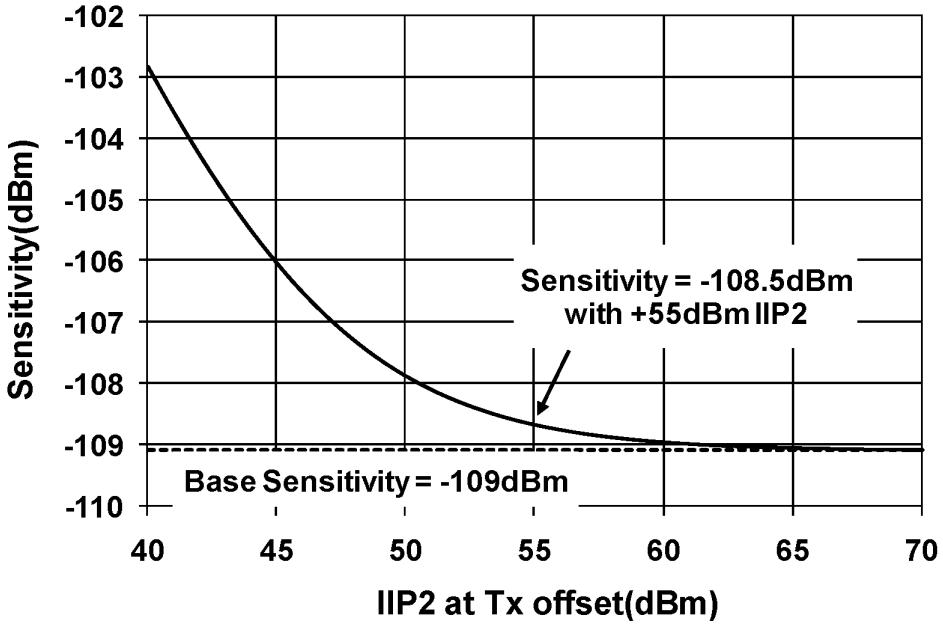

Figure 1.13: Tx IIP_2 perfomance versus sensitivity.

two-tone Tx power of -28dBm, 25dB of SAW Tx rejection, and +35dBm LNA input referred IIP_2, the resulting LNA input referred IM_2 power is calculated to be -147dBm, which is negligible compared to the Rx noise floor of -108dBm.

However, the system has a more challenging Tx IIP_2requirement if the SAW filter is removed, due to the lack of rejection at the Tx frequency, as shown in Fig. 1.12(b). From (1.13) and (1.14) and the same conditions described above, it can be shown that the IM_2 distortion referred to the LNA input is -97dBm, which is above the -108dBm noise floor. Ideally, the IM_2 distortion level should be 9dB below the noise floor, so as not to increase it by more than 0.5dB. This sets the maximum IM_2 distortion level to be -117dBm, resulting in a +55dBm of LNA input referred mixer IIP_2 requirement from(1.14) if no SAW filter is employed, which is extremely challenging due to the high LNA gain (usually higher than 15dB) at the Tx frequency. The sensitivity of the SAW-less receiver system can be calculated from (1.15), including the effects of Tx IM_2 distortion.

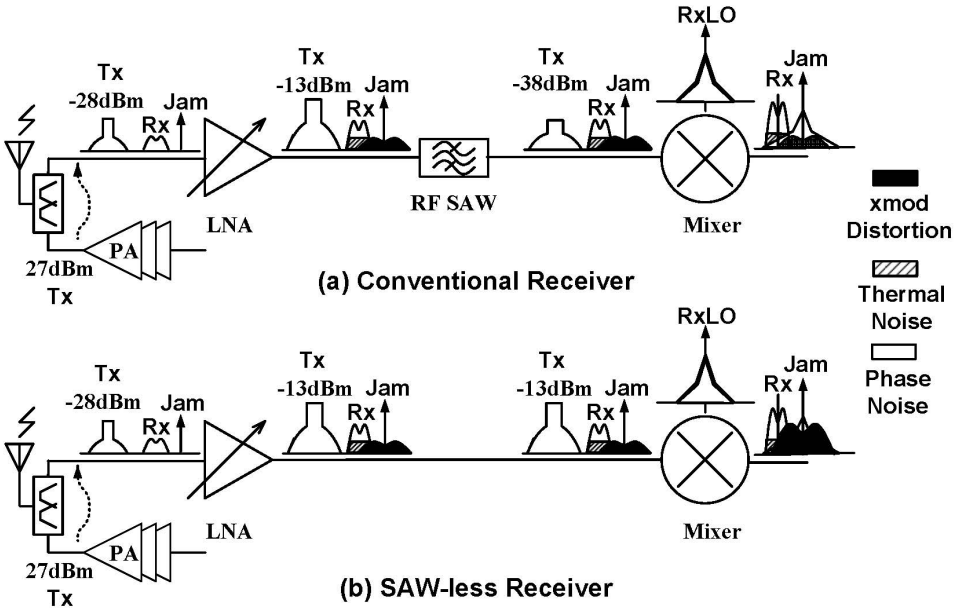

Figure 1.14: STD issue in receiver system. (a) Conventional receiver. (b) SAW-less receiver.

$$\text{Sensitivity}\,(\text{dBm}) =$$
$$10 \cdot \log_{10}\left[10^{\text{IM}_{2,\text{Tx}}/10} + K \cdot T \cdot B \cdot 10^{3} \cdot 10^{\text{NF}_{\text{ant}}/10}\right](\text{dBm}) + \text{CNR}\,(\text{dB}) \quad (1.15)$$

where $\text{IM}_{2,\text{Tx}}$ is the input referred IM_2 distortion power level in dBm. From (1.13)-(1.15), the required input referred IIP_2 can be calculated for a given sensitivity specification. The receiver sensitivity plot, with variation in IIP_2 performance at the Tx offset, is plotted in Fig. 1.13.

Single Tone Desense (STD)

When the Tx power leaks to the Rx port, and a jammer is present in the vicinity of the Rx band, the STD test becomes a key determiner of the receiver linearity and phase noise requirement. The conceptual explanation of the STD test in a conventional Zero-IF receiver is shown in Fig. 1.14(a). The leaked Tx signal, with an additional Rx-band jammer present, generates cross-modulation distortion (XMD) at the LNA output due to the nonlinearity of the LNA. This XMD creates additional noise in the Rx band and

Table 1.2: Test Parameters for CDMA Receiver STD [5]

Parameter	Units	Value
$\hat{\mathrm{I}}_{\mathrm{or}}$	dBm/1.23MHz	-101
$\frac{\text{Traffic } \mathrm{E_C}}{\mathrm{I_{or}}}$		$10^{-15.6/10}$
Data Rate (DR)	bps	9600
$\frac{\text{Traffic } \mathrm{E_b}}{\mathrm{N_t}}$		$10^{4.5/10}$
Spreading Rate (SR)	cps	1.2288×10^6
Frame Error Rate (FER)	%	1
Tone Offset from Carrier	kHz	$\pm$900
Tone Power	dBm	-30

degrades the signal-to-noise ratio (SNR). Since the jammer is in the Rx-band, the XMD depends on the LNA linearity, and the jammer adds additional noise in the Rx band due to reciprocal mixing [19, 20]. The required minimum performance for *STD* test is summarized in Table 1.2. As can be seen from Table 1.2, the differences compared to sensitivity are FER and $\hat{\mathrm{I}}_{\mathrm{or}}$. The $\hat{\mathrm{I}}_{\mathrm{or}}$ is increased by 3dB to accomodate additional noises from XMD and reciprocal mixing. Since the CNR is the same as before, the sensitivity, with a jammer present, can now be calculated as

$$\begin{aligned}&\text{Sensitivity}_{\mathrm{STD}}\,(\mathrm{dBm}) = \\ &10\cdot\log_{10}\Bigg[10^{\left(\mathrm{P_j}-\mathrm{TB}\right)\Big/10}+10^{\left(\mathrm{P_j}+\mathrm{P_{phase}}\right)\Big/10}+10^{\mathrm{IM_{2,Tx}}\Big/10}+ \\ &K\cdot T\cdot B\cdot 10^3\cdot 10^{\mathrm{NF_{ant}}\Big/10}\Bigg]\,(\mathrm{dBm})+\mathrm{CNR}\,(\mathrm{dB})\end{aligned} \tag{1.16}$$

where $\mathrm{P_j}$ is the Rx-band jammer power at the antenna (in dBm), and $\mathrm{P_{phase}}$ is the phase noise integrated over the signal bandwidth (1.25MHz) with the center frequency at the jammer frequency offset (in dBc). Assuming that synthesizer phase noise exhibits a

$1/f^2$ profile at the jammer frequency offset from the carrier frequency, $\mathrm{P_{phase}}$ can be calculated as

$$\mathrm{P_{phase}} = \mathrm{P_{spot}}\left(f_\mathrm{j}\right) \times \int_{f_\mathrm{j}-\frac{\mathrm{BW}}{2}}^{f_\mathrm{j}-\frac{\mathrm{BW}}{2}} \left(\frac{f_\mathrm{j}}{f}\right)^2 df = \mathrm{P_{spot}}\left(f_\mathrm{j}\right) \cdot f_\mathrm{j}^2 \frac{\mathrm{BW}}{f_\mathrm{j}^2 - \frac{\mathrm{BW}^2}{4}} \tag{1.17}$$

where f_j is a jammer frequency offset, which is specified by Table 1.2, and $\mathrm{P_{spot}}(f_\mathrm{j})$ is the spot phase noise at the jammer offset.

A test parameter, named the triple beat (TB), is introduced to emulate the XMD distortion. Simulation and measurement with a modulated signal (Tx) is extremely time consuming and tedious. The TB can be measured by applying three tones at the input: two tones in the Tx band and one jammer tone in the Rx band. Then, the resulting XMD tone will appear at the difference frequency of the two Tx tones from the Rx-band jammer offset. The TB specification is defined as the difference in power (in dB) between the jammer tone and the XMD tone, as shown in Fig. 1.15. As can be seen from (1.16), there is a trade-off between the TB and phase noise performance, since both add additional noise in the Rx band. The trade-off between TB and phase noise is plotted in Fig. 1.16. The sensitivity specification with a jammer present can never meet the -101dBm requirement if the TB is +68dB. But the phase noise can be relaxed to -75dBc with +72dB of TB. This TB level requires +8dBm of effective LNA $\mathrm{IIP_3}$ in a CDMA cellular system [9], assuming the LNA linearity dominates the TB performance. By inserting -75dBc integrated phase noise, the BW, and jammer offset frequency into (1.17), the spot phase noise requirement can be derived as -139dBc/Hz at 900kHz offset from the carrier frequency. In a SAW-less system, the TB requirement depends on the mixer and Trans-Impedance Amplifier (TIA) as well as the LNA, as shown in Fig. 1.14(b). The phase noise requirement at the jammer offset becomes extraordinarily difficult to meet if there is any additional TB contribution after the LNA, as can be seen from (1.16) and Fig. 1.16. Therefore, a highly linear receiver front-end from LNA to baseband (TIA) output is desirable and essential for a SAW-less receiver system.

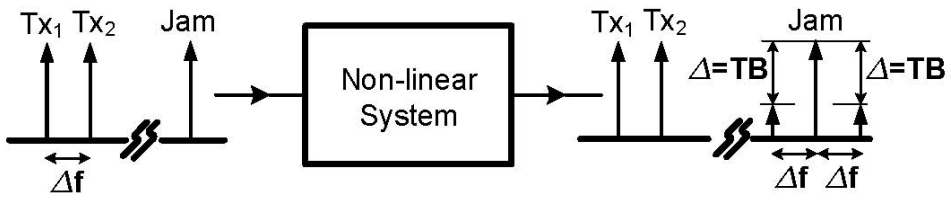

Figure 1.15: Triple-Beat definition.

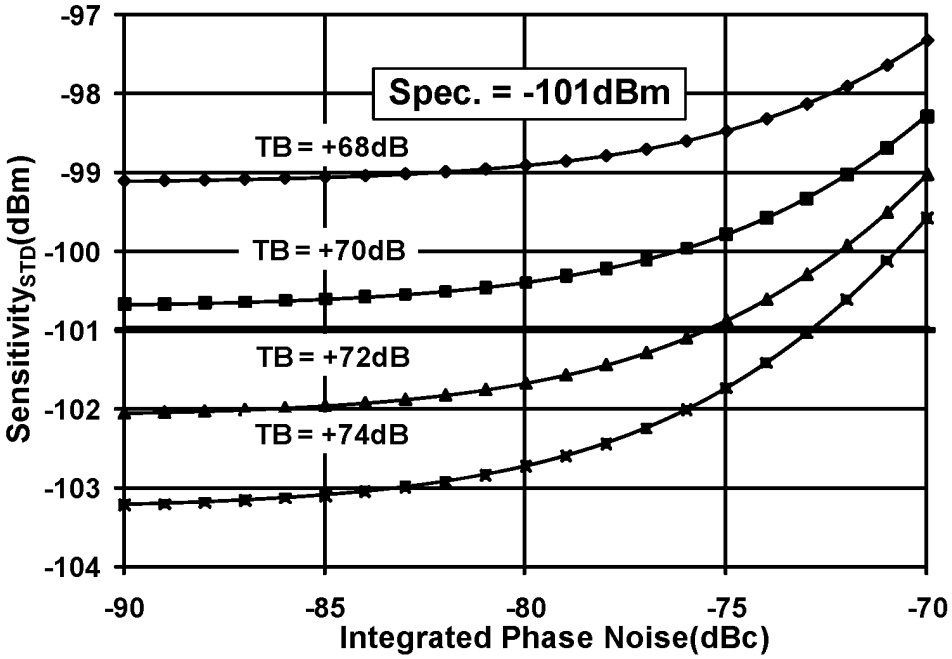

Figure 1.16: Trade-off between TB and phase noise.

Table 1.3: Target performance for SAW-less Receiver

Performance	Conventional Rx	SAW-less Rx	Units
Sensitivity	-109	-108.5	dBm
Triple Beat	72[a]	72[b]	dB
Integrated Phase noise	-75	-75	dBc
Spot Phase noise at $f_c \pm f_j$	-139	-139	dBc/Hz
Rx IIP_2	+35	+55	dBm

[a]LNA only
[b]LNA+mixer+TIA

Summary of SAW-less Receiver Performance

The summary of target performances for SAW-less receiver is shown in Table 1.3 with conventional receiver.

1.4 Dissertation Organization

The dissertation consists of five chapters.

Chapter I is an introduction to the wireless communication environment and SAW-less CDMA RF receiver specifications. The benefits of removing the inter-stage SAW filter between the LNA and mixer are introduced. A simple introduction of prior researches for SAW-less receiver is given. The effects of eliminating the SAW filter are introduced. The analysis of sensitivity and STD performances are given with/without the SAW filter.

Chapter II deals with linear LNA design issues. As specified in the standards, the linearity has to be met for both high-side and low-side jammer. Almost every linear LNA design assumes that the LNA will have symmetric performance, which is not generally the case. The widely used common-source and common-gate LNA topology linearities

are analyzed and the sources of asymmetry in the IM_3 performance are given. Methods for mitigating the asymmetry of the IM_3 issue are suggested. A highly linear differential APD LNA design is given as a part of a SAW-less receiver design.

Chapter III focuses on a highly linear low noise passive mixer by means of a resistive degeneration. A passive mixer has better linearity performance compared to an active mixer. But the passive mixer suffers from a well-known TIA noise amplification, which seriously degrades receiver NF in narrow-band applications, such as GSM and CDMA. A method of improving the TIA noise amplification due to the low mixer output impedance is proposed by resistively degenerating a conventional passive mixer. The effects of resistive degeneration are analyzed for gain, noise figure, and IIP_2 performances. The suggested passive mixer is manufactured and the performance improvement is verified through measurement.

Chapter IV introduces a new embedded filtering passive mixer (EFP mixer). Due to the high Tx power, the main contributor for corrupting the overall receiver linearity performance is the mixer and TIA. By introducing additional Tx filtering and isolating the non-ideal TIA effects, while the mixer is performing downconversion, the overall receiver linearity performances, IIP_2 and TB, are greatly improved. The new embedded filtering passive mixer is analized and the measured performances for a SAW-less receiver employing differential APD LNA and EFP mixer are given in this chapter.

Chapter V concludes this dissertation.

Chapter 2

Linear LNA Design

CMOS processes are increasingly popular for radio frequency(RF), due to the merits of low cost and easy integration with digital circuits. Most RF building blocks for receivers and transmitters now use CMOS processes [6, 21–24]. Due to this wide adoption, the design and analysis of CMOS integrated RF circuits has received considerable interest.

Among the various RF circuits, the LNA is one of the key components. The role of the LNA is to amplify the signal without adding excessive noise. Several studies optimizing the noise performance of LNAs have already been reported [25–27]. Another important parameter of the LNA is linearity in wireless communication systems, especially for frequency division duplex (FDD) systems [9,28], and the analysis of MOSFET amplifier linearity in the weakly non-linear region has been studied [29–32]. Special techniques for improving the linearity of MOSFET amplifiers have been researched as well [33–40].

In large-signal applications, such as power amplifiers, the asymmetry of the IM_3 is already identified and studied with compound semiconductor technologies [41–45]. But most of the studies are either highly dependent on measurement/simulation results [41–43] or describe incomplete expressions [44, 45].

This chapter addresses the IM_3 asymmetry issue for common-source(CS) and common-gate(CG) amplifier cases, which are the most common amplifiers in CMOS technology. Section 2.1 reviews the concept of IM_3 asymmetry in non-linear systems. Section 2.2 derives a complete Volterra series for a CS amplifier without ignoring the

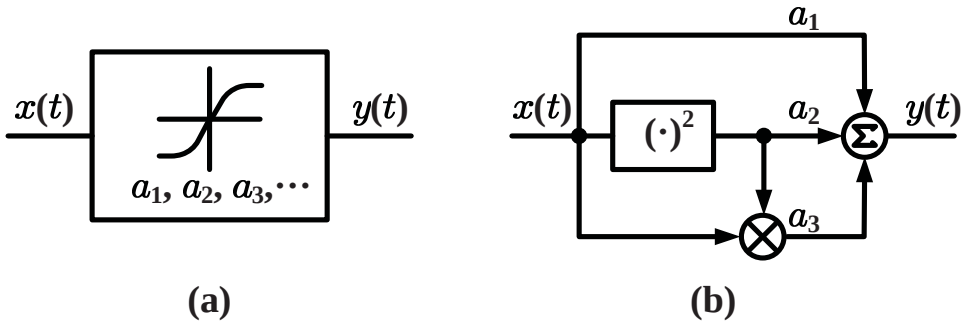

Figure 2.1: A memoryless, time-invariant non-linear system model (a) simple block diagram (b) equivalent representation for weakly non-linear system.

effect of $C_{\rm gd}$, and discusses the $\rm IM_3$ asymmetry issue and a method for alleviating the asymmetry. Section 2.3 derives the Volterra series for a CG amplifier, the $\rm IM_3$ asymmetry, and a method for mitigating the asymmetry. Section 2.4 shows a linear LNA design example and analyzes the effects of the linearization for input impedance, noise figure, transconductance, and linearity. Section 2.5 concludes and summarizes the results.

2.1 Review of $\rm IM_3$ Asymmetry Issue

A memoryless, time-invariant non-linear system can be modeled by [19]

$$y(t) = a_1 \cdot x(t) + a_2 \cdot x^2(t) + a_3 \cdot x^3(t) + \cdots \tag{2.1}$$

where, a_1 is the first-order coefficient, a_2 is the second-order coefficient, a_3 is the third-order coefficient. In a weakly non-linear system, the coefficients higher than third-order can be ignored [19]. A simple block diagram of such a system, and the equivalent representation for a weakly non-linear system, are shown in Fig. 2.1 [46]. Assume that this system has two input tones,

$$v_{\rm in}(t) = A_1 \cdot \cos(\omega_1 t) + A_2 \cdot \cos(\omega_2 t). \tag{2.2}$$

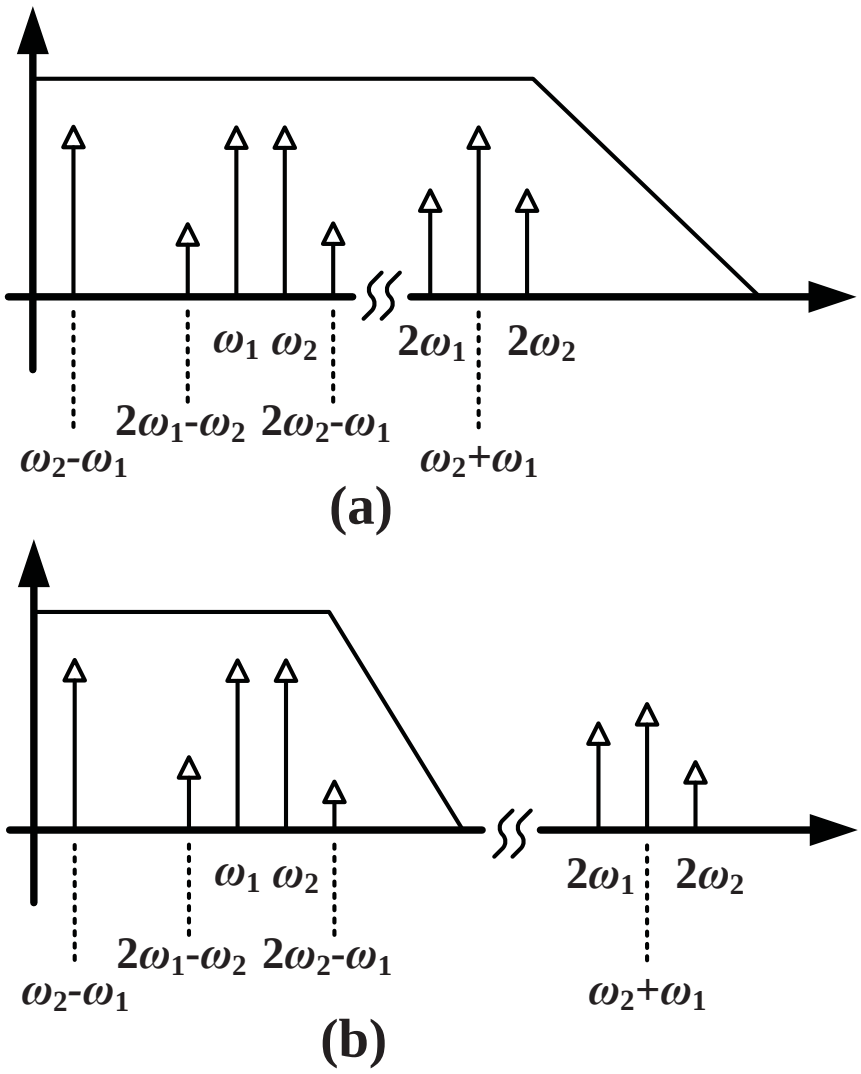

Figure 2.2: Effect of system bandwidth on IM_3 products (a) system bandwidth is larger than the second harmonic of the input tones. (b) system bandwidth is smaller than the second harmonic of the input tones.

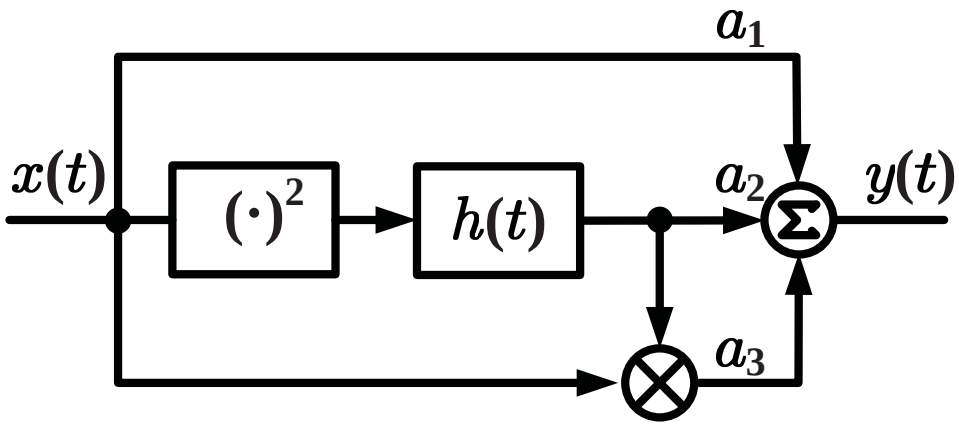

Figure 2.3: Modified equivalent representation of weakly non-linear system that includes memory effects.

Then, the resulting intermodulation terms caused by the third-order non-linearity are given by the well-known result.

$$\frac{3 \cdot a_3 \cdot A_1^2 \cdot A_2}{4} \cdot \cos(2\omega_1 \pm \omega_2)t \tag{2.3a}$$

$$\frac{3 \cdot a_3 \cdot A_2^2 \cdot A_1}{4} \cdot \cos(2\omega_2 \pm \omega_1)t \tag{2.3b}$$

As is clear from (2.3) and Fig. 2.1(b), the third-order intermodulation products are generated by squaring the input tones and multiplying that result with the input fundamental tones. It is important to understand that the square of the input is produced first to make the third-order intermodulation terms. And the resulting tones, such as $2\omega_2$, $2\omega_1$, $\omega_2 + \omega_1$, and $\omega_2 - \omega_1$, are multiplied by ω_1 and ω_2. In a memoryless non-linear system, the non-linear coefficients, the amplitudes, and the phases of each of the resulting tones from the squaring are assumed to be frequency independent. This assumption is true when the system bandwidth is much higher than the second harmonic frequency. This is illustrated in Fig. 2.2(a). For low-frequency applications, where the second harmonic of the input tone is much smaller than the system bandwidth, a memoryless non-linear system model is valid.

The model has to be modified in high-frequency applications, if the second harmonics of the input tones are at a higher frequency than the system bandwidth, as shown in Fig. 2.2(b). The two intermodulation products have different amplitudes due to the narrow bandwidth, and the difference will be larger with a larger frequency difference

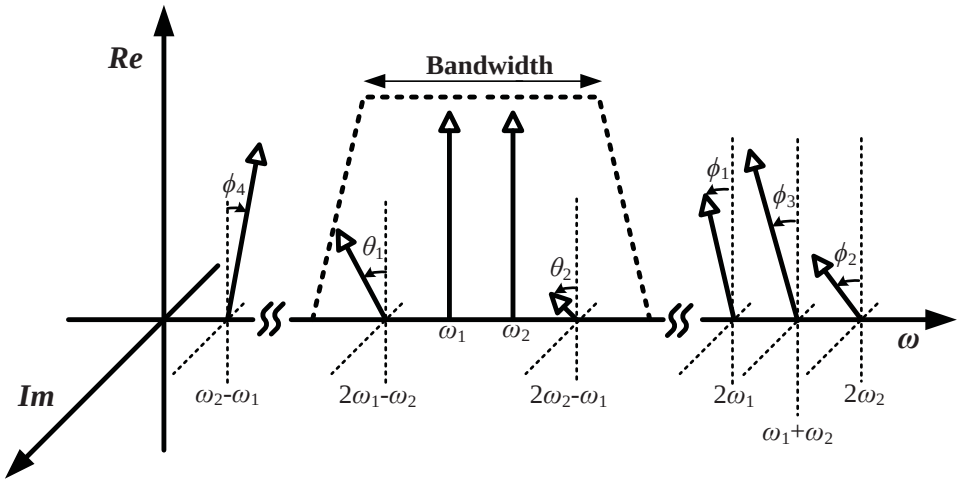

Figure 2.4: Demonstration of linear system response effect on IM_3 asymmetry.

between the two input tones. The equivalent representation of the memoryless system model needs to be modified to accomodate this effect.

The modified equivalent representation of the system is shown in Fig. 2.3. The $h(t)$ is the impulse response of a linear system. It can have a low-pass, band-pass, or high-pass response of any order, which is caused by the memory elements inside the system. The second harmonics, the sum, and the difference of the input tones have to experience this system response, resulting in different amplitudes and phases for each of the tones. Therefore, the IM_3 products will have different amplitudes and phases depending on the frequency offset of the two input tones, as can be seen from Fig. 2.4.

The system is assumed to have a band-pass response, since most RF blocks exhibit a band-pass response. Fig. 2.4 shows that the memory effect of the non-linear system cannot be predicted with a conventional power series expression, and so a Volterra series is used to calculate non-linear amplitude and phase effects simultaneously [47].

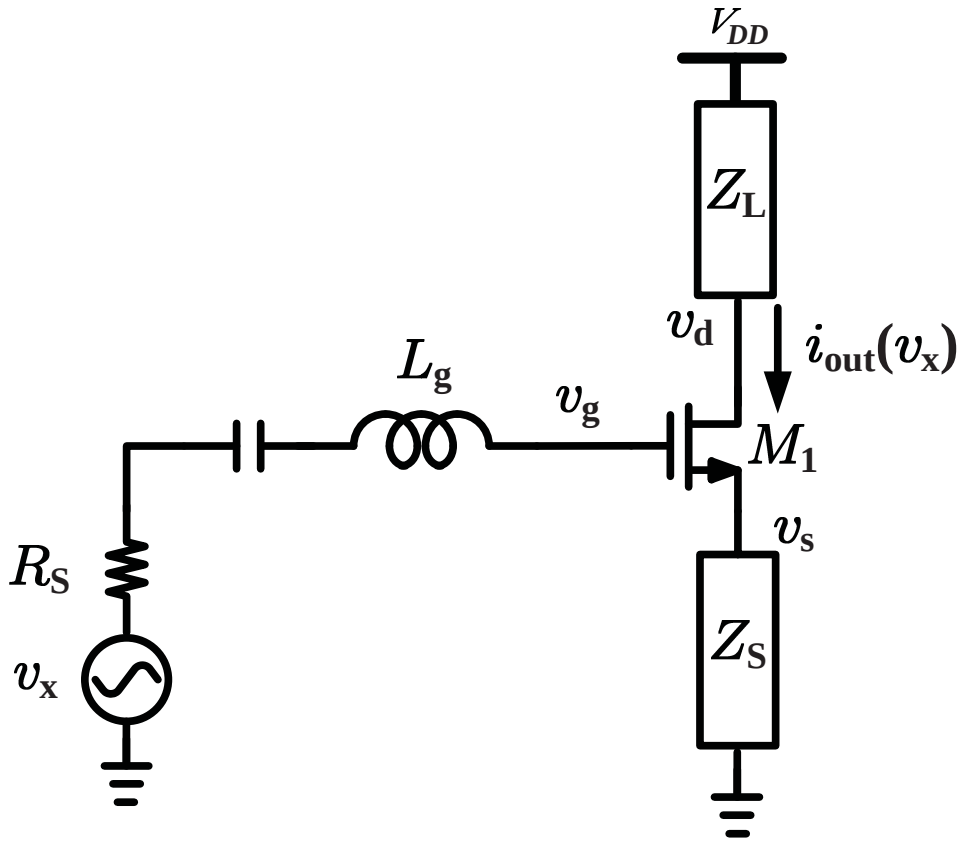

Figure 2.5: Simplified common-source amplifier.

2.2 Common Source Amplifier Volterra-Series Analysis and IM_3 Asymmetry

A commonly used CS amplifier, without the dc bias circuit, is shown in Fig. 2.5. To generalize the circuit for any conditions, the degeneration and load impedances are denoted by Z_S and Z_L, respectively. The Z_L can be either a cascode device or the load impedance, depending on the design. The complete small-signal equivalent circuit for the simplified CS amplifier with $C_{\rm gd}$ and $C_{\rm gs}$ is shown in Fig. 2.6. The external impedances, such as the source resistance and matching components, are combined as Z_1.

For the simplicity of the Volterra Series derivation, the following assumptions are made:

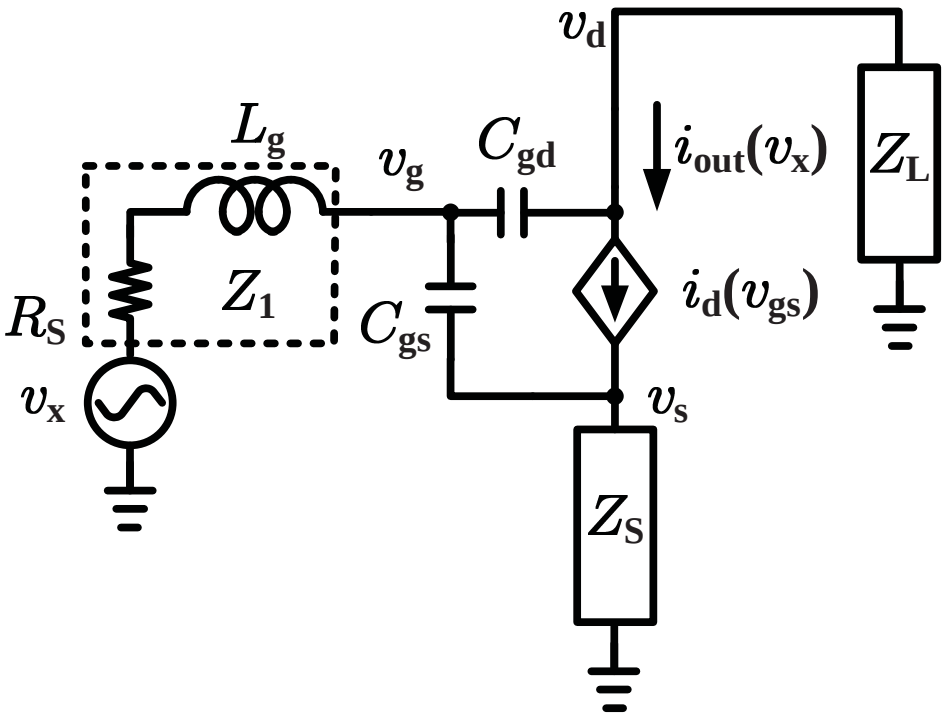

Figure 2.6: Equivalent circuit for CS amplifier including C_{gd} and C_{gs}.

- The resistance values for gate, source, and drain are insignificant. The gate resistance will be small in most LNA designs, since it has a direct effect on noise figure. The drain and source resistances will be kept small as well.
- The amplifier will be operating in the weakly non-linear region.
- The body effect will be negligible thanks to the use of triple-well process.
- The gate-source and gate-drain capacitances are constant at a fixed bias point.

From a time-invariant memoryless non-linear system model, the drain current of a MOSFET can be modeled by the power series representation

$$i_d(v_{gs}) = g_1 \cdot v_{gs} + g_2 \cdot v_{gs}^2 + g_3 \cdot v_{gs}^3 + \cdots \tag{2.4}$$

where, g_1 is the small-signal transconductance, g_2 is the first-order derivative of g_1, and g_3 is the second-order derivative of g_1. For a small-signal weakly non-linear system,

higher derivatives than second-order can be ignored, as explained in Section 2.1. The final goal is to derive the relationship between the input voltage and the output current so that the third-order non-linearity coefficient can be identified. In weakly non-linear operation, the output current can be represented by the following truncated Volterra series

$$i_{\mathrm{out}}(v_{\mathrm{x}}) = C_1(s) \circ v_{\mathrm{x}} + C_2(s_1, s_2) \circ v_{\mathrm{x}}^2 + C_3(s_1, s_2, s_3) \circ v_{\mathrm{x}}^3 \tag{2.5}$$

where, $C_{\mathrm{n}}(s_1, s_2, \cdots, s_{\mathrm{n}})$ is the Laplace transform of the *n*th-order Volterra kernel and the operator " $\circ$ " means that each spectral component of $v_{\mathrm{x}}^{\mathrm{n}}$ is multiplied by the magnitude of $C_{\mathrm{n}}(s_1, s_2, \cdots, s_{\mathrm{n}})$ and shifted by the phase of $C_{\mathrm{n}}(s_1, s_2, \cdots, s_{\mathrm{n}})$. The gate-source voltage and gate-drain voltage can be expressed by a truncated Volterra series, as a function of input voltage, as well.

$$v_{\mathrm{gs}}(v_{\mathrm{x}}) = A_1(s) \circ v_{\mathrm{x}} + A_2(s_1, s_2) \circ v_{\mathrm{x}}^2 + A_3(s_1, s_2, s_3) \circ v_{\mathrm{x}}^3 \tag{2.6a}$$

$$v_{\mathrm{gd}}(v_{\mathrm{x}}) = B_1(s) \circ v_{\mathrm{x}} + B_2(s_1, s_2) \circ v_{\mathrm{x}}^2 + B_3(s_1, s_2, s_3) \circ v_{\mathrm{x}}^3 \tag{2.6b}$$

where, $A_{\mathrm{n}}(s_1, s_2, \cdots, s_{\mathrm{n}})$ and $B_{\mathrm{n}}(s_1, s_2, \cdots, s_{\mathrm{n}})$ are the Laplace transforms of the nth-order Volterra kernels. From Fig. 2.6, a nodal equation at the drain node can be derived as

$$i_{\mathrm{out}} = i_{\mathrm{d}} - sC_{\mathrm{gd}} \cdot v_{\mathrm{gd}} \tag{2.7}$$

where, s can be s_1, $s_1 + s_2$, or $s_1 + s_2 + s_3$ depending on the non-linearity order. By inserting (2.4), (2.5), (2.6a), and (2.6b) into (2.7), the Volterra kernels of $i_{\mathrm{out}}(v_{\mathrm{x}})$ can be expressed in the manner of $A_{\mathrm{n}}(s_1, s_2, \cdots, s_{\mathrm{n}})$ and $B_{\mathrm{n}}(s_1, s_2, \cdots, s_{\mathrm{n}})$. Therefore, the first step is to determine $A_{\mathrm{n}}(s_1, s_2, \cdots, s_{\mathrm{n}})$ and $B_{\mathrm{n}}(s_1, s_2, \cdots, s_{\mathrm{n}})$. The *harmonic input* method will be used to calculate each Voterra kernel in (2.5) and (2.6) [48]. This method is based on multitone excitation and solving the nodal equations in the frequency domain at the sum of all input frequencies. The detailed procedure of deriving the Volterra kernels is presented in Appendix A.

From (A.16), the high-side($2\omega_2 - \omega_1$) and low-side($2\omega_1 - \omega_2$) IM_3 products can

be derived.

$$C_3(-j\omega_1, j\omega_2, j\omega_2) = A_1^2(j\omega_2) \cdot A_1(-j\omega_1) \times \left[\frac{1}{g_1 + g(j2\omega_2 - j\omega_1)} \cdot \frac{\alpha(j2\omega_2 - j\omega_1)}{Z_{\rm x}(j2\omega_2 - j\omega_1)}\right] \cdot \epsilon(j\Delta\omega, j2\omega_2) \tag{2.8a}$$

$$C_3(-j\omega_2, j\omega_1, j\omega_1) = A_1^2(j\omega_1) \cdot A_1(-j\omega_2) \times \left[\frac{1}{g_1 + g(j2\omega_1 - j\omega_2)} \cdot \frac{\alpha(j2\omega_1 - j\omega_2)}{Z_{\rm x}(j2\omega_1 - j\omega_2)}\right] \cdot \epsilon(-j\Delta\omega, j2\omega_1) \tag{2.8b}$$

where $A_1(s)$ is the linear transfer function from $v_{\rm x}$ to $v_{\rm gs}$ and is the major factor defining the IM$_3$ amplitude level. Therefore, the effects of $C_{\rm gd}$ must be included in the calculation, since $C_{\rm gd}$ affects the linear transfer function directly. The resulting plots of (2.8) along with the simulated results are shown in Fig. 2.7 for high-side IM$_3$ and Fig. 2.8 for low-side IM$_3$, respectively. The test input tones with -30dBm power are at 1GHz(f_1) and 1GHz+Δf(f_2), where Δf is 1MHz and 50MHz. The CS amplifier considered in the simulation and calculation has a cascode device, so that the loading impedance is low. The plots show the IM$_3$ products along with gate-source bias voltage from 0V to 0.9V. The important bias voltage range is between 0.45V to 0.55V, since the current consumption in this range is 5-15mA and the $|S_{11}|$ is less than -10dB in that region.

As can be seen from Figs. 2.7 and 2.8, the high-side IM$_3$ products exhibit higher IM$_3$ amplitude with larger Δf, while the low-side IM$_3$ shows lower IM$_3$ amplitude with larger Δf. The maximum amplitude differences between high-side and low-side IM$_3$ products with various Δf's in the bias range of 0.45-0.55V are shown in Fig. 2.9. The amplitude difference is determined by $\epsilon(\Delta j\omega, j2\omega)$, since this is the only term that can set the overall IM$_3$ to be zero. By assuming $\Delta\omega C_{\rm gd} \approx \Delta\omega C_{\rm gs} \approx 0$ and $Z_{\rm S}(j\omega)$=$j\omega L_{\rm S}$ for the normal inductively degenerated CS amplifier case, $\epsilon(\Delta j\omega, j2\omega)$ given in (A.15) can be approximated by

$$\epsilon(j\Delta\omega, j2\omega) \approx g_3 - \frac{2}{3} \cdot g_2^2 \cdot \left[\frac{2 \cdot j\Delta\omega L_{\rm S}}{g_1 \cdot j\Delta\omega L_{\rm S} + 1} + \frac{1}{g_1 + g(j2\omega)}\right] \tag{2.9}$$

where, $g(j\omega)$ is given by (A.6a). To understand the root cause of the asymmetry, the second term in the bracket of (2.9) has to be simplified. Assuming an inductively degenerated CS amplifier, which has a cascode device and so the effects of $Z_{\rm L}(j\omega)$ can be

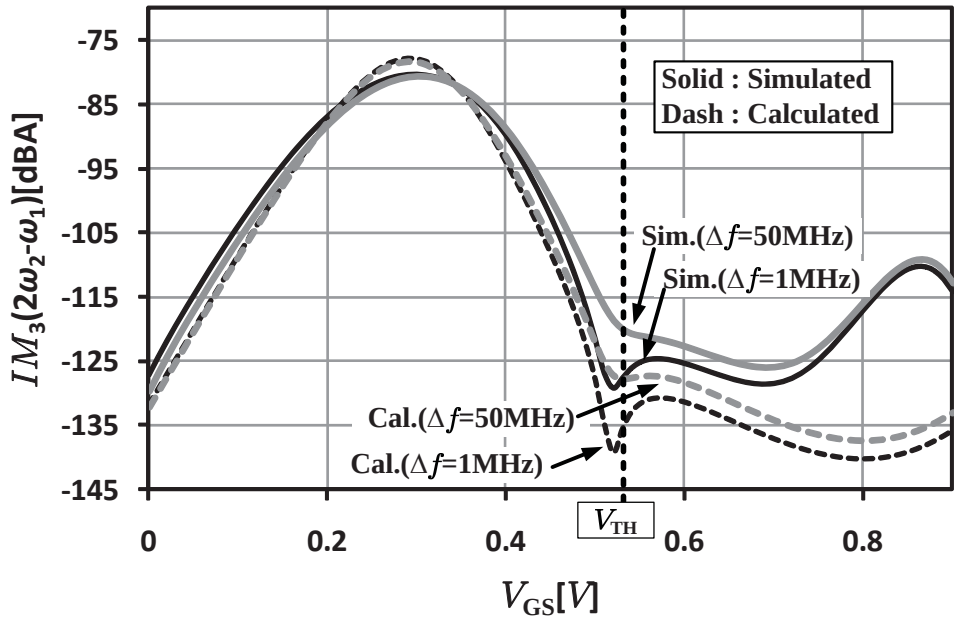

Figure 2.7: Calculated and simulated high-side($2\omega_2 - \omega_1$) IM$_3$ of CS amplifier. $P_{\mathrm{IN}} = -30$dBm, $f = 1$GHz, Wg=500μm, Lg=60nm.

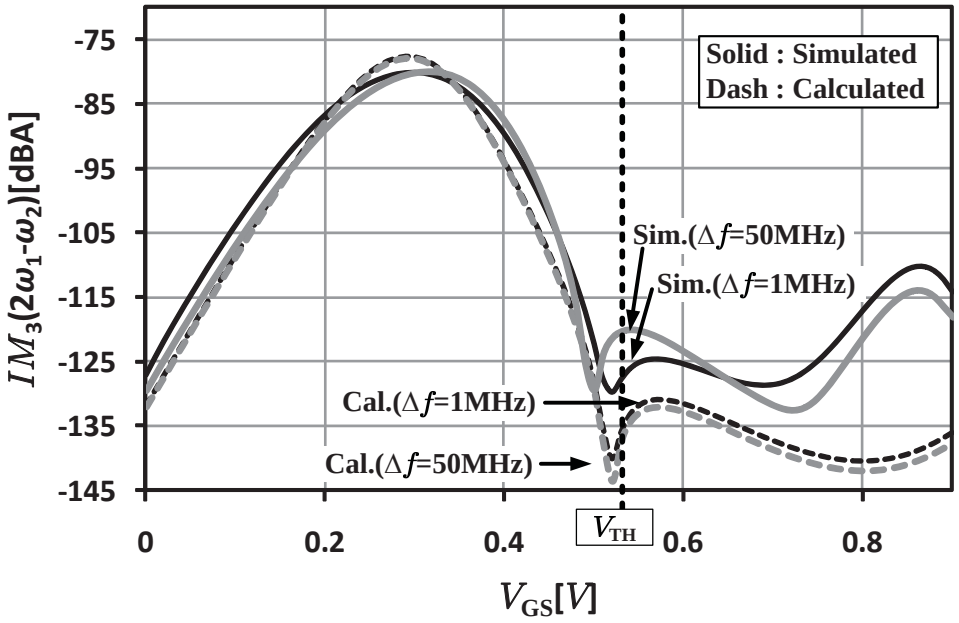

Figure 2.8: Calculated and simulated low-side($2\omega_1 - \omega_2$) IM$_3$ of CS amplifier. $P_{\mathrm{IN}} = -30$dBm, $f = 1$GHz, Wg=500μm, Lg=60nm.

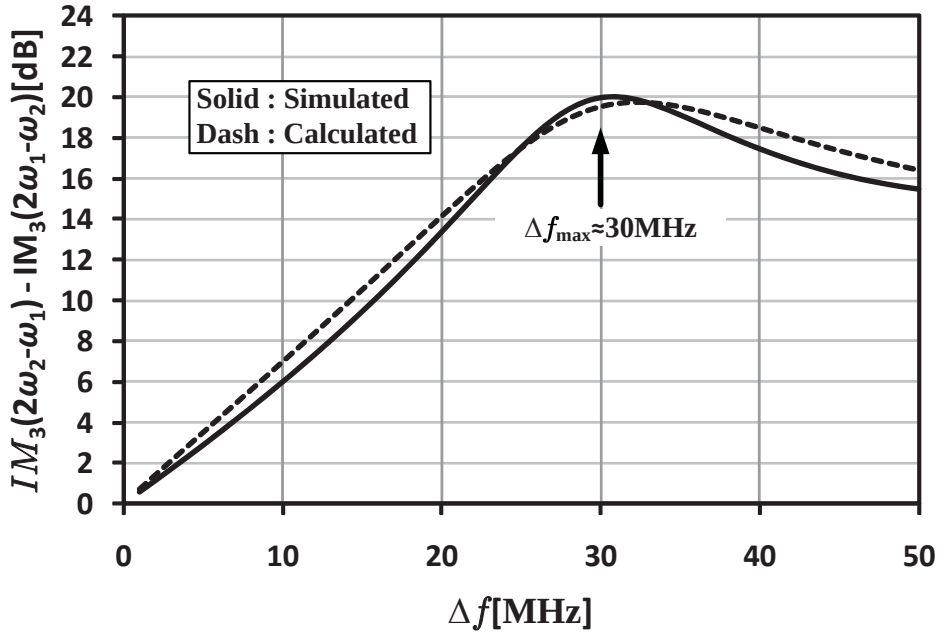

Figure 2.9: Calculated and simulated IM_3 asymmetry of CS amplifier. $P_{\mathrm{IN}} = -30$dBm, $f = 1$GHz, Wg=500μm, Lg=60nm.

ignored, the second term in the bracket of (2.9) can be approximated by (2.10).

$$\frac{1}{g_1 + g(j\omega)} \approx \frac{j\omega L_{\mathrm{S}} \cdot (1 + Z_1(j\omega) \cdot j\omega C_{\mathrm{gd}})}{[g_1 \cdot j\omega L_{\mathrm{S}} + j\omega L_{\mathrm{S}} \cdot j\omega C_{\mathrm{gs}} + 1] \cdot [1 + Z_1(j\omega) \cdot j\omega C_{\mathrm{gd}}] + Z_1(j\omega) \cdot j\omega C_{\mathrm{gs}}} \tag{2.10}$$

Inserting (2.10) into (2.9), the simplifed ϵ for high-side($2\omega_2 - \omega_1$) and low-side($2\omega_1 - \omega_2$) IM_3 can be expressed. The resulting plot is shown in Fig. 2.10, with the result from (2.8). As can be seen, the simplified equation can be used to roughly predict the frequency offset, where the maximum amplitude difference between high-side and low-side IM_3 occurs, and the resulting amplitude difference.

By assuming $2\omega_2 \approx 2\omega_1$ for the case of $\Delta\omega \leq 50$MHz, (2.10) can be the same for both high-side and low-side. Therefore, the root cause of the asymmetry comes from the amplitude difference of the imaginary portions of (2.9). The imaginary portions of (2.9)

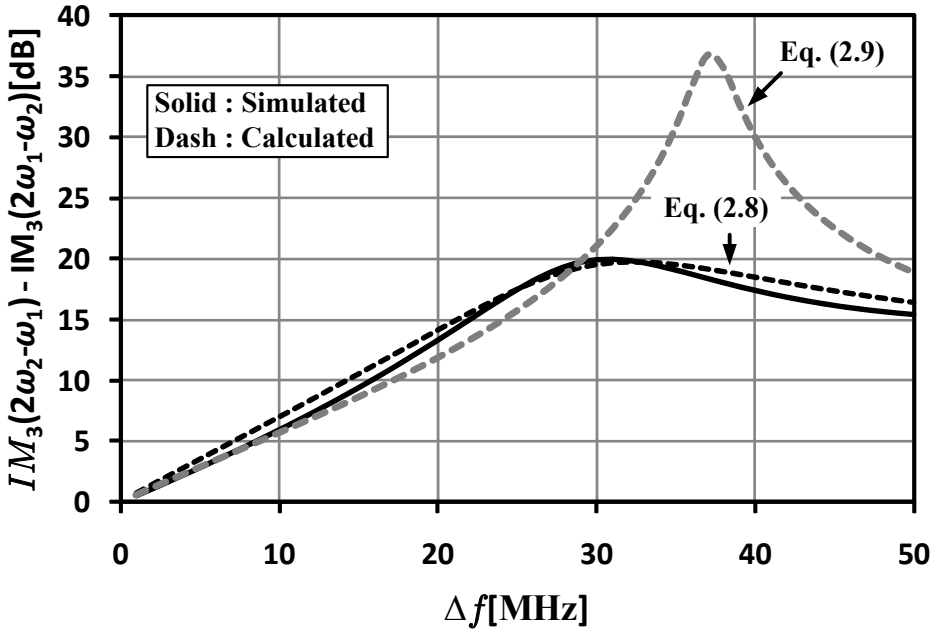

Figure 2.10: Comparison of CS amplifier aysmmetry; full calculation vs simplified calculation vs simulation. $P_{\mathrm{IN}} = -30$dBm, $f = 1$GHz, Wg=500μm, Lg=60nm.

for the high-side and low-side can be expressed as

$$\mathrm{Im}(\epsilon(j\Delta\omega, j2\omega_2)) = -\frac{2}{3}\cdot g_2^2\cdot\left[\frac{2\cdot\Delta\omega L_{\mathrm{S}}}{1+(g_1\cdot\Delta\omega L_{\mathrm{S}})^2}+\mathrm{Im}\left(\frac{1}{g_1+g(j2\omega)}\right)\right] \tag{2.11a}$$

$$\mathrm{Im}(\epsilon(-j\Delta\omega, j2\omega_1)) = -\frac{2}{3}\cdot g_2^2\cdot\left[\frac{-2\cdot\Delta\omega L_{\mathrm{S}}}{1+(g_1\cdot\Delta\omega L_{\mathrm{S}})^2}+\mathrm{Im}\left(\frac{1}{g_1+g(j2\omega)}\right)\right] \tag{2.11b}$$

As can be seen from (2.11), the Im(ϵ) of (2.11a) exhibits a continuous amplitude increase with larger frequency offset, while the Im(ϵ) of (2.11b) shows the characteristic of $|ax-b|$, depending on the design parameters. It is clear that there would not be any asymmetry if there was no contribution from the second-harmonic and the difference frequency, as explained in Section 2.1. The maximum asymmetry frequency offset($\Delta\omega_{\max}$) can be predicted by setting Im(ϵ) of (2.11b) to zero.

The asymmetry in the CS amplifier is caused by L_{S}. The first terms of (2.11) show the L_{S} contribution. As is clear from (2.10), the second terms in the brackets of (2.11) will be zero, if $L_{\mathrm{S}} = 0$.

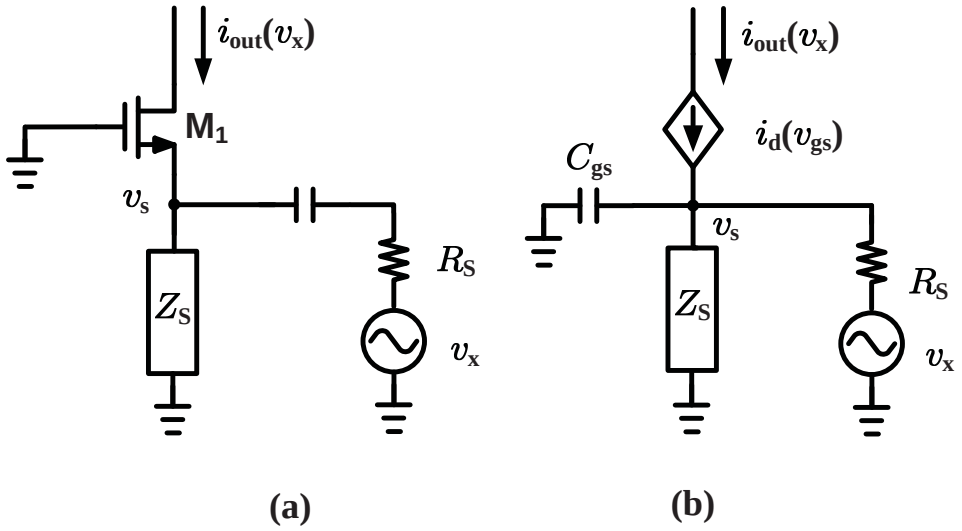

Figure 2.11: Common-Gate amplifier (a)simplified schematic (b)small-signal equivalent circuit.

2.3 Common Gate (CG) Amplifier Volterra-Series Analysis and IM_3 Asymmetry

A simplified CG amplifier schematic with its small-signal equivalent circuit is shown in Fig. 2.11, where Z_S can be the bias circuit or a choke. A complete set of Volterra kernels for the CG amplifier has already been derived in [49]. But the method used in [49] is based on a current approach with feedback theory. To be consistent with the CS case, the complete derivation of the CG amplifier with the direct voltage method is shown in Appendix B. As in the CS case in Section 2.2, the same assumptions are applied to the CG case as well.

From (B.7), the high-side($2\omega_2-\omega_1$) and low-side($2\omega_1-\omega_2$) IM_3 products of CG amplifer can be shown to be

$$C_3(-j\omega_1, j\omega_2, j\omega_2) = A_1^2(j\omega_2)\cdot A_1(-j\omega_1)$$
$$\times\,[1+g_1\cdot R_S\cdot A_1(j2\omega_2-j\omega_1)]\cdot\epsilon(j\Delta\omega, j2\omega_2) \tag{2.12a}$$
$$C_3(-j\omega_2, j\omega_1, j\omega_1) = A_1^2(j\omega_1)\cdot A_1(-j\omega_2)$$
$$\times\,[1+g_1\cdot R_S\cdot A_1(j2\omega_1-j\omega_2)]\cdot\epsilon(-j\Delta\omega, j2\omega_1) \tag{2.12b}$$

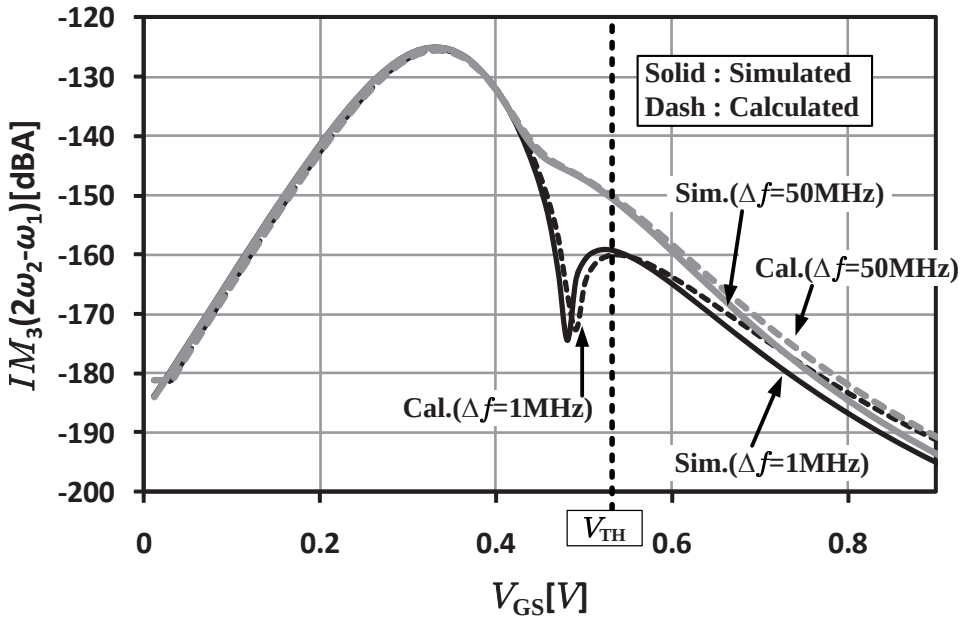

Figure 2.12: Calculated and simulated high-side($2\omega_2 - \omega_1$) IM_3 of CG amplifer. $P_{\mathrm{IN}} = -30$dBm, $f = 1$GHz, Wg=160μm, Lg=60nm.

As in the CS amplifier case, $A_1(s)$ is the linear transfer function from v_{x} to v_{gs}=$-v_{\mathrm{s}}$ and is the major factor of defining the IM_3 amplitude level. With the same test condition as in the CS amplifier case, the resulting plots of (2.12) along with simulated results are shown in Fig. 2.12 and Fig. 2.13.

As in the CS amplifier case, the asymmetry of the CG amplifier comes from $\epsilon(\Delta j\omega, j2\omega)$. With the assumptions of $\Delta\omega C_{\mathrm{gs}} \approx 0$, $R_{\mathrm{S}} \approx g_1^{-1}$, and $Z_{\mathrm{S}}(j\omega) = j\omega L_{\mathrm{S}}$, (B.6) can be approximated for high-side($2\omega_2 - \omega_1$) and low-side($2\omega_1 - \omega_2$).

$$\epsilon(j\Delta\omega, j2\omega_2) \approx g_3 - \frac{2}{3}\cdot g_2^2 \cdot \times \left(\frac{2\cdot j\Delta\omega L_{\mathrm{S}}}{2g_1\cdot j\Delta\omega L_{\mathrm{S}}+1} + \frac{j2\omega_2 L_{\mathrm{S}}}{1-(2\omega_2)^2 C_{\mathrm{gs}}L_{\mathrm{S}} + 2g_1\cdot j2\omega_2 L_{\mathrm{S}}}\right) \tag{2.13a}$$

$$\epsilon(-j\Delta\omega, j2\omega_1) \approx g_3 - \frac{2}{3}\cdot g_2^2 \cdot \times \left(\frac{-2\cdot j\Delta\omega L_{\mathrm{S}}}{2g_1\cdot j\Delta\omega L_{\mathrm{S}}+1} + \frac{j2\omega_1 L_{\mathrm{S}}}{1-(2\omega_1)^2 C_{\mathrm{gs}}L_{\mathrm{S}} + 2g_1\cdot j2\omega_1 L_{\mathrm{S}}}\right) \tag{2.13b}$$

The plots of the amplitude difference between high-side and low-side IM_3, along with

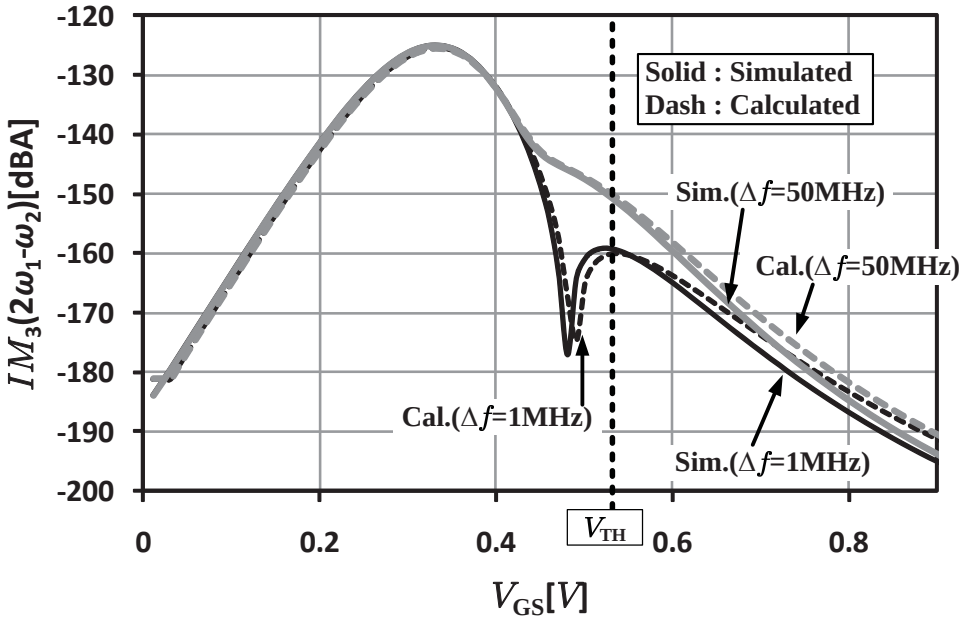

Figure 2.13: Calculated and simulated high-side($2\omega_1 - \omega_2$) IM_3 of CG amplifer. $P_{\mathrm{IN}} = -30$dBm, $f = 1$GHz, Wg=160μm, Lg=60nm.

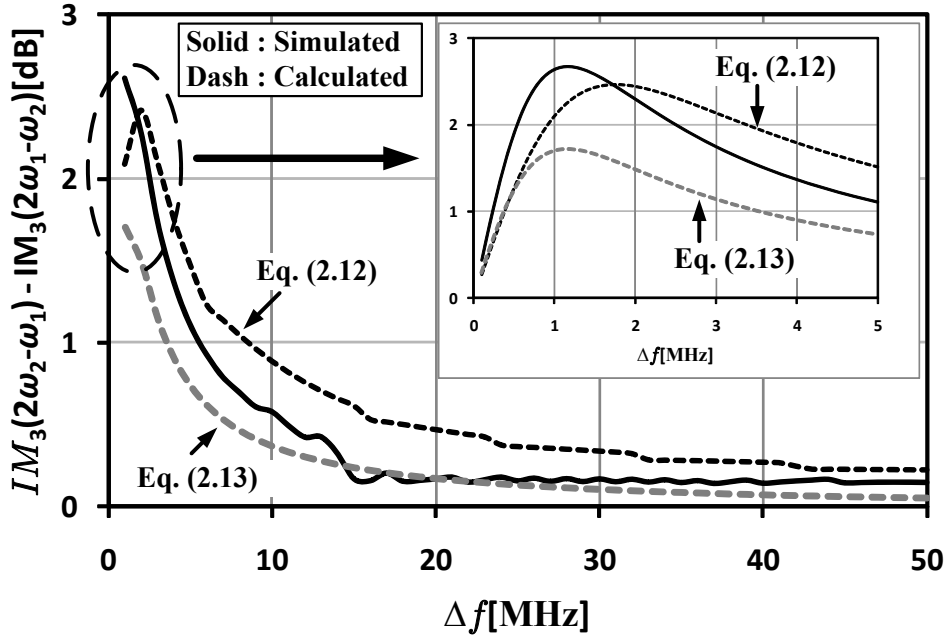

Figure 2.14: Comparison of CG amplifier aysmmetry; full calculation vs simplified calculation vs simulation.

simulated results, are shown in Fig. 2.14. The result predicted by the simplified model is very accurate. Equation (2.13) suggests that the asymmetry in the CG amplifier can be mitigated, if the bias choke inductor(L_{S}) resonates with C_{gs} at the second harmonic frequency of the input. Therefore, the optimum L_{S} value in the CG case can be given by

$$L_{\mathrm{S,opt}} \approx \frac{1}{(2\omega_1)^2 \cdot C_{\mathrm{gs}}} \tag{2.14}$$

2.4 Linear LNA Design Example

Due to the high IIP_3 requirement of the LNA, the conventional source degenerated CS LNA is not suitable. There are various ways of designing a highly linear CS LNA, such as the modified derivative superposition method (MDS) [34] and the active post-distortion method (APD) [33]. In this design, the APD method is chosen. With this method, the complexity of the bias circuitry and the related input parasitic capacitance can be reduced.

2.4.1 Input Impedance

The LNA has a low-linearity and a high-linearity mode of operation. The APD method is used in the high-linearity mode to overcome the linearity issue in the STD test case, but it is not used in the low-linearity case, because it slightly degrades the LNA noise figure and effective transconductance.

The simplified schematic of the LNA is shown in Fig. 2.15. The inductor L_{S} is a source degeneration inductance and L_l is a load inductance. Transistors M_1, M_2, M_5, and M_6 form the main signal path, while M_3 and M_4 act as IM_3 cancellers. The APD method is combined with source cross coupling to further improve the linearity and IM_3 asymmetry by increasing degeneration. The mode control between two states is acheived by turning ON/OFF M_3 and M_4. The simplified half-equivalent circuit of the LNA in the high-linearity mode is shown in Fig. 2.16. The input impedance in the high-linearity mode is

$$Z_{\mathrm{in}}(j\omega) = \frac{1}{j\omega \cdot C_{\mathrm{gs},1} \cdot [1 - \alpha(j\omega)] + j\omega \cdot C_{\mathrm{gd},1} \cdot [1 - \beta(j\omega)]} \tag{2.15}$$

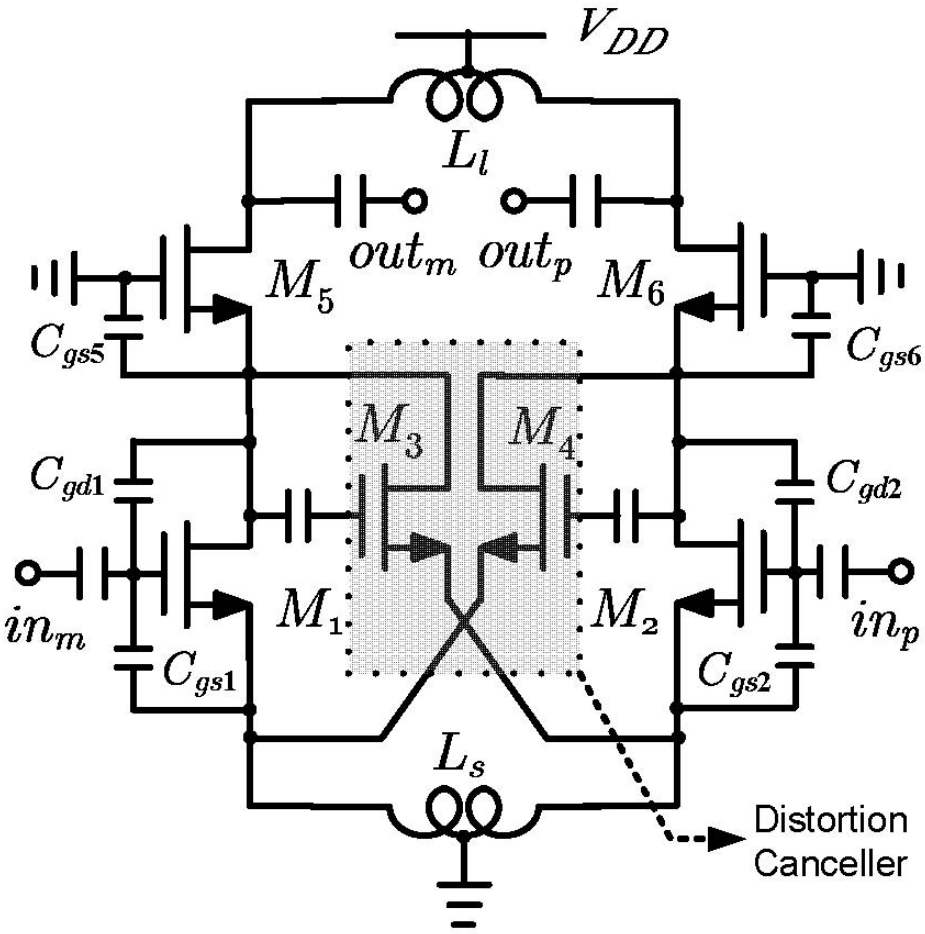

Figure 2.15: Simplified schematic of the differential APD LNA.

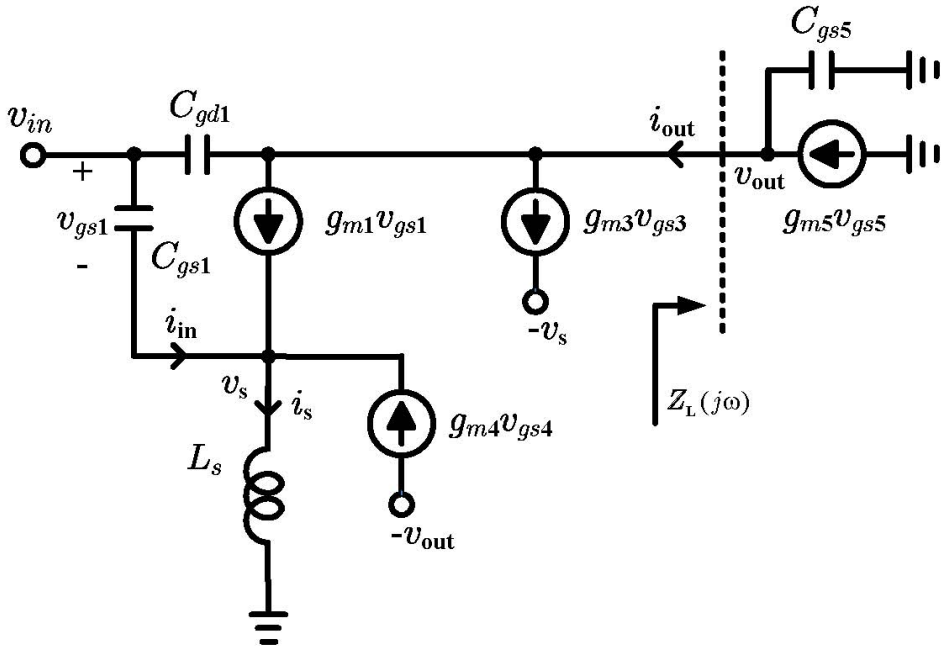

Figure 2.16: Simplified schematic of the differential APD LNA.

where

$$\alpha(j\omega) \approx \frac{j\omega \cdot L_{\mathrm{S}} \cdot [j\omega \cdot C_{\mathrm{gs},1} + g_{\mathrm{m},1}]}{1 + j\omega \cdot L_{\mathrm{S}} \cdot [j\omega \cdot C_{\mathrm{gs},1} + g_{\mathrm{m},1} + g_{\mathrm{m},3}]} \tag{2.16a}$$

$$\beta(j\omega) = \frac{Z_{\mathrm{L}}(j\omega) \cdot [j\omega \cdot C_{\mathrm{gd},1} - g_{\mathrm{m},1} \cdot (1 - \alpha(j\omega)) - g_{\mathrm{m},3} \cdot \alpha(j\omega)]}{1 + Z_{\mathrm{L}}(j\omega) \cdot [j\omega \cdot C_{\mathrm{gd},1} + g_{\mathrm{m},3}]} \tag{2.16b}$$

$$Z_{\mathrm{L}}(j\omega) = \frac{1}{j\omega \cdot C_{\mathrm{gs},5} + g_{\mathrm{m},5}} \tag{2.16c}$$

where $g_{\mathrm{m},1}$ is the transconductance of the input FET, $g_{\mathrm{m},3}$ is the transconductance of the canceller FETs, $g_{\mathrm{m},5}$ is the transconductance of the cascode FET, $C_{\mathrm{gs},1}$ is the gate-to-source capacitance of the input FET, $C_{\mathrm{gd},1}$ is the gate-to-drain capacitance of the input FET, and $C_{\mathrm{gs},5}$ is the gate-to-source capacitance of the cascode FET. Note that the input impedance in the high-linearity mode is same as the low-linearity mode if $g_{\mathrm{m},3}$ is set to 0. The simulated and calculated input impedances of the LNA in both modes are shown in Fig. 2.17, and the agreement is excellent. The impedance in the high-linearity mode is higher than the low-linearity mode up to 1.5GHz. There are slight differences between simulated and calculated values due to the additional parasitics related to the nonlinearity canceller FETs.

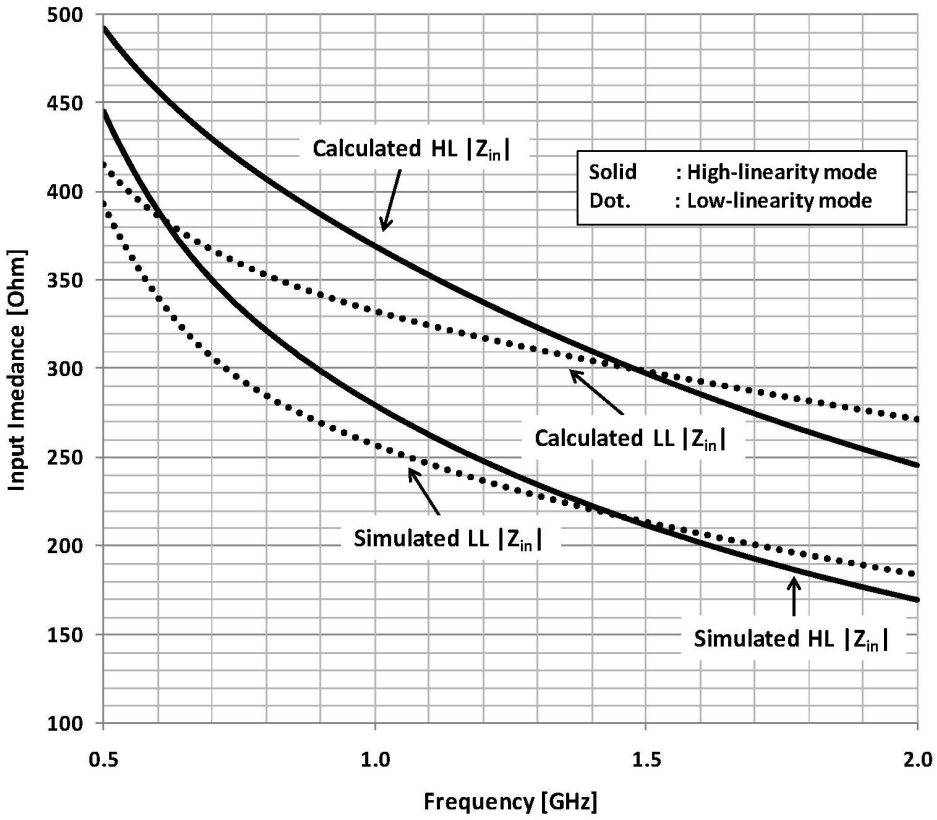

Figure 2.17: Calculated and simulated input impedance of the APD LNA in high/low-linearity modes.

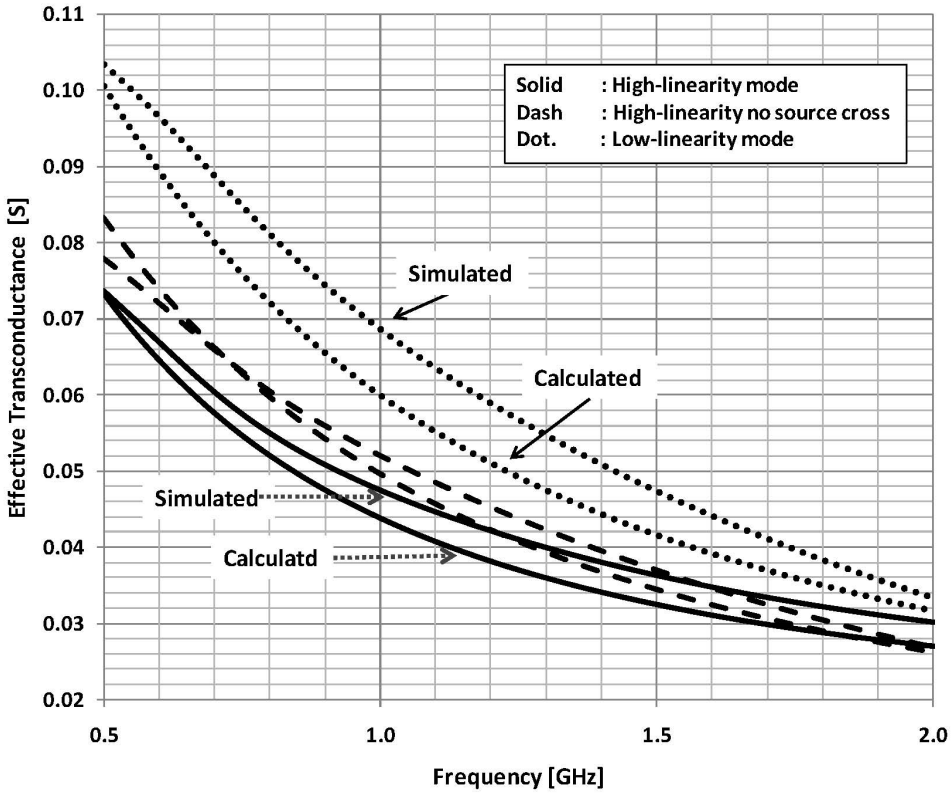

Figure 2.18: Calculated and simulated effective transconductance of the APD LNA in high/low-linearity modes.

2.4.2 Effective Transconductance

The effective transconductance of the LNA will differ in the low-linearity and high-linearity modes. The effective transconductance in the two modes can be derived from Fig. 2.16.

$$G_{\mathrm{m}}(j\omega) \approx \frac{g_{\mathrm{m},1}}{1 + g_{\mathrm{m},3} \cdot Z_{\mathrm{L}}(j\omega)} \cdot \frac{1 + j\omega \cdot L_{\mathrm{S}} \cdot g_{\mathrm{m},3}}{1 - \omega^2 \cdot C_{\mathrm{gs1}} \cdot L_{\mathrm{S}} + j\omega \cdot L_{\mathrm{S}} \cdot (g_{\mathrm{m},1} + g_{\mathrm{m},3})} \qquad (2.17)$$

In the derivation of (2.17), the effect of C_{gd} is ignored. The effective transconductance expression (2.17) can be used for the low-linearity mode assuming $g_{\mathrm{m},3}$ = 0. The first term of the right-hand side in (2.17) represents the gain loss using the APD method. The second term represents the effect of the cross-coupled devices. It further reduces, by means of the effective source degeneration boost, the overall transconductance. The simulated and calculated effective transconductance in both modes are shown in Fig. 2.18,

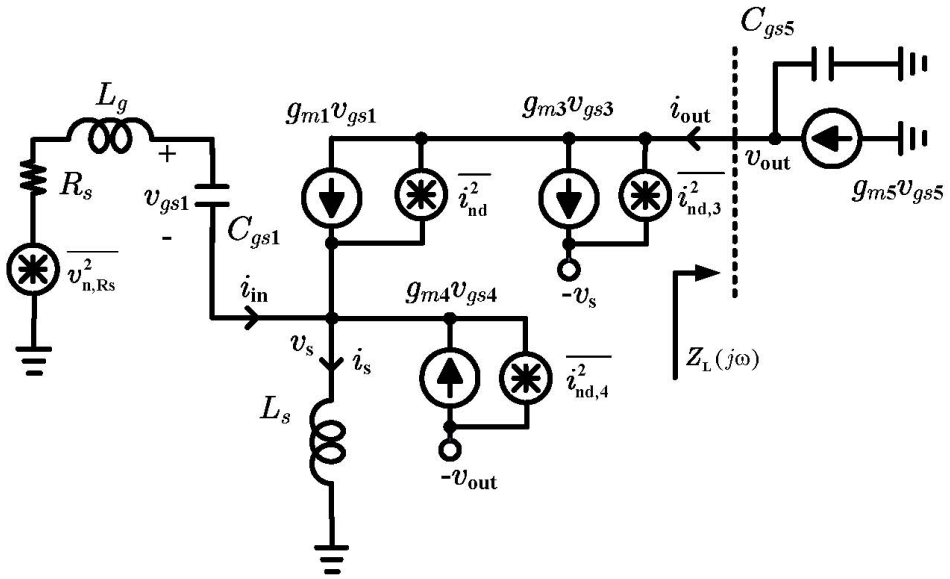

Figure 2.19: Noise equivalent half-circuit of the differential APD LNA.

and the agreement is excellent. To show the effect of the cross-coupled devices, the calculated effective transconductance of the case in [33], where there is no source cross-couple, is plotted in same Figure. As expected, the effective transconductance is smaller in the high-linearity mode and the cross-coupling boosts the source degeneration. As described in [33], there is an optimum value of $g_{\mathrm{m},3}$ to maximize IM_3 cancellation. The value of $g_{\mathrm{m},3}$, therefore, needs to be chosen to optimize the gain and linearity trade-off.

2.4.3 Noise Analysis

The high-linearity mode has a lower gain than the low-linearity mode, which degrades the overall system noise figure. To calculate the amplifier noise figure, the channel noise of the input FET will be considered to be the only noise source in the LNA. The source noise transfer function can be derived, since the input impedance and the effective transconductance are known from (2.15)- (2.17). With the assumption of a single matching component(L_{g}), as shown in Fig. 2.19, the output noise, due to the source is

$$\overline{i^2_{\mathrm{ns,o}}} = \left| \frac{Z_{\mathrm{in}}(j\omega)}{R_{\mathrm{S}} + j\omega \cdot L_{\mathrm{g}} + Z_{\mathrm{in}}(j\omega)} \right|^2 \cdot G^2_{\mathrm{m}}(j\omega) \cdot 4 \cdot \kappa \cdot T \cdot R_{\mathrm{s}} \cdot B \tag{2.18}$$

where $i_{\mathrm{ns,o}}$ is the output noise due to the source in either mode. Equation (2.18) applies for both high-linearity and low-linearity modes with appropriate input impedance and effective transconductance. The output noise due to the input FET channel noise is given in (2.19).

$$\overline{i^2_{\mathrm{nd,o}}} = \left| \frac{1 - \omega^2 C_{\mathrm{gs,1}} (L_{\mathrm{S}} + L_{\mathrm{g}}) + j\omega C_{\mathrm{gs,1}} R_{\mathrm{S}} + 2j\omega L_{\mathrm{S}} g_{\mathrm{m,3}} \left[1 - \omega^2 C_{\mathrm{gs,1}} L_{\mathrm{g}} + j\omega C_{\mathrm{gs,1}} R_{\mathrm{S}}\right]}{\Delta(j\omega) \left(1 + g_{\mathrm{m,3}} Z_{\mathrm{L}}(j\omega)\right) + j\omega L_{\mathrm{S}} g_{\mathrm{m,3}} \left[1 - \omega^2 C_{\mathrm{gs,1}} L_{\mathrm{g}} + g_{\mathrm{m,1}} Z_{\mathrm{L}}(j\omega) + j\omega C_{\mathrm{gs,1}} R_{\mathrm{S}}\right]} \right|^2 \times \overline{i^2_{\mathrm{nd}}} \tag{2.19}$$

where, i_{nd} is the channel noise. The derivation of (2.19) is shown in Appendix C. The output noise due to the channel noise in the high-linearity mode is the same as in the low-linearity mode once $g_{\mathrm{m,3}}$ is set to zero. From (2.15)- (2.19), the ratio of the noise factors in the high-linearity and low-linearity mode for a fixed L_{s} and L_{g} is

$$\frac{F_{\mathrm{HL}}}{F_{\mathrm{LL}}} = \frac{1 + \overline{i^2_{\mathrm{ndHL,o}}} / \overline{i^2_{\mathrm{nsHL,o}}}}{1 + \overline{i^2_{\mathrm{ndLL,o}}} / \overline{i^2_{\mathrm{nsLL,o}}}} \tag{2.20}$$

The resulting plot of the noise figure ratio is shown in Fig. 2.20 with the solid line. The difference between high linearity and low linearity is negligible in the US Cellular band (869 894MHz), where the S_{11} is better than 10dB. The most important difference between the two modes is the distortion canceller noise, which will directly add to the noise factor. The amount of the added noise due to distortion canceller noise is approximately equal to the transconductance ratio between main path and auxiliary path [33], and the noise transfer function of the nonlinearity canceller FETs is described in Appendix C. The effect of the added canceller noise is plotted in Fig. 2.20 with the dotted line. The canceller increases the noise figure by almost 0.1dB, which agrees with the results in [33]. The NF difference becomes noticeable above 1GHz. From 1GHz to 1.7GHz, the high-linearity mode noise is lowest, because the channel noise transfer function is smaller than the low-linearity mode. Above 1.7GHz, the channel noise transfer function in the high-linearity mode is higher than in the low-linearity mode, which makes the noise performance worse.

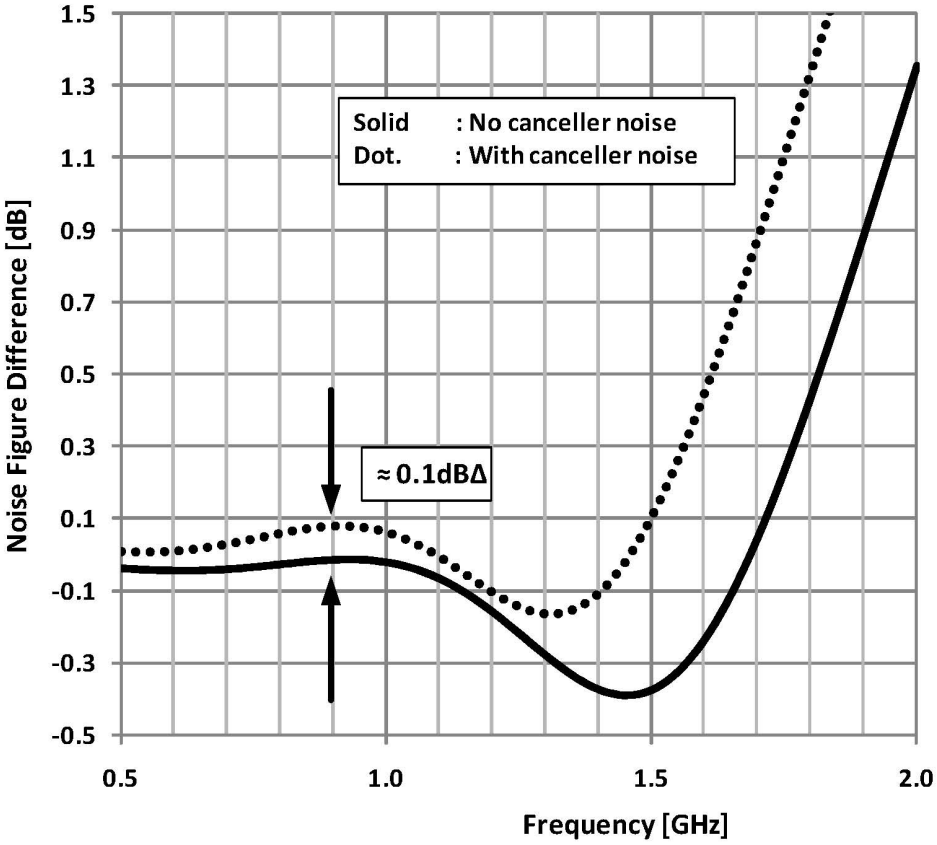

Figure 2.20: Calculated NF difference between HL and LL with/without canceller noise.

2.4.4 Linearity Analysis

As explained in section 2.4.1, the input impedance will be different for the schematic shown in Fig 2.15 compared to normal CS amplifier. The different input impedance leads into different transfer function from source voltage ($v_{\rm x}$) to $v_{\rm gs}$, meaning that A_1, A_2, and A_3 will be changed. To simplify the analysis, the $C_{\rm gd}$ is assumed to be ignorable. By following same procedure as in Appendix A with the equivalent schematic shown in Fig. 2.19, the A_1 of the cross-coupled APD LNA can be found.

$$A_{1,APD}(s) = \frac{1}{g_{m1} + g_{\rm APD}(s)} \cdot \frac{1 + sL_{\rm s} \cdot g_{\rm m4}}{sL_{\rm s} \cdot [1 + (1/\beta) \cdot (sC_{\rm gs1}Z_1(s) + \alpha + 1)]} \tag{2.21}$$

where

$$g_{\rm APD}(s) = \frac{1 + sC_{\rm gs1} \cdot (Z_1(s) + sL_{\rm s})}{sL_{\rm s} \cdot [1 + (1/\beta) \cdot (sC_{\rm gs1}Z_1(s) + \alpha + 1)]}, \tag{2.22}$$

$Z_1(s) = sL_{\rm g}(s) + R_{\rm S}$, $\alpha = g_{\rm m1}/g_{\rm m5}$, and $\beta = g_{\rm m1}/g_{\rm m4}$. By assuming $\Delta\omega C_{\rm gs1} \approx 0$, the expression as in (2.11) can be derived for the cross-coupled APD LNA.

$$\begin{aligned}&{\rm Im}(\epsilon(j\Delta\omega, j2\omega_2)) \approx \\ &-\frac{2}{3} \cdot g_{12}^2 \cdot \left[\frac{2 \cdot \Delta\omega L_{\rm S} \cdot \left[1 + \frac{\alpha+1}{\beta}\right]}{1 + \left(g_{m1} \cdot \Delta\omega L_{\rm S} \cdot \left[1 + \frac{\alpha+1}{\beta}\right]\right)^2} + {\rm Im}\left(\frac{1}{g_{m1} + g_{\rm APD}(j2\omega)}\right) \right]\end{aligned} \tag{2.23a}$$

$$\begin{aligned}&{\rm Im}(\epsilon(-j\Delta\omega, j2\omega_1)) \approx \\ &-\frac{2}{3} \cdot g_{12}^2 \cdot \left[\frac{-2 \cdot \Delta\omega L_{\rm S} \cdot \left[1 + \frac{\alpha+1}{\beta}\right]}{1 + \left(g_{m1} \cdot \Delta\omega L_{\rm S} \cdot \left[1 + \frac{\alpha+1}{\beta}\right]\right)^2} + {\rm Im}\left(\frac{1}{g_{m1} + g_{\rm APD}(j2\omega)}\right) \right]\end{aligned} \tag{2.23b}$$

where g_{12} is the coefficient of the second order distortion of the M_1 device. With the values for the $\alpha = 1.77$ and $\beta = 8$ as in [33], it is clear that the effective $L_{\rm s}$ value is increased. A larger $L_{\rm s}$ value means that the asymmetry peak point will move to smaller Δf, like in CG amplifier case, so that the asymmetry at the Tx frequency offset can be improved. A comparsion of asymmetry IM_3 performance between normal CS LNA and APD LNA is shown in Fig. 2.21.

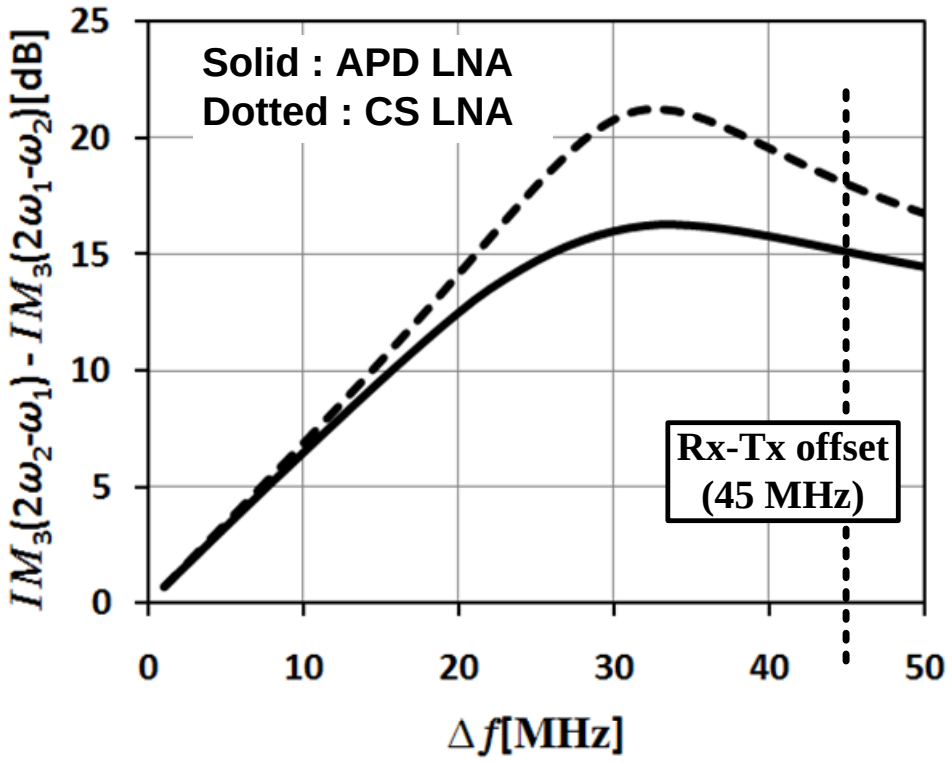

Figure 2.21: Asymmetry IM_3 performance comparsion between CS and APD LNA.

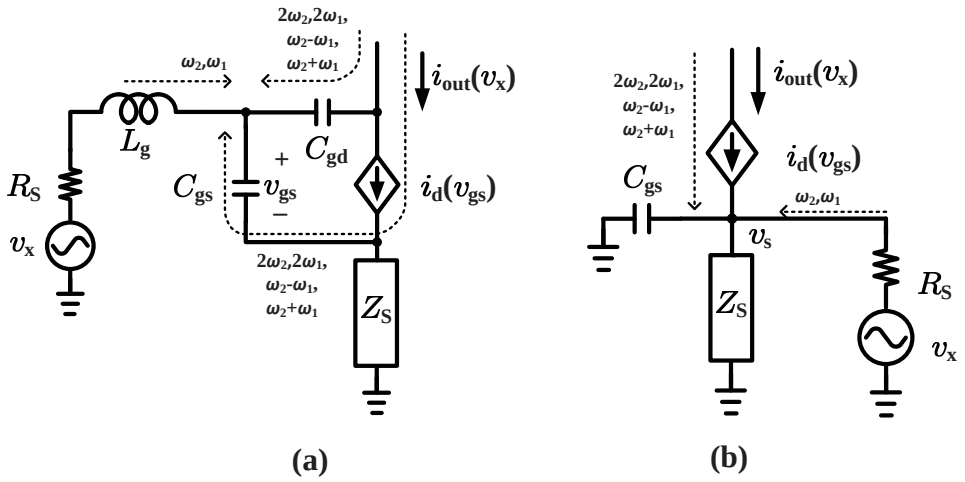

Figure 2.22: Graphical illustration of the second harmonic and difference frequency feedback effect (a) CS amplifier (b) CG amplifier.

2.5 Conclusion and Discussion

In this chapter, the intermodulation asymmetry for the CS and CG MOSFET amplifiers, operating in the weakly non-linear region, is analyzed. The root cause of the asymmetry is identified as the second-harmonic and difference frequency effect, caused by the band-pass response. The second harmonics and difference frequency of the input tones, experiencing different amplitude and phase responses, are fedback to the input and mixed with the fundamental tones via the device non-linearity, resulting in asymmetry between high-side($2\omega_2 - \omega_1$) and low-side($2\omega_1 - \omega_2$) IM_3. Graphical explanations of the feedback paths for the CS and CG amplifiers are shown in Fig. 2.22.

For the CG amplifier case, the asymmetry can be reduced by resonating the input capacitances with an inductor at the second harmonic frequency. In the CS amplifier, the feedback through the source degeneration(L_S), C_gd, and C_gd have to be minimized to reduce the asymmetry.

In the narrowband case, the CS nonlinearity (2.9) and CG nonlinearity (2.13) show the same general behavior. The main difference between the two is the much larger L_S value in the CG case. The IM_3 asymmetry ratio of the CS and CG amplifiers can both be expressed as a function of $\Delta\omega$, as can be seen from both (2.9) and (2.13),

i.e.

$$\left|\frac{\text{IM}_3(\Delta\omega)}{\text{IM}_3(-\Delta\omega)}\right| = \frac{\left|\text{Re} + j\left(c + \frac{a\cdot\Delta\omega}{1+(b\cdot\Delta\omega)^2}\right)\right|}{\left|\text{Re} + j\left(c - \frac{a\cdot\Delta\omega}{1+(b\cdot\Delta\omega)^2}\right)\right|} \tag{2.24}$$

where, $a = 2L_{\text{S}}$, $b = g_1 L_{\text{S}}$ for the CS and $b = 2g_1 L_{\text{S}}$ for the CG, c is mainly determined by 2ω and L_{S}, and Re is the real value of (2.9) and (2.13). Therefore, the asymmetry ratio (2.24) increases as a function of $\Delta\omega$ until the imaginary value of its denominator reaches zero, and the ratio then decreases at higher values of $\Delta\omega$. The maximum asymmetry ratio (2.24) can be expressed by

$$\left|\frac{\text{IM}_3(\Delta\omega)}{\text{IM}_3(-\Delta\omega)}\right| = \frac{|\text{Re} + j\,(2\cdot c)|}{|\text{Re}|} \tag{2.25}$$

In the CG amplifier, the peak asymmetry ratio (2.24) happens at a lower $\Delta\omega$ than the CS amplifer, since the CG L_{S} value is usually much larger than the CS L_{S} value. This is confirmed by comparing Fig. 2.9 and Fig. 2.14.

An example of highly linear LNA design is presented in this chapter. The effects of using cross-coupled APD method are explained for input impedance, noise figure, and linearity. The cross-coupled APD method increased the input impedance by effectively increasing the degneration inductance value, so that the linearity is improved in high linearity mode and the asymmetry IM_3 at Tx frequency offset as well. This chapter has been submitted for review for the following publication:

1. N. Kim, V. Aparin, and L. E. Larson, "Analysis of IM_3 asymmetry in MOSFET small-signal amplifiers," submitted to *IEEE Trans. Circuits Syst. I, Reg. Papers*

Chapter 3

Highly Linear Resistively Degenerated Passive Mixer

CMOS processes have been scaled to shorter gate lengths to improve overall area and power consumption, while achieving higher unity gain frequency (f_t). Even though a shorter gate length is helpful for better radio frequency (RF) performance, it introduces more flicker noise (*1/f* noise) [7,19,20,50]. Especially for narrowband wireless systems, such as cellular systems, the *1/f* noise seriously degrades NF performance.

There have been some efforts to improve *1/f* noise performance of active mixers [51–53]. A PMOS switching pair, rather than an NMOS switching pair, is reported in [51]. A method of flicker noise cancellation is introduced in [52]. Another way to mitigate *1/f* noise is by adopting longer channel length devices, since *1/f* noise is inversely proportional to the channel length [54]. But using non-minimum channel length FETs will introduce other problems. The parasitic capacitance associated with the gate will be increased, degrading RF gain and noise performance [55].

The best way to alleviate the *1/f* noise contribution is to have zero DC current flowing in the switching core [56]. This leads to a passive mixer application. There are several drawbacks to the use of a passive mixer. The well-known characteristic of poor thermal noise performance is the main concern [57].

This chapter describes wideband operation of a passive mixer with low NF and highly linear performance, while consuming 10mW from a 2V supply. Section 3.1 reviews the conventional passive CMOS mixer architecture and related issues. Section 3.2

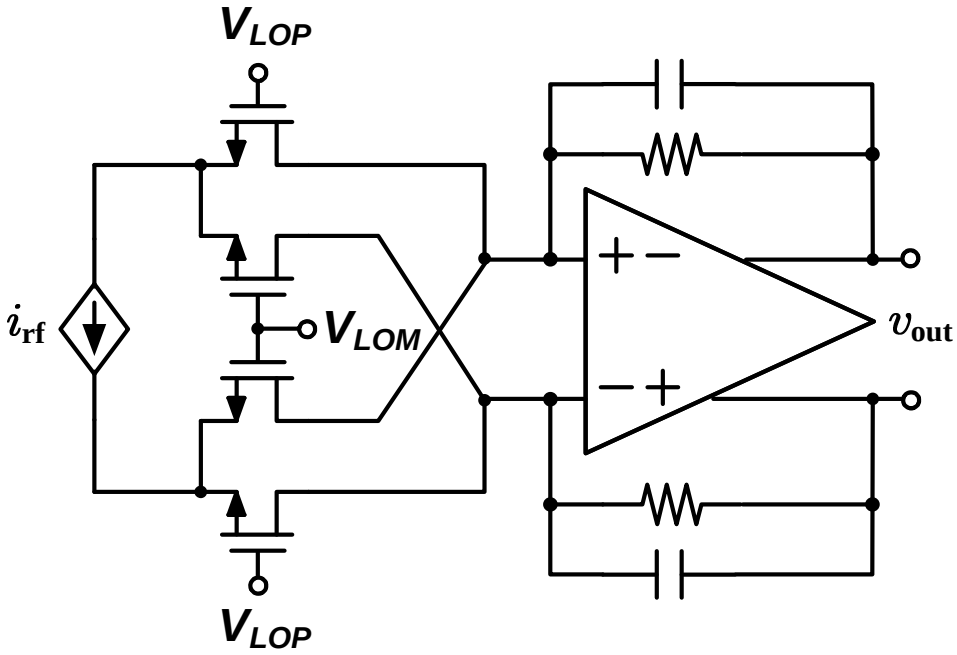

Figure 3.1: Conventional passive mixer.

introduces and analyzes an improved resistively degenerated passive mixer topology. Section 3.3 describes individual block design. Section 3.4 presents measured results. Section 3.5 concludes this chapter.

3.1 Conventional CMOS Passive Mixer Design

There have been many publications using a passive mixer architecture to avoid *1/f* noise issues [58–65]. The most common CMOS passive mixer architecture employs a *"current input and current output"* approach, with a TIA output stage to provide a low impedance at the mixer output, as shown in Fig. 3.1 [62]. This approach will exhibit a high NF due to conversion loss and well-known TIA noise amplification [58], i.e.

$$\overline{v_{\mathrm{no,TIA}}^2} = \left(1 + \frac{2 \cdot R_{\mathrm{TIA}}}{R_{\mathrm{Mix}}}\right)^2 \cdot \overline{v_{\mathrm{ni,TIA}}^2} \tag{3.1}$$

where, $v_{\mathrm{no,TIA}}$ is the TIA output noise voltage due to the noise generated by the TIA, $v_{\mathrm{ni,TIA}}$ is the input referred TIA noise voltage, R_{TIA} is the feedback resistance of the

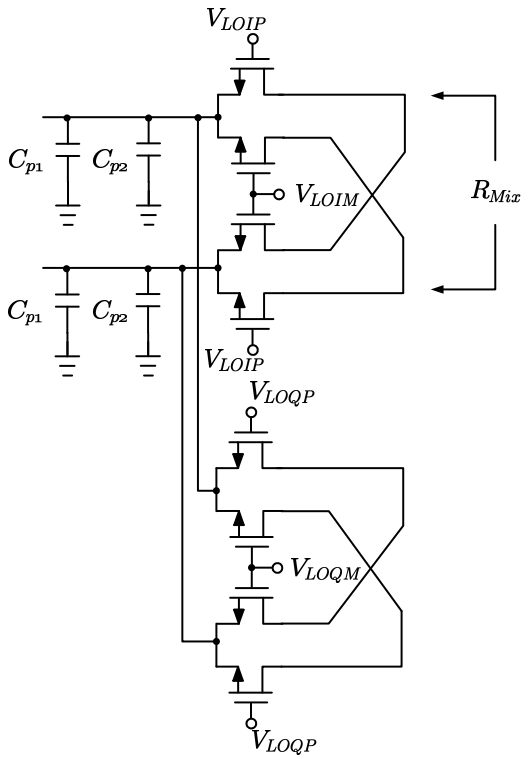

Figure 3.2: Equivalent circuit for R_{Mix} calculation for dual channel mixer.

TIA stage and R_{Mix} is the equivalent mixer output resistance.

As can be seen from (3.1), R_{Mix} needs to be as high as possible to reduce noise amplification of the TIA input referred noise.

The mixer equivalent circuit, used to calculate R_{Mix}, which is a function of the switched-parasitic capacitance and mixer turn-on resistance, is shown in Fig. 3.2. When the mixer switch is operating, the time domain response of an input voltage step on the parasitic capacitances would be,

$$V_{\mathrm{C}}(t) \cong V_{\mathrm{step}} \cdot \left(1 - e^{\frac{-t}{\alpha \cdot \left(C_{\mathrm{p1}}+C_{\mathrm{p2}}\right) \cdot \beta \cdot R_{\mathrm{on}}}}\right) \tag{3.2}$$

and the charge stored on the parasitic capacitances will be

$$Q_{\mathrm{C}}(T_{\mathrm{LO}}) = \alpha \cdot (C_{\mathrm{p1}} + C_{\mathrm{p2}}) \cdot V_{\mathrm{step}} \cdot \left(1 - e^{\frac{-T_{\mathrm{LO}}}{\alpha \cdot \left(C_{\mathrm{p1}}+C_{\mathrm{p2}}\right) \cdot \beta \cdot R_{\mathrm{on}}}}\right) \tag{3.3}$$

where, C_{p1} is the parasitic capacitance from the output stage of the preceding G_{m} stage, C_{p2} is the parasitic capacitance from the mixer cores, R_{on} is the turn-on resistance of each mixer FET, α is the capacitance multiplication factor, which is two for a single-channel and four for a dual-channel (I/Q) in a doubly-balanced mixer, and β is a resistance multiplication factor (two), which is coming from two series switches in the switched-capacitor. The capacitance multiplication factor (α) arises from the parallel connection of the FETs in the doubly-balanced mixer. For an I/Q mixer, there are four parallel connections. From (3.3), the equivalent mixer output resistance, which can be expressed as a switched-capacitor resistance [66], is

$$R_{\mathrm{Mix}} = \left[f_{\mathrm{LO}} \cdot \alpha \cdot (C_{\mathrm{p1}} + C_{\mathrm{p2}}) \cdot \left(1 - e^{\frac{-T_{\mathrm{LO}}}{\alpha \cdot \left(C_{\mathrm{p1}}+C_{\mathrm{p2}}\right) \cdot \beta \cdot R_{\mathrm{on}}}}\right) \right]^{-1} \tag{3.4}$$

For example, with 500fF of total parasitic capacitance and 2GHz operation, R_{Mix} would be 250Ω for a doubly-balanced mixer in a dual channel application.

The mixer voltage gain can be estimated by

$$A_{\mathrm{v}} \approx G_{\mathrm{m}} \cdot \frac{2}{\pi} \cdot R_{\mathrm{TIA}} \tag{3.5}$$

where, G_{m} is the transconductance of the preceding stage, and $2/\pi$ is the switching efficiency. For example, to obtain 25-35dB of gain with 20mS of transconductance,

R_{TIA} is calculated to be 2-5kΩ and the TIA noise will be amplified by a factor of 80-440 from (3.1). This factor could be reduced by moving to a smaller value of R_{TIA}, but this is problematic because,

- A smaller resistance results in a larger overall chip area, since the TIA feedback capacitance needs to be increased to maintain the same pole location.
- A larger capacitance will require a higher output current from the TIA, since the current requirement is proportional to the capacitance.
- A smaller resistance leads to a lower gain from (3.5).

Therefore, designing a very low noise TIA stage would be challenging, while simultaneously maintaining low power consumption and a small die area using the conventional approach. The next Section presents an improved mixer approach that minimizes this limitation.

3.2 Resistively Degenerated Passive Mixer

To avoid TIA noise amplification, the previous Section showed that it is essential to obtain a high mixer output impedance. But the output impedance of the mixer is limited by the operating frequency and parasitic capacitance, from (3.4). The proposed improved passive mixer with added resistance R_{deg} is shown in Fig. 3.3. The difference between the conventional and proposed passive mixer is illustrated in Fig. 3.4.

3.2.1 Increased Output Impedance

The proposed passive mixer can provide a higher equivalent mixer resistance by separating the parasitic capacitance of the G_{m} stage and mixer core. Then the equivalent

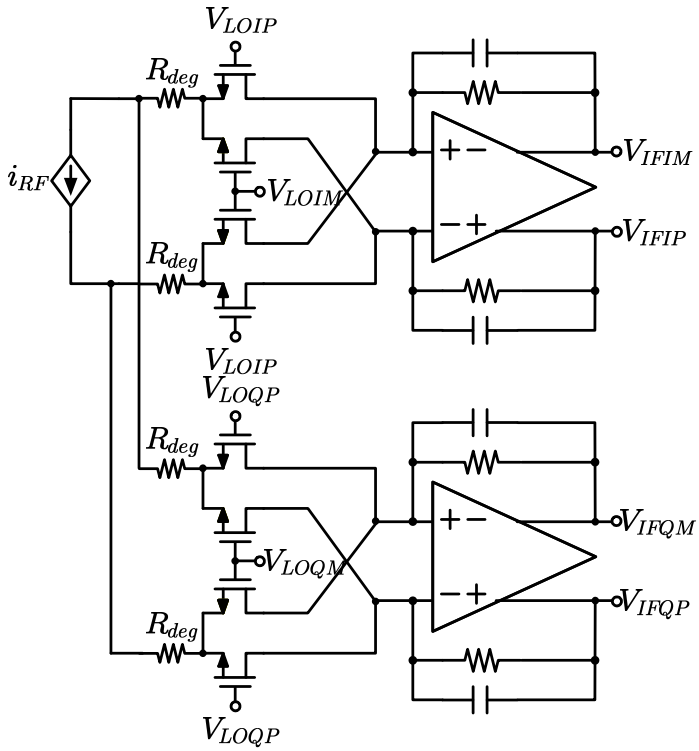

Figure 3.3: Proposed resistively degenerated passive mixer.

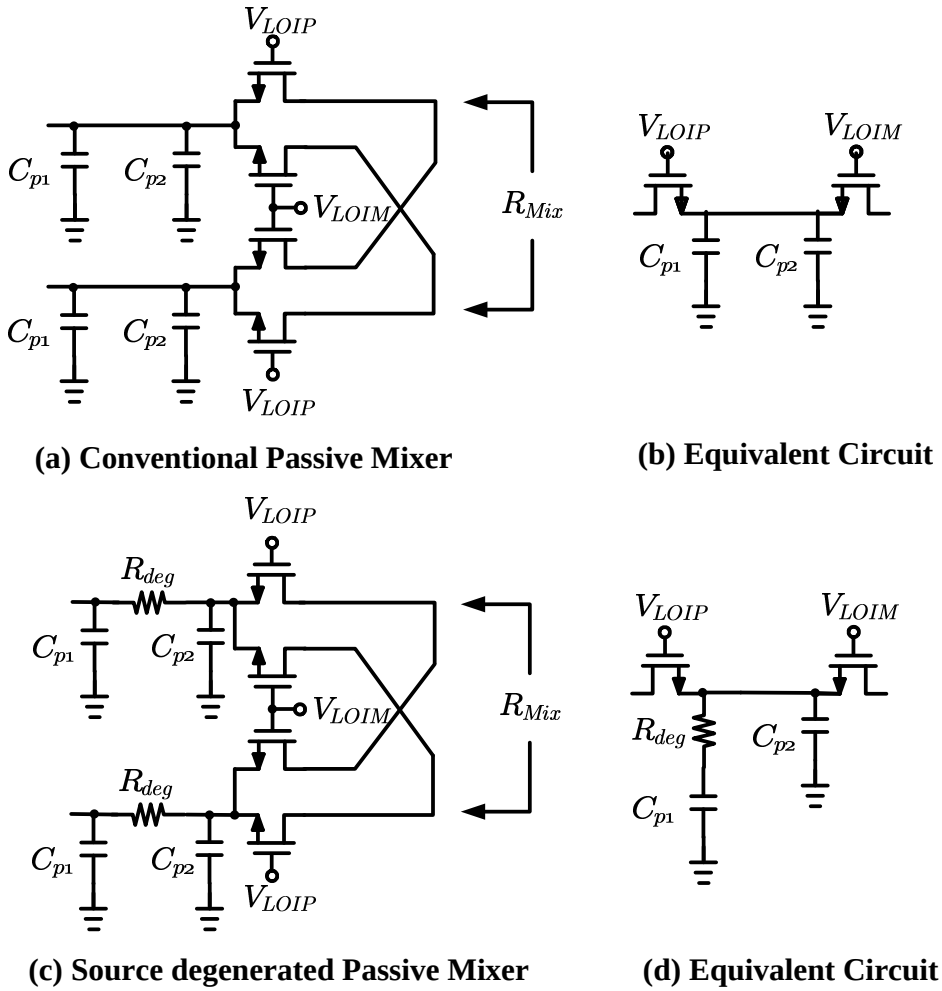

(a) Conventional Passive Mixer **(b) Equivalent Circuit**

(c) Source degenerated Passive Mixer **(d) Equivalent Circuit**

Figure 3.4: Difference between conventional and proposed mixer (a)conventional passive mixer (b)conventional passive mixer output impedance equivalent circuit (c)proposed resistively degenerated passive mixer (d)proposed mixer output impedance equivalent circuit.

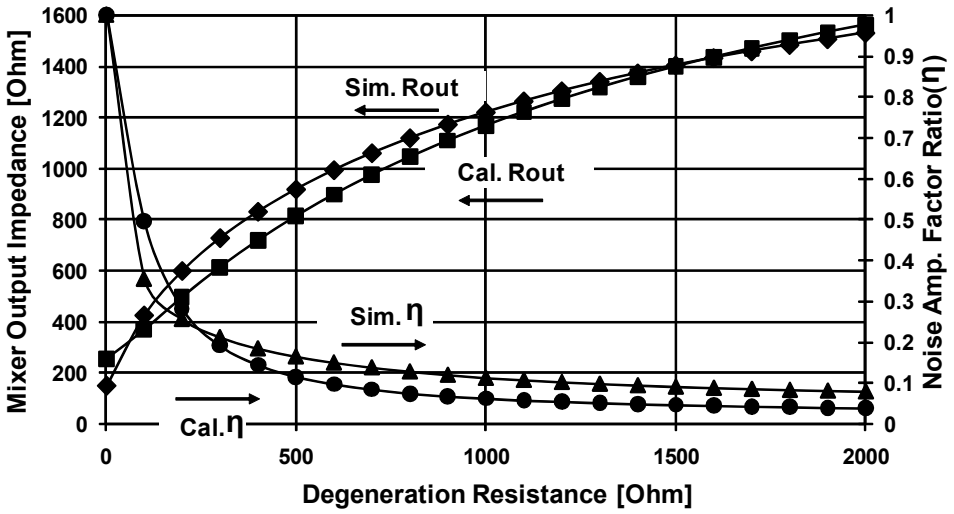

Figure 3.5: Simulated and calculated proposed mixer output impedance and noise amplification factor ratio at 2GHz.

resistance can be modified from (3.4) to be

$$R_{\mathrm{Mix}}(R_{\mathrm{deg}}) = [f_{\mathrm{LO}} \cdot \alpha \cdot [\, C_{\mathrm{p1}} \cdot \left(1 - e^{\frac{-T_{\mathrm{LO}}}{\alpha \cdot C_{\mathrm{p1}} \cdot \beta \cdot \left(R_{\mathrm{on}} + R_{\mathrm{deg}}\right)}}\right) + C_{\mathrm{p2}} \cdot \left(1 - e^{\frac{-T_{\mathrm{LO}}}{\alpha \cdot C_{\mathrm{p2}} \cdot \beta \cdot R_{\mathrm{on}}}}\right)]]^{-1} \tag{3.6}$$

As can be seen from (3.6), the equivalent mixer output resistance is increased by inserting R_{deg}. Usually, the parasitic capactiance(C_{p1}) from the preceding G_{m} stage is larger than the mixer core parasitic(C_{p2}), since the size of the mixer core is relatively small compared to the G_{m} stage due to speed considerations. Therefore, R_{Mix} can be boosted if the effect of C_{p1} can be minimized. Assuming the time constant formed by C_{p1} and R_{on}+R_{deg} is larger than the LO period, C_{p1} can be neglected and (3.6) can be approximated by

$$R_{\mathrm{Mix}}(R_{\mathrm{deg}}) \approx \left[f_{\mathrm{LO}} \cdot \alpha \cdot C_{\mathrm{p2}} \cdot \left(1 - e^{\frac{-T_{\mathrm{LO}}}{\alpha \cdot C_{\mathrm{p2}} \cdot \beta \cdot R_{\mathrm{on}}}}\right)\right]^{-1} \tag{3.7}$$

The noise amplification factor ratio(η) can be defined as the ratio of the proposed mixer's TIA noise amplification factor compared to that of the conventional mixer, i.e.

$$\eta(R_{\mathrm{deg}}) = \left(1 + \frac{2 \cdot R_{\mathrm{TIA}}}{R_{\mathrm{Mix}}(R_{\mathrm{deg}})}\right)^2 / \left(1 + \frac{2 \cdot R_{\mathrm{TIA}}}{R_{\mathrm{Mix}}(0)}\right)^2 \tag{3.8}$$

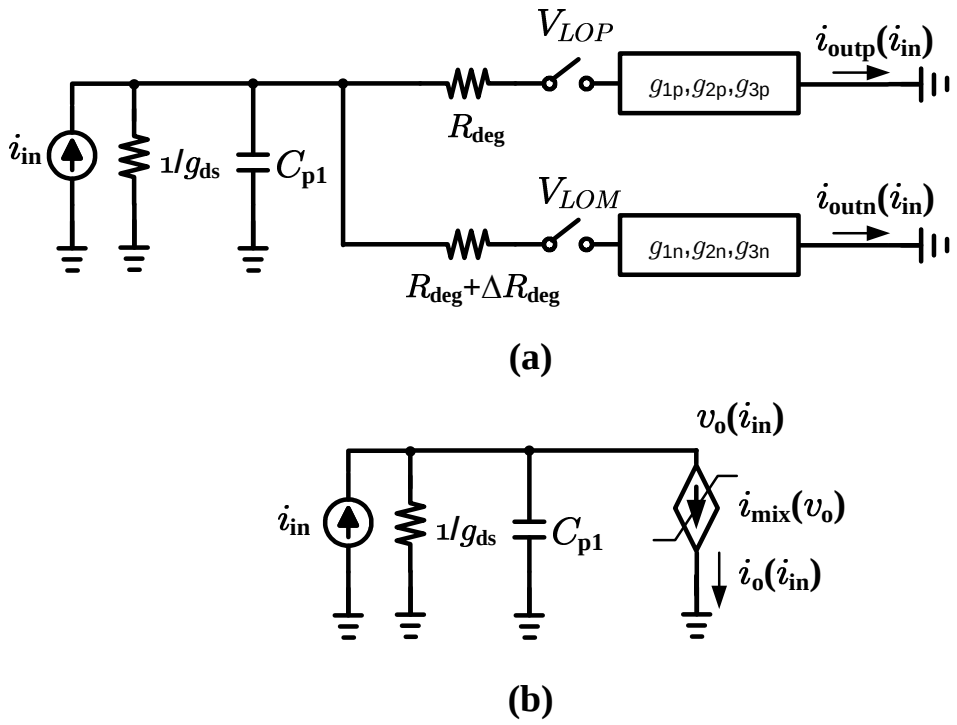

Figure 3.6: Equivalent circuit diagram for IM_2 calculation (a) full mixer model (b) simplified equivalent circuit.

Simulated and calculated results for the mixer output impedance and the TIA noise amplification factor ratio(η) are shown in Fig. 3.5. A 3.5kΩ feedback resistance($R_{\rm TIA}$) value is used to calculate η. As expected from (3.7), and shown in Fig. 3.5, the output impedance of the proposed passive mixer saturates at value detemined by (3.7) when $R_{\rm deg}$ is increased. The η decreases rapidly with increasing $R_{\rm deg}$, and reaches a limit when $R_{\rm deg} \geq 500\Omega$.

3.2.2 Improved IIP_2 Performance

Another issue is that the RF current from the preceding $G_{\rm m}$ stage cannot be split with perfect balance between the two paths of the mixer, due to mismatches in the mixer cores. This effect will cause strong second-order distortion in passive mixers [67]. By adding $R_{\rm deg}$, the current split can be better balanced(improving the second-order distortion), since a polysilicon resistor can be made with a large aspect ratio and excellent matching, which will reduce the overall resistance mismatch. Therefore, the

total resistance seen by the RF source at the mixer input would be proportional to $R_{\rm on} + R_{\rm deg}$. The variation of the *total* resistance can be smaller than a conventional passive mixer if $R_{\rm on} < R_{\rm deg}$.

A simplified first-order equivalent circuit used to calculate the $\rm IM_2$ product is shown in Fig. 3.6. In Fig. 3.6(a), the model assumes an ideal switch for the passive mixer, with turn-on resistance ($R_{\rm on}$) followed by a weakly nonlinear conductance, where the nonlinearity coefficient can be considered only up to 3rd order (g_1, g_2, g_3) [47]. The output drain-to-source conductance ($g_{\rm ds}$) and parasitic capacitance ($C_{\rm p1}$) models the output of the $G_{\rm m}$ stage. The FET mismatch between the two paths is modeled as a turn-on resistance difference ($\Delta R_{\rm on}$) [67] and the degeneration resistor mismatch is $\Delta R_{\rm deg}$. There is another nonlinear effect due to the finite rise and fall time difference, and the non-ideal duty-cycle of the LO [67]. But for this simplified analysis, an ideal 50% duty cycle non-overlapping rectangular waveform is assumed. Using Fig. 3.6(a), it can be shown that the leaked direct $\rm IM_2$ distortion at $\omega_1 - \omega_2$, due to the mismatch, dominates the frequency translated $\rm IM_2$ at $\omega_{\rm LO} - \omega_1 - \omega_{\rm LO} + \omega_2$ and $\omega_{\rm LO} + \omega_1 - \omega_{\rm LO} - \omega_2$. Based on this, along with the assumption of a non-overlapping rectangular LO waveform, the nonlinear model of the passive mixer for a single side (positive or negative) can be modeled as in Fig. 3.6(b), where the nonlinear conductance is modeled as a voltage-controlled current source. The linear degeneration resistance can be combined with the nonlinear coefficient of the switch to be expressed as

$$i_{\rm mix}(v_{\rm o}) = g_1 \cdot v_{\rm o} + g_2 \cdot v_{\rm o}^2 + g_3 \cdot v_{\rm o}^3 \tag{3.9}$$

The mismatch between the positive and negative sides of the mixer can be modeled by

$$g_{1\rm p} = \frac{1}{R_{\rm deg} + R_{\rm on}} \tag{3.10a}$$

$$g_{1\rm n} = \frac{1}{R_{\rm deg} + \Delta R_{\rm deg} + R_{\rm on} + \Delta R_{\rm on}} \tag{3.10b}$$

The nonlinear voltage ($v_{\rm o}(i_{\rm in})$) and output current ($i_{\rm o}(i_{\rm in})$) can be expressed as a Volterra Series, which is a function of the input current [47],

$$v_{\rm o}(i_{\rm in}) = A_1(s) \circ i_{\rm in} + A_2(s_1, s_2) \circ i_{\rm in}^2 + A_3(s_1, s_2, s_3) \circ i_{\rm in}^3 \tag{3.11a}$$

$$i_{\rm o}(i_{\rm in}) = C_1(s) \circ i_{\rm in} + C_2(s_1, s_2) \circ i_{\rm in}^2 + C_3(s_1, s_2, s_3) \circ i_{\rm in}^3 \tag{3.11b}$$

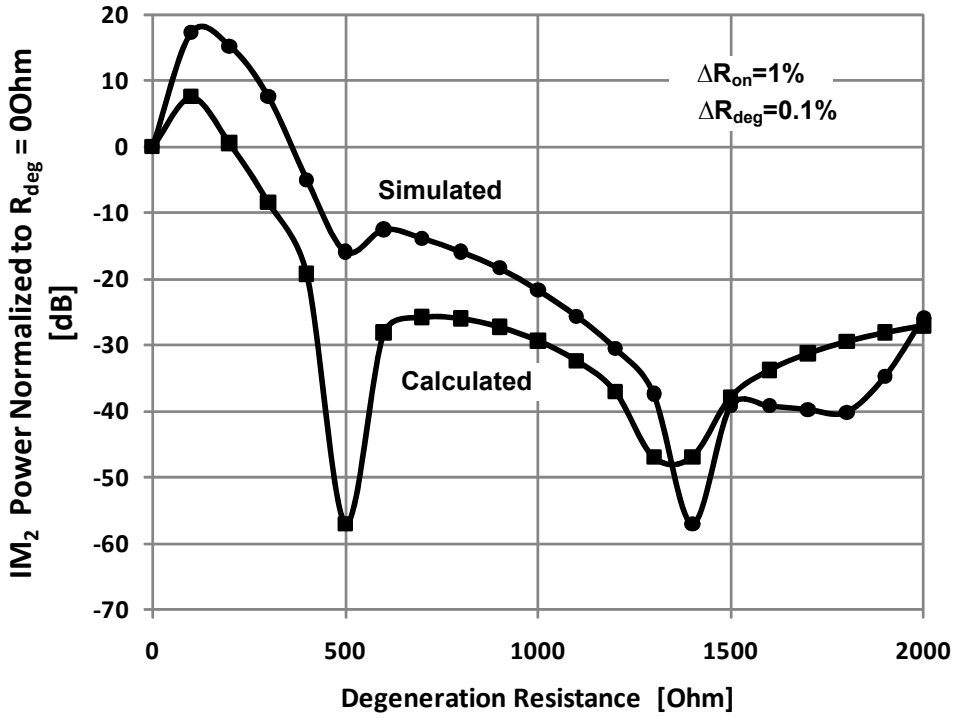

Figure 3.7: Calculated and simulated IM_2 improvement as a function of R_{deg} at 2GHz.

where $A_{\mathrm{n}}(s_1, s_2, \cdots, s_{\mathrm{n})})$ and $C_{\mathrm{n}}(s_1, s_2, \cdots, s_{\mathrm{n})})$ are the Laplace transforms of the n-th order Volterra kernels. For the IM_2 calculation, only the second-order Volterra kernel ($C_2(s_1, s_2)$) needs to be calculated. Using the nodal equation and excitation method in [47], and assuming $\omega_1 \approx \omega_2 \approx \omega_3$ and $\Delta\omega(= \omega_1 - \omega_2) \approx 0$, the second-order Volterra kernels for each mixer branch are

$$C_{2\mathrm{p}}(j\omega_1, -j\omega_2) = \frac{g_{1\mathrm{p}}}{g_{1\mathrm{p}} + g_{\mathrm{ds}}} \cdot \left(\frac{g_{2\mathrm{p}}}{\left(g_{1\mathrm{p}} + g_{\mathrm{ds}}\right)^2 + \left(\omega_1 \cdot C_{\mathrm{p1}}\right)^2} \right) \tag{3.12a}$$

$$C_{2\mathrm{n}}(j\omega_1, -j\omega_2) = \frac{g_{1\mathrm{n}}}{g_{1\mathrm{n}} + g_{\mathrm{ds}}} \cdot \left(\frac{g_{2\mathrm{n}}}{\left(g_{1\mathrm{n}} + g_{\mathrm{ds}}\right)^2 + \left(\omega_1 \cdot C_{\mathrm{p1}}\right)^2} \right) \tag{3.12b}$$

From (3.12), the differential second-order Volterra kenel (which determines the IM_2) is given by

$$\begin{aligned} C_{2,\mathrm{diff}}(j\omega_1, -j\omega_2) = \Bigg[& \frac{g_{1\mathrm{p}}}{g_{1\mathrm{p}} + g_{\mathrm{ds}}} \cdot \left(\frac{g_{2\mathrm{p}}}{\left(g_{1\mathrm{p}} + g_{\mathrm{ds}}\right)^2 + \left(\omega_1 \cdot C_{\mathrm{p1}}\right)^2} \right) \\ & - \frac{g_{1\mathrm{n}}}{g_{1\mathrm{n}} + g_{\mathrm{ds}}} \cdot \left(\frac{g_{2\mathrm{n}}}{\left(g_{1\mathrm{n}} + g_{\mathrm{ds}}\right)^2 + \left(\omega_1 \cdot C_{\mathrm{p1}}\right)^2} \right) \Bigg] \end{aligned} \tag{3.13}$$

This result can be used to predict the improvement in IM_2 as a function of $R_{\rm deg}$ and a given mismatch. The predicted and simulated improvement of IM_2 as a function of $R_{\rm deg}$ is plotted in Fig. 3.7. The turn-on resistance mismatch is assumed to be 1% for median device size [68], and the $R_{\rm deg}$ mismatch is assumed to be 0.1%. As can be seen, the trends in the calculated IM_2 improvement in (3.13) agree well with the trends in the simulated improvement, and clearly demonstrates the improvement in IM_2 with the new approach, when the degeneration resistance is larger than 400Ω.

3.2.3 Limitation of Using Large Degeneration Resistance ($R_{\rm deg}$)

Even though the degeneration resistance($R_{\rm deg}$) is helpful for improving NF and IIP_2 performance, the value of degeneration resistance cannot be increased indefinitley due to following reasons.

- The signal path gain will decrease with larger $R_{\rm deg}$, since the RF current entering the mixer from the $G_{\rm m}$ stage will be decreased, due to higher mixer input impedance ($R_{\rm on}$+$R_{\rm deg}$).
- The extra resistor in the RF path can generate a large signal swing at the mixer input and degrade linearity.
- The degeneration resistor itself generates additional thermal noise, with a larger resistance value.

Therefore, there is an optimum $R_{\rm deg}$ value based on the preceding $G_{\rm m}$ stage output impedance and the mixer core turn-on resistance. The design procedure to choose the optimum $R_{\rm deg}$ value will be discussed in the next Section.

3.3 Mixer Design

The complete simplified mixer schematic is shown in Fig. 3.8. It consists of an input transconductance stage, the resistively degenerated passive mixer core, and a TIA.

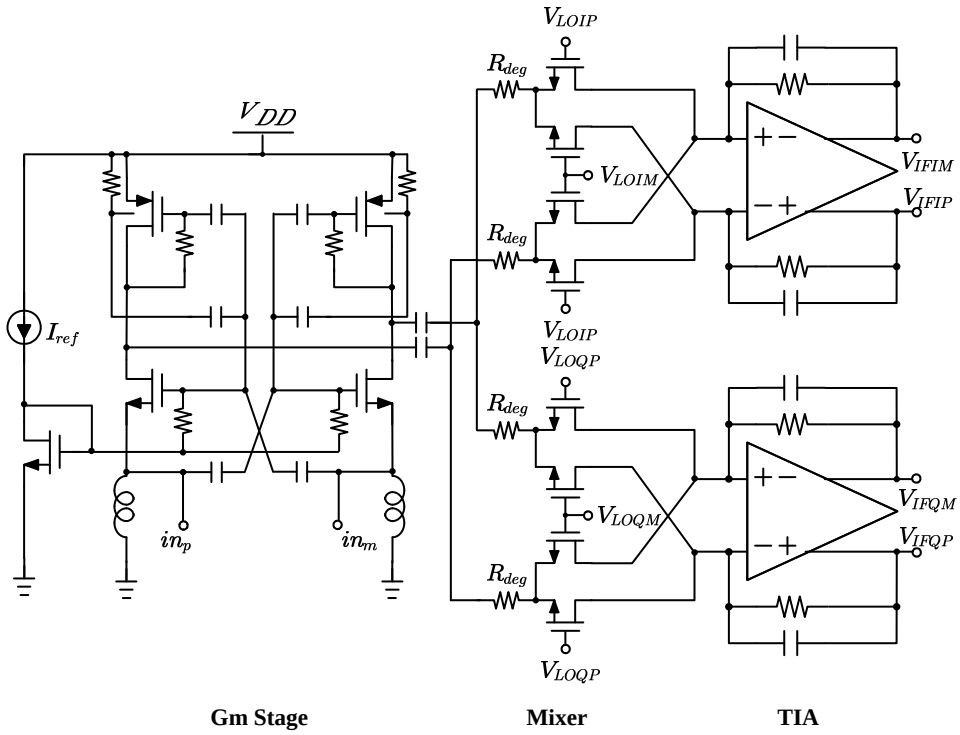

Figure 3.8: Simplified schematic diagram of the mixer.

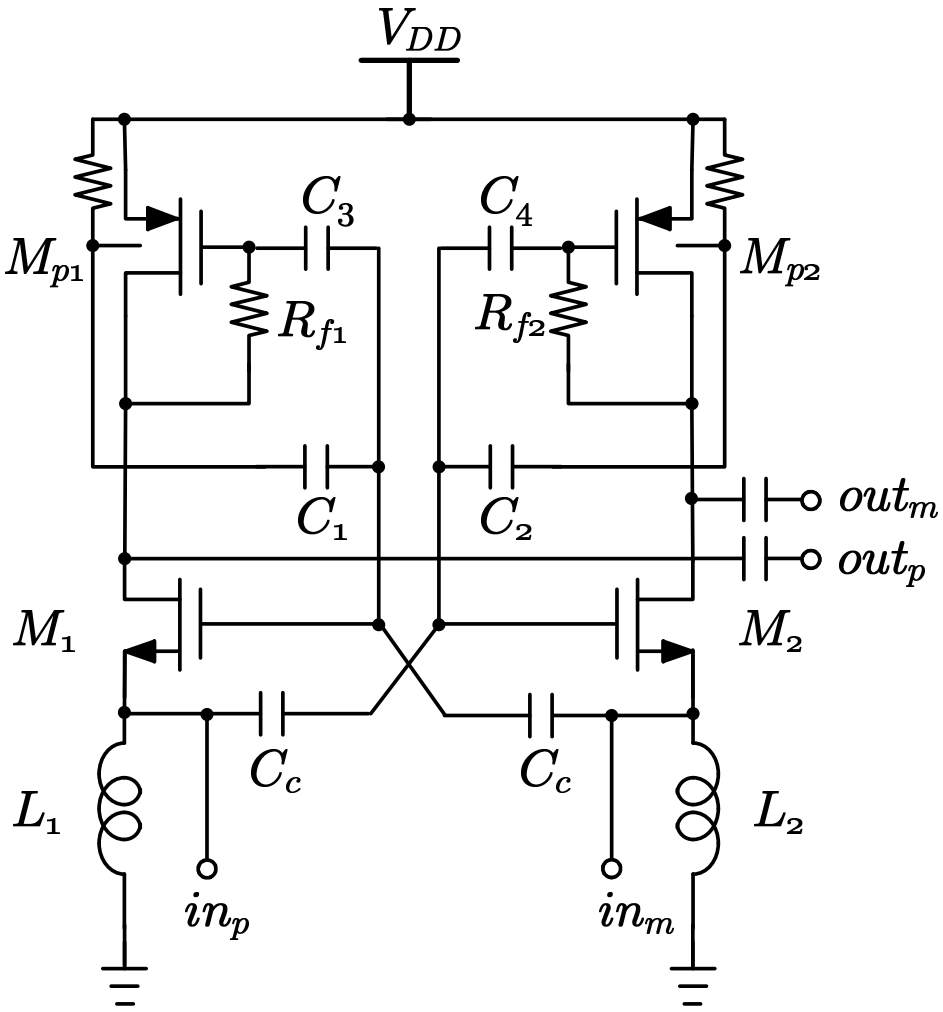

Figure 3.9: Simplified schematic of the transconductance stage.

3.3.1 Transconductance Stage

The transconductance (G_{m}) stage converts the RF input voltage to current. Due to the wideband (1.55G-2.2GHz) operation requirement, the input stage is designed with a Common Gate (CG) topology. The CG input stage can provide wideband operation, due to its resistive input impedance, but there is a NF penalty. To improve the NF performance of the CG stage, the cross-coupled method is used [69]. But the cross-coupled method can boost the G_{m} by only a factor of two at best.

The G_{m} can be boosted further with a current reuse complementary input stage,

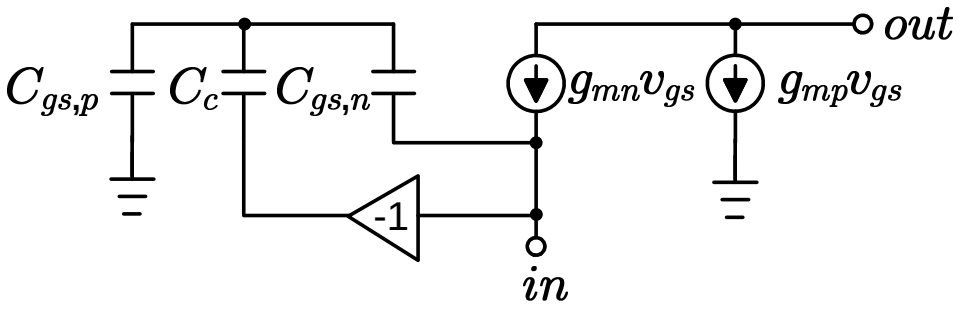

Figure 3.10: Equivalent schematic of the transconductance stage used to calculate input impedance and effective transconductance.

and back-gate connection, as shown in Fig. 3.9. Transistor M_1 and M_2 provide transconductance and input matching, M_{p1} and M_{p2} are input PFET transistors, which provide additional transconductance without consuming extra current, C_c is an input cross-coupling capacitor, R_f is a self-bias resistor for the PFETs, and L_1 is the bias choke inductor. The half equivalent circuit of the G_{m} stage is shown in Fig. 3.10. From Fig. 3.10, it can be shown that the input impedance of the proposed Gm stage is

$$Z_{\mathrm{in}}(j\omega) = \frac{1}{[1-A]\cdot[g_{\mathrm{m,n}} + j\omega C_{\mathrm{gs,n}}] + [1+A]\cdot j\omega C_{\mathrm{c}}} \tag{3.14}$$

where, $g_{\mathrm{m,n}}$ is the transconductance of the NFET, $C_{\mathrm{gs,n}}$ is the gate-to-source capacitance of the NFET, $C_{\mathrm{gs,p}}$ is the gate-to-source capacitance of the PFET, C_{c} is the coupling capactiance from the negative input side, and A is the voltage transfer function from the input to the gate of the NFET and PFET and is given by

$$A \cong -\frac{C_{\mathrm{c}} - C_{\mathrm{gs,n}}}{C_{\mathrm{gs,n}} + C_{\mathrm{gs,p}} + C_{\mathrm{c}}} \tag{3.15}$$

If C_c is zero, A becomes positive, which means that the gate voltage will have a portion of the source voltage superimposed on it, which will degrade the transconductance. However, assuming C_{c} is very large, then, $A \approx -1$ and $Z_{\mathrm{in}}(j\omega)$ is

$$Z_{\mathrm{in}}(j\omega) \approx \frac{1}{2\cdot[g_{\mathrm{m,n}} + j\omega C_{\mathrm{gs,n}}]} \tag{3.16}$$

It is clear from (3.16) that the transconductance and input capacitance is increased by a

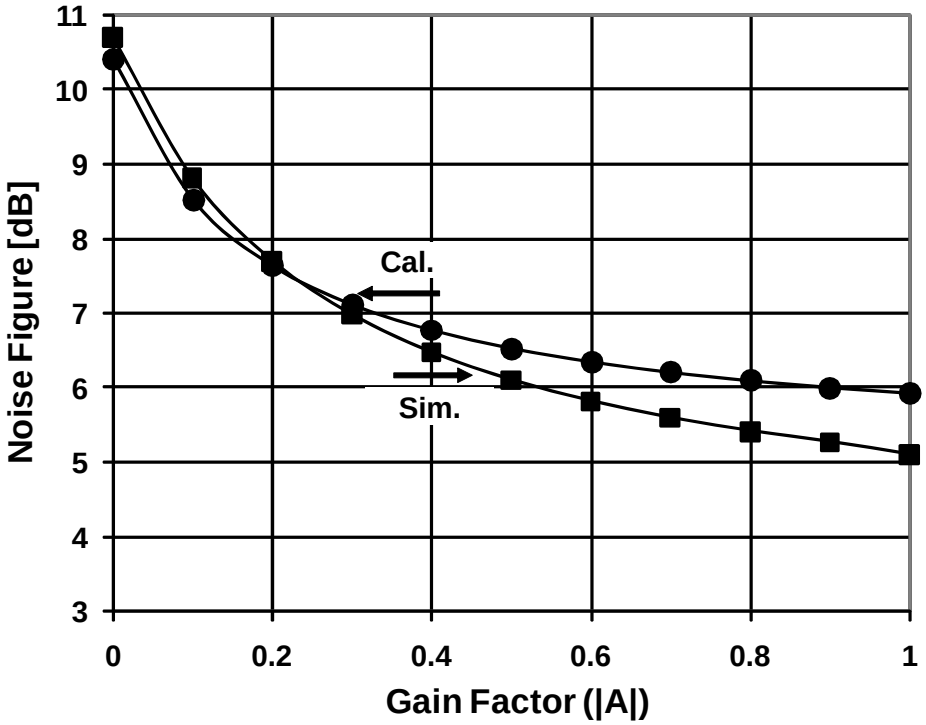

Figure 3.11: Calculated and simulated NF of transconductance stage at 2GHz.

factor of two. The total transconductance ($G_{\mathrm{m,eff}}$) of the G_m stage is therefore,

$$G_{\mathrm{m,eff}} \approx g_{\mathrm{m,n}} \cdot [1 - A] - g_{\mathrm{m,p}} \cdot A \tag{3.17}$$

With the assumption of infinite C_{c} and $g_{\mathrm{m,n}} \approx g_{\mathrm{m,p}}$, the $G_{\mathrm{m,eff}}$ can be three times the conventional CG stage [70].

Neglecting the FET gate induced noise for FETs and assuming an input matching condition of $R_s \approx 1/\left(g_{\mathrm{m,n}} \cdot (1 - A)\right)$, the noise factor of the proposed transconductance stage can be expressed as

$$F_{\mathrm{Gm}} = 1 + \frac{\gamma \cdot (g_{\mathrm{d0,n}} + 4 \cdot g_{\mathrm{d0,p}})}{g_{\mathrm{m,n}} \cdot \left(\frac{1}{1-A} - 4 \cdot A\right)} \tag{3.18}$$

where, γ is bias dependent constant, which is usually 2/3 for long-channel device [20], and g_{d0} is drain-source conductance at V_{DS}=0. Equation (3.18) can be modified further, if $g_{\mathrm{d0,n}} \approx g_{\mathrm{d0,p}}$,

$$F_{\mathrm{Gm}} \approx 1 + 5 \cdot \gamma \frac{g_{\mathrm{d0,n}}}{g_{\mathrm{m,n}}} \cdot \frac{1}{\frac{1}{1-A} - 4 \cdot A} \tag{3.19}$$

The calculated and simulated noise figure of transconductance stage is shown in Fig. 3.11, where γ =2 is used to account for the short-channel device effect [20]. As can be seen, the calculated and simulated values agree well and the noise factor of the CG transconductance stage can be significantly improved.

The coupling capacitor at the output of the G_{m} stage is used to block any low-frequency IM_2 components and low-frequency noise from the transconductance stage from reaching the mixer core.

3.3.2 Mixer Core Stage

Due to the superior noise and IIP_2 performance compared to the conventional mixer, as explained in Section III, the resistively degenerated passive mixer is used as the mixer core structure. Thanks to the use of a triple-well process, the back-gate of the switching core is biased at the same voltage as the source node to minimize the body effect. As mentioned in Section III, the degeneration resistance value needs to be optimized for best NF and gain performance. The overall gain of the mixer, as a function of R_{deg}, from the transconductance stage input to the TIA output is

$$G(R_{\mathrm{deg}}) \approx \frac{2}{\pi} \cdot \ G_{\mathrm{m,eff}} \cdot \left| \frac{4 \cdot Z_{\mathrm{out}}}{R_{\mathrm{deg}} + R_{\mathrm{on}} + 4 \cdot Z_{\mathrm{out}}} \right| \cdot R_{\mathrm{TIA}} \tag{3.20}$$

where, Z_{out} is the output impedance of the transconductance stage at the input frequency with parasitic capacitance(C_{p1}), which is assumed to be 80% of total parasitic capacitance, and the factor of four comes from the four parallel connections of the passive mixers in an I/Q doubly balanced mixer. .

The noise factor ratio (F(R_{deg})/F(0), the ratio of the mixer noise factor with and without degeneration resistance) of the complete mixer can be derived using noise equivalent circuit, as shown in Fig. 3.12. The noise from the transconductance stage is assumed to be the same for both conventional and degenerated passive mixers. The $\overline{v_{\mathrm{s}}^2}$ represents the source and input referred transconductance noise. The output noise due to $\overline{v_{\mathrm{s}}^2}$ can be expressed as

$$\overline{v_{\mathrm{s,out}}^2} = \overline{v_{\mathrm{s}}^2} \cdot |G(R_{\mathrm{deg}})|^2 \tag{3.21}$$

where, $G(R_{\mathrm{deg}})$ is given by (3.20).

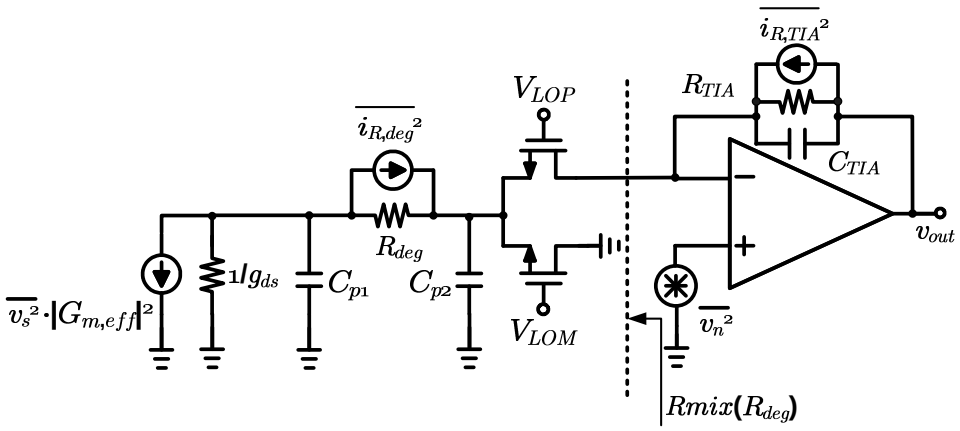

Figure 3.12: Simplified noise equivalent circuit.

The TIA noise($\overline{v_{\rm n}^2}$) at the output is

$$\overline{v_{\rm n,out}^2} = \overline{v_{\rm n}^2} \cdot \left[1 + \frac{2 \cdot R_{\rm TIA}}{R_{\rm Mix}(R_{\rm deg})}\right]^2 = \overline{v_{\rm n}^2} \cdot \epsilon(R_{\rm deg}) \tag{3.22}$$

Assuming $R_{\rm on} << R_{\rm deg}$, which is the case here since $R_{\rm on} = 30\Omega$ and $R_{\rm deg} = 600\Omega$, the noise contribution due to $R_{\rm on}$ can be ignored. The noise current from $R_{\rm deg}$ and $R_{\rm TIA}$ are given by

$$\overline{i_{\rm R_{deg},out}^2} = \frac{4 \cdot kT \cdot \Delta f}{R_{\rm deg}} \cdot \left|\frac{2 \cdot R_{\rm TIA}}{1 + j\omega \cdot C_{\rm TIA} \cdot R_{\rm TIA}}\right|^2 \tag{3.23a}$$

$$\overline{i_{\rm R_{TIA},out}^2} = \frac{4 \cdot kT \cdot \Delta f}{R_{\rm TIA}} \cdot \left|\frac{2 \cdot R_{\rm TIA}}{1 + j\omega \cdot C_{\rm TIA} \cdot R_{\rm TIA}}\right|^2 \tag{3.23b}$$

and the transimpedance stage is given by

$$Z_{\rm TIA}(j\omega) = \frac{2 \cdot R_{\rm TIA}}{1 + j\omega \cdot C_{\rm TIA} \cdot R_{\rm TIA}} \tag{3.24}$$

The noise factor without the degeneration resistance is

$$F(R_{\rm deg} = 0) = \frac{\overline{v_{\rm s}^2} \cdot |G(0)|^2 + \overline{i_{\rm R_{TIA}}^2} \cdot |Z_{\rm TIA}|^2 + \overline{v_{\rm n}^2} \cdot \epsilon(0)}{\overline{v_{\rm s}^2} \cdot |G(0)|^2} \tag{3.25}$$

and the noise factor with degeneration resistance is

$$F(R_{\rm deg}) = \frac{\overline{v_{\rm s}^2} \cdot |G(R_{\rm deg})|^2 + \left[\overline{i_{\rm R_{TIA}}^2} + \overline{i_{\rm R_{deg}}^2}\right] \cdot |Z_{\rm TIA}|^2 + \overline{v_{\rm n}^2} \cdot \epsilon(R_{\rm deg})}{\overline{v_{\rm s}^2} \cdot |G(R_{\rm deg})|^2} \tag{3.26}$$

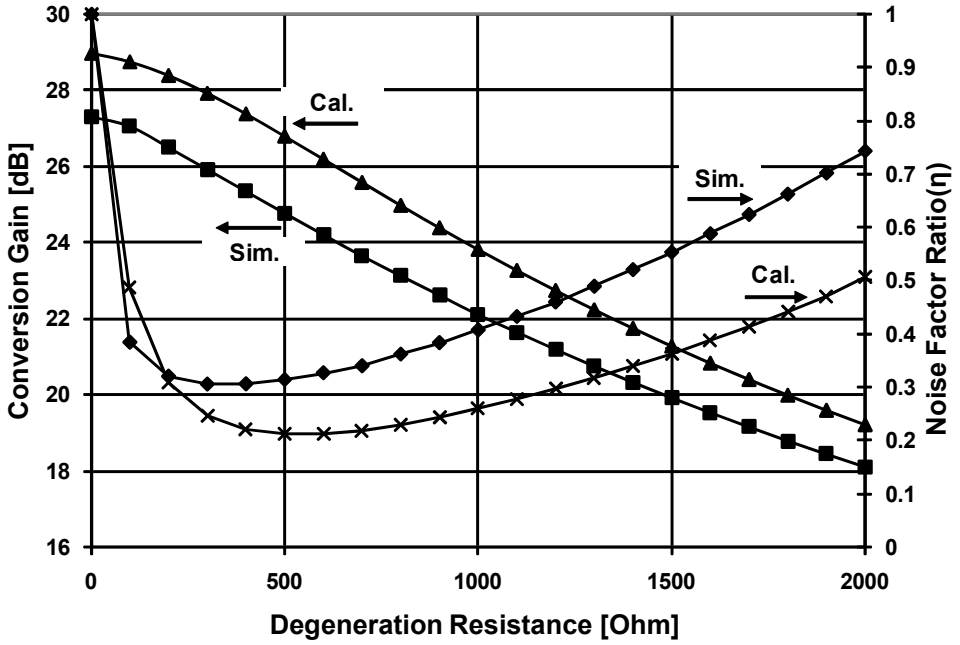

Figure 3.13: Calculated and simulated total gain and noise factor ratio of the mixer at 2GHz.

The noise factor ratio($F_{\rm r}(R_{\rm deg})$) is defined as $F(R_{\rm deg})/F(0)$ and is given by

$$F_{\rm r}(R_{\rm deg}) = \frac{\overline{v_{\rm s}^2}\cdot|G(R_{\rm deg})|^2 + \left[\overline{i_{\rm R_{deg}}^2} + \overline{i_{\rm R_{TIA}}^2}\right]\cdot|Z_{\rm TIA}|^2 + \overline{v_{\rm n}^2}\cdot\epsilon(R_{\rm deg})}{\frac{|G(R_{\rm deg})|^2}{|G(0)|^2}\cdot\left[\overline{v_{\rm s}^2}\cdot|G(0)|^2 + \overline{i_{\rm R_{TIA}}^2}\cdot|Z_{\rm TIA}|^2 + \overline{v_{\rm n}^2}\cdot\epsilon(0)\right]} \tag{3.27}$$

where, $\epsilon(R_{\rm deg})$ is defined by

$$\epsilon(R_{\rm deg}) = \left(1 + \frac{2\cdot R_{\rm TIA}}{R_{\rm Mix}(R_{\rm deg})}\right)^2 \tag{3.28}$$

In the derivation of (3.27), the noise contribution of the switch core is ignored due to a small average turn-on resistance [71]. The overall gain and noise factor ratio, with various values of $R_{\rm deg}$, are plotted in Fig. 3.13 with simulated values for comparison purpose. The optimal $R_{\rm deg}$ is between 300Ω and 600Ω, where the NF is minimized but the gain is still acceptable. The $\rm IIP_3$ performance of mixer switching core itself is simulated and the result is shown in Fig. 3.14, which demonstrates the improvement with the added degeneration resistance. A degeneration resistance of 600Ω was chosen,

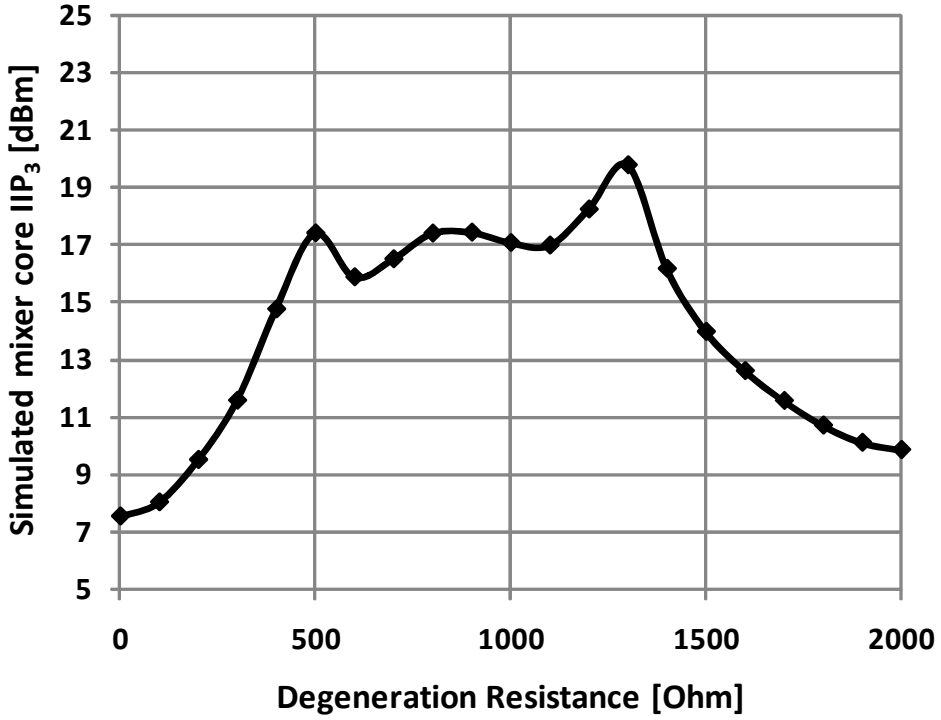

Figure 3.14: Simulated IIP_3 performance of mixer switch core as a function of R_{deg} at 2GHz.

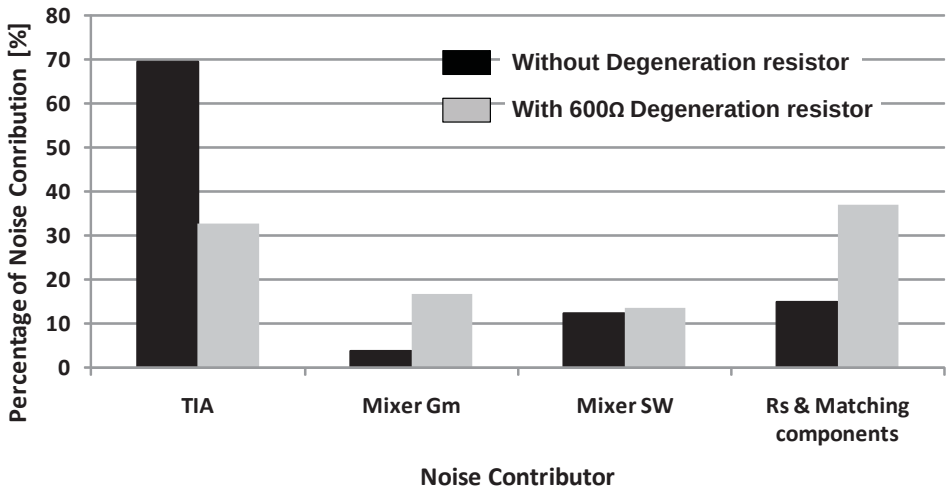

Figure 3.15: Simulated noise contribution from TIA, mixer switch, source resistance (R_{S}), matching components, and G_{m} stage with and without 600Ω degeneration resistance at 2GHz.

based on simulation results. The simulated noise contributions with and without the 600Ω of degeneration resistance are shown in Fig. 3.15. As can be seen, the noise contribution of the TIA stage is reduced to less than 35% of the total, compared to 70% without the degeneration resistance. The total integrated output noise voltage over 1MHz bandwidth is $6.8 \times 10^{-9}V^2$ without degeneration resistance and $1 \times 10^{-9}V^2$ with degeneration resistance, respectively.

3.3.3 Transimpedance Stage

The TIA stage serves as a mixer load, current-to-voltage converter, and anti-aliasing filter for the following stage. The active-RC TIA stage will provide a very low impedance at the mixer output, so that nearly all the current from the mixer core flows into the feedback RC. This ensures highly linear mixer operation, since the mixer encounters a small voltage swing [59]. But this assumption is only true when the operational transconductance amplifier (OTA) has sufficient gain at the highest possible frequency. The noise from the TIA stage also has to be small, so as to not corrupt the overall NF of the mixer, as explained in previous sections. The flicker noise from the TIA is the dominant noise contributor in narrow-band communication systems. Therefore, the area of the TIA input FETs needs to be large. But this requirement will increase the input parasitic capacitance. The TIA transfer function can be derived from Fig. 3.16. In Fig. 3.16(a),

$$i_{\mathrm{in}} = j\omega \cdot C_{\mathrm{gs}} \cdot v_{\mathrm{a}} + \frac{v_{\mathrm{a}} - v_{\mathrm{out}}}{Z_{\mathrm{f}}(j\omega)} \tag{3.29a}$$

$$\frac{v_{\mathrm{a}} - v_{\mathrm{out}}}{Z_{\mathrm{f}}(j\omega)} = \frac{v_{\mathrm{out}} + v_{\mathrm{a}} \cdot A(j\omega)}{Z_{\mathrm{out}}(j\omega)} \tag{3.29b}$$

where, C_{gs} is the input parasitic capacitance of the OTA, Z_{out} is the output impedance of the OTA, Z_{f} is the feedback impedance of TIA, and $A(j\omega)$ is the OTA open-loop voltage gain. The OTA is assumed to be a compensated two-stage amplifier, where C_{c} is the compensation capacitance, and shown in Fig. 3.16(b). The output impedance of the OTA is

$$Z_{\mathrm{out}}(j\omega) = \frac{Z_{\mathrm{out2}}(j\omega)}{1 + \frac{j\omega \cdot C_{\mathrm{c}} \cdot Z_{\mathrm{out2}}(j\omega) \cdot [1 + g_{\mathrm{m2}} \cdot Z_{\mathrm{out1}}(j\omega)]}{1 + j\omega \cdot C_{\mathrm{c}} \cdot Z_{\mathrm{out1}}(j\omega)}} \tag{3.30}$$

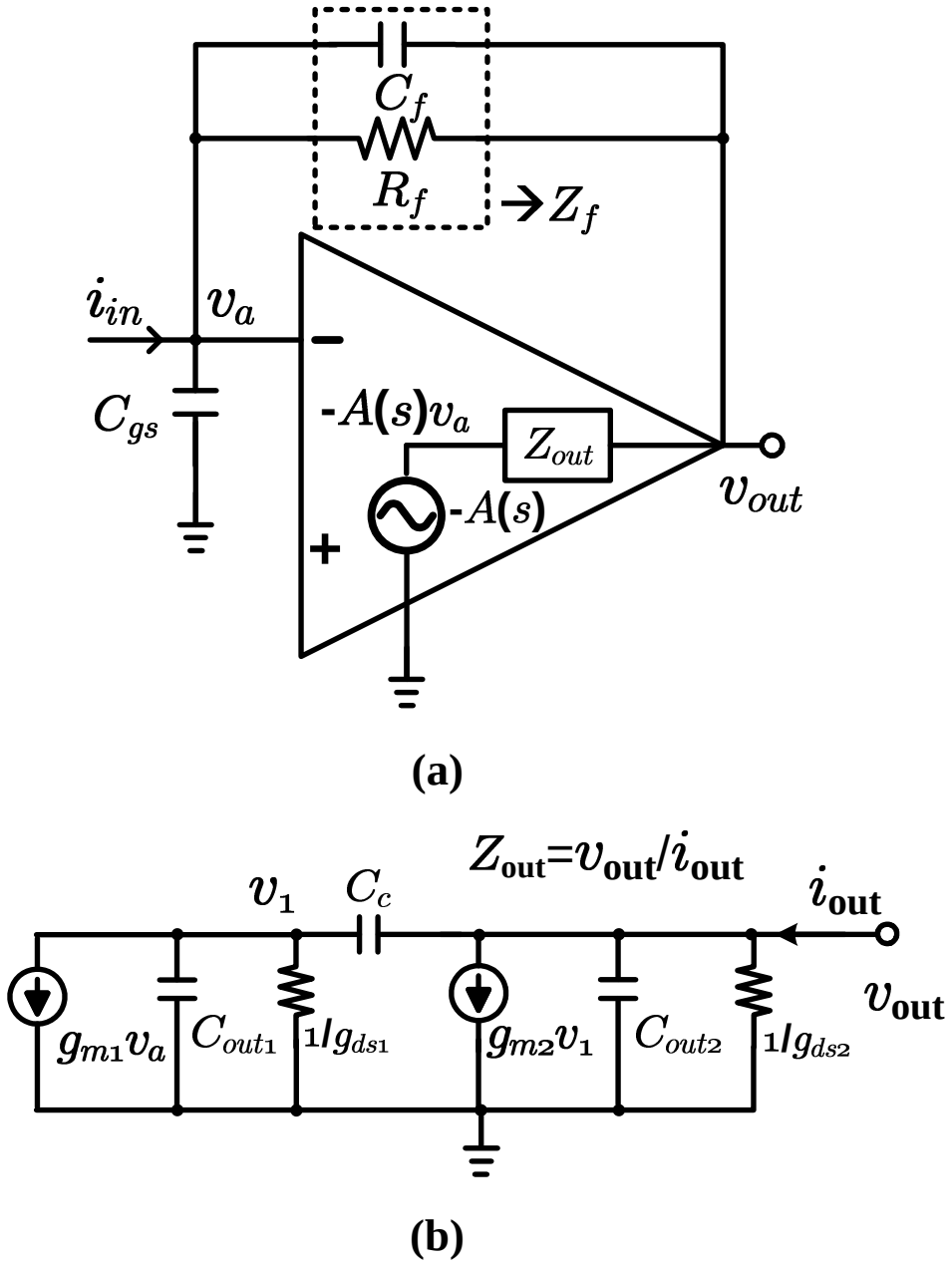

Figure 3.16: Effect of the OTA non-ideality on TIA transfer function. (a)Non-ideal TIA model including finite gain, input parasitic capacitance, and finite output impedance (b) Two-stage OTA equivalent circuit.

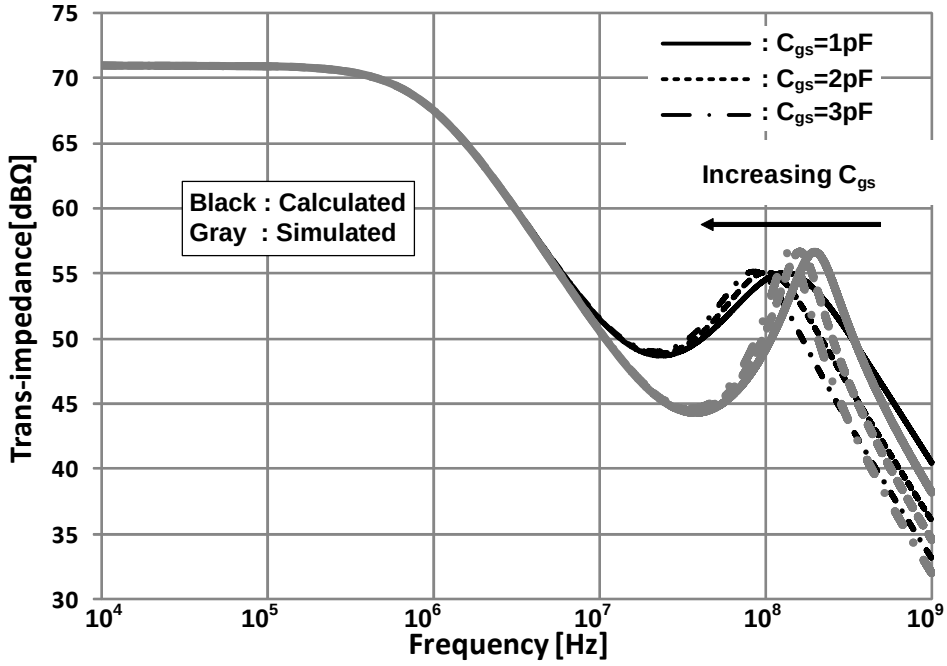

Figure 3.17: Calculated TIA transfer function with the Cgs value of 1pF-3pF.

where, $Z_{\rm out1}(j\omega) = (g_{\rm ds1} + j\omega \cdot C_{\rm out1})^{-1}$ and $Z_{\rm out2}(j\omega) = (g_{\rm ds2} + j\omega \cdot C_{\rm out2})^{-1}$. By inserting (3.30) and (3.29b) into (3.29a), the TIA transfer function($v_{\rm out}/i_{\rm in}$) is

$$H_{\rm TIA}(j\omega) = \frac{Z_{\rm out}(j\omega) - Z_{\rm f}(j\omega) \cdot A(j\omega)}{j\omega \cdot C_{\rm gs} \cdot [Z_{\rm out}(j\omega) + Z_{\rm f}(j\omega)] + A(j\omega) + 1} \tag{3.31}$$

The calculated and simulated transimpedance of the TIA are plotted in Fig. 3.17 as a function of the input frequency, with different values of $C_{\rm gs}$. It is shown that increasing $C_{\rm gs}$ moves the out-of-band peaking to a lower frequency and reduces filtering. This could be a significant problem depending on the application. For most Cellular applications, gain peaking above 100MHz is tolerable, since the Tx leakage will be at an offset of 45MHz or 80MHz, for Cellular and PCS bands, respectively.

3.4 Measured results

The downconverter was fabricated in a 0.18μm Si CMOS 5M1P process, and a chip microphotograph is shown in Fig. 3.18. The downconverter is part of a direct con-

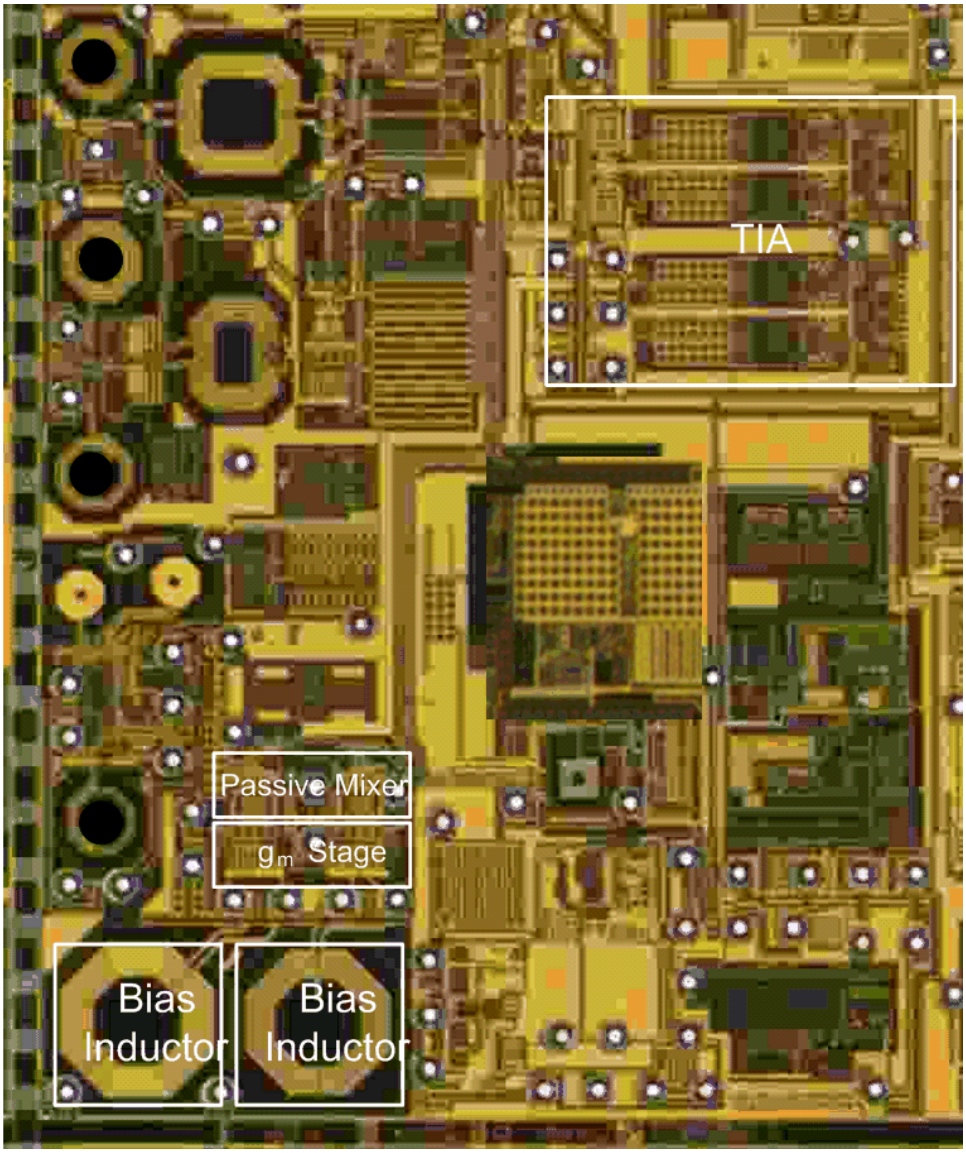

Figure 3.18: Chip microphotograph.

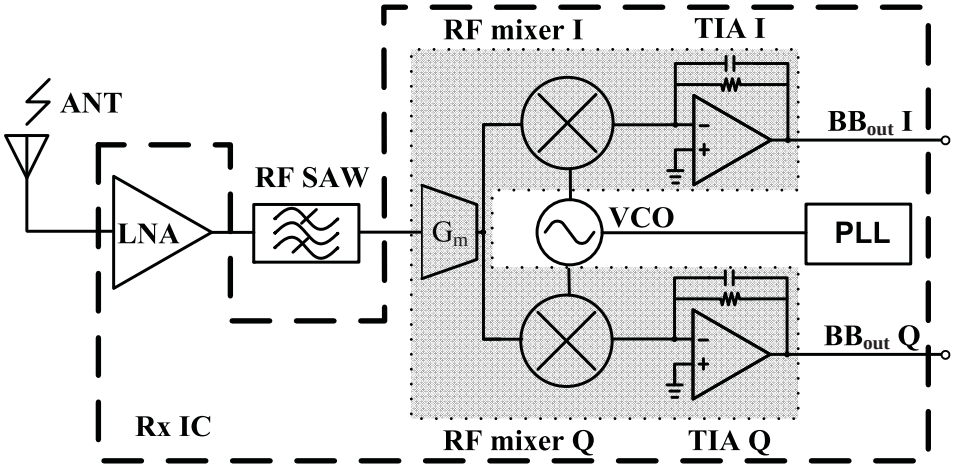

Figure 3.19: Receiver block diagram; shadowed area is this design.

version receiver system with an inter-stage SAW filter between the LNA and mixer.The block diagram of the receiver is shown in Fig. 3.19. All the measurements are done at the mixer input port, since the LNA can be bypassed. The input matching condition is measured with a Network Analyzer, and is shown in Fig. 3.20. The matching is done with single series inductor for each positive and negative input. As can be seen, the -10dB S_{11} input matching bandwidth is from 1.35GHz to 2.3GHz. The difference between the measured and simulated result is due to the higher parasitics of the test socket. To measure multiple devices, the evaluation board adopted a test socket, which has larger parasitic inductance and capacitance compared to a solder down board. The gain and NF performance are measured from 1.55GHz to 2.3GHz. The noise performance is measured using the Excess Noise Ratio (ENR) method [72]. The ENR used in the measurement was 20dB and the output noise power spectrum is measured at baseband with a Vector Signal Analyzer (VSA). The measured noise performance shows less than 9.5dB of DSB NF across the band. A large-signal noise figure, or so-called blocking noise figure, is defined as the noise figure in the presence of a large blocking/jammer signal. The noise performance in this situation is usually dominated by reciprocal mixing [19]. The close-in jammer signal at the mixer input can be as large as -16dBm in a

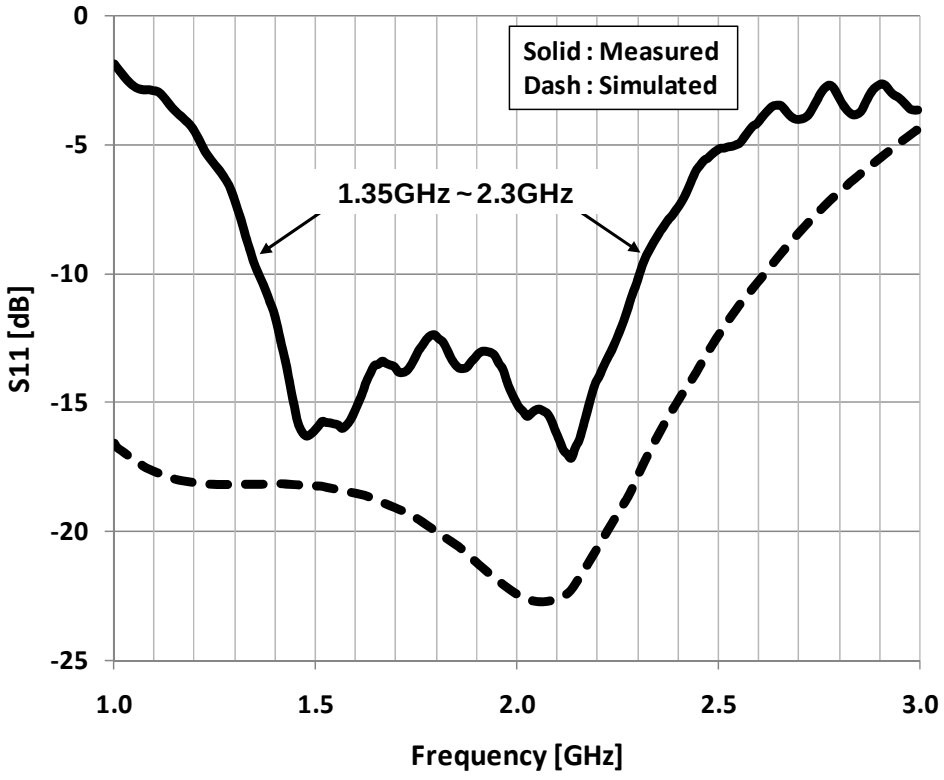

Figure 3.20: Measured input matching condition.

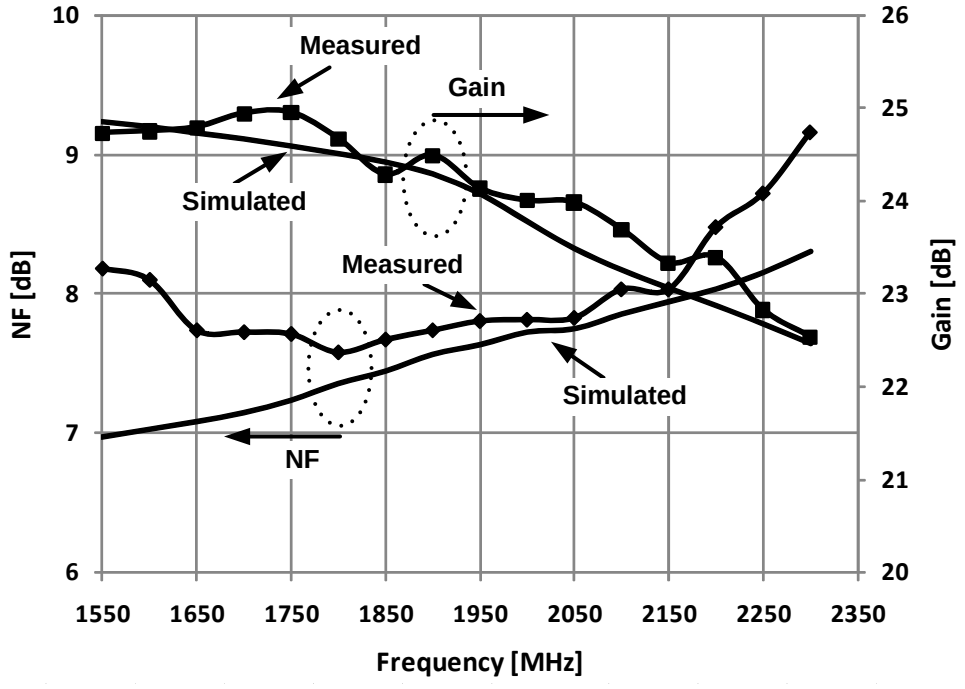

Figure 3.21: Measured and simulated gain and NF performance.

CDMA system, since the jammer level at the LNA input is -30dBm with 15dB of LNA power gain, followed by 1dB loss in the SAW filter [18]. With the assumption of -75dBc of integrated phase noise from the VCO and a -16dBm jammer, the large-signal noise figure of the mixer can be calculated

$$NF_{\mathrm{LS}} = 10 \cdot \log_{10}\left(1 + \frac{10^3 \cdot kT \cdot B \cdot 10^{\frac{NF_{\mathrm{mixer}}}{10}} + 10^{\frac{P_{\mathrm{phase}}+P_{\mathrm{j}}}{10}}}{10^3 \cdot kT \cdot B}\right) \tag{3.32}$$

where, NF_{LS} is large-signal noise figure, k is Boltzmann's constant, T is absolute temperature, B is bandwidth(1.23MHz in a CDMA system), NF_{mixer} is noise figure of mixer, P_{phase} is the integrated phase noise, and P_{j} is the jammer power. From (3.32), it can be shown that the large-signal noise figure is 22dB with -16dBm of jammer power, -75dBc of integrated phase noise, and 0dB mixer noise figure. Even with 15dB of mixer noise figure, which is increased from the original NF due to the jammer, it will affect the large-signal noise figure by 0.8dB only. The large-signal noise figure was measured and no outstanding noise figure degradation was observed. The *1/f* noise corner frequency of the mixer is approximately 50kHz. Gain is measured with a single tone input at 150kHz (IF) offset from the LO frequency, and is greater than 22dB. The measured gain and

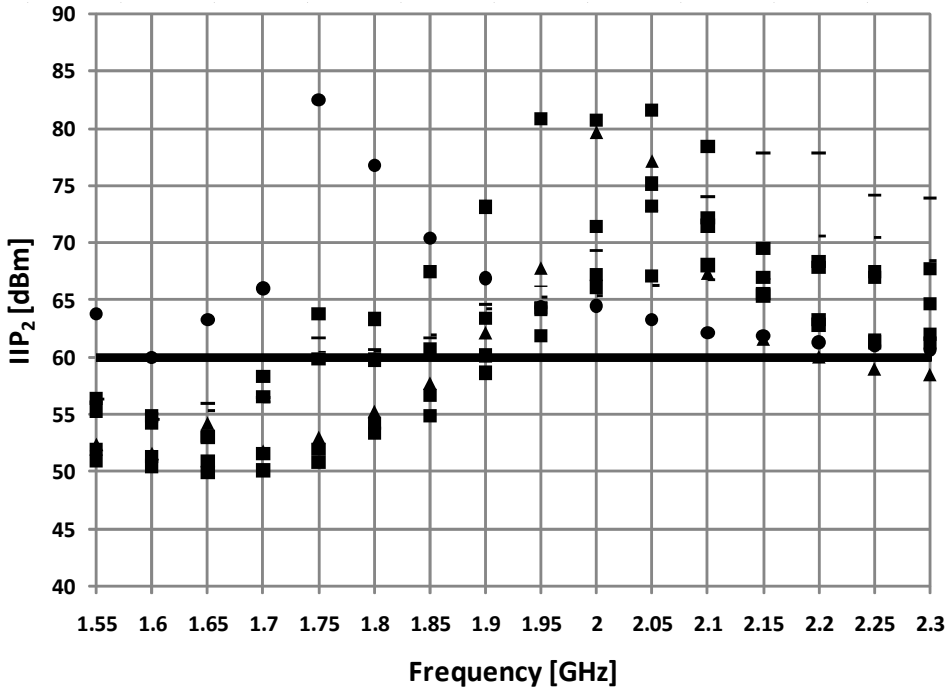

Figure 3.22: Measured un-calibrated IIP_2 performance over operation bandwidth.

NF performances are shown in Fig. 3.21 along with simulated results. The agreement between measured and simulated NF is excellent from 1.75GHz to 2.2GHz. At the low and high frequency edge, the deviation becomes larger due to the additional parasitic effects from the socket. The gain agreement between measured and simulated values are excellent.

The measured IIP_2 performance across the band is shown in Fig. 3.22. Two -30dBm input tones at 5MHz and 5.21MHz offset from the LO frequency are used. The resulting IM_2 component will be at 210kHz. The IIP_2 performance over the band(from 1.55GHz to 2.3GHz) is greater than 50dBm without calibration for more than five measured devices. Each device is presented with different markers in Fig. 3.22. The solid line presents a reference +60dBm IIP_2. As can be seen, the designed mixer shows better than +60dBm of un-calibrated IIP_2 performance for US PCS band(1.93-1.99GHz) and IMT band(2.11-2.17GHz). In an earlier paper [66], the IIP_2 performance is reported for US PCS band only. The IM_2 power with input power swept from -32dBm to -24dBm

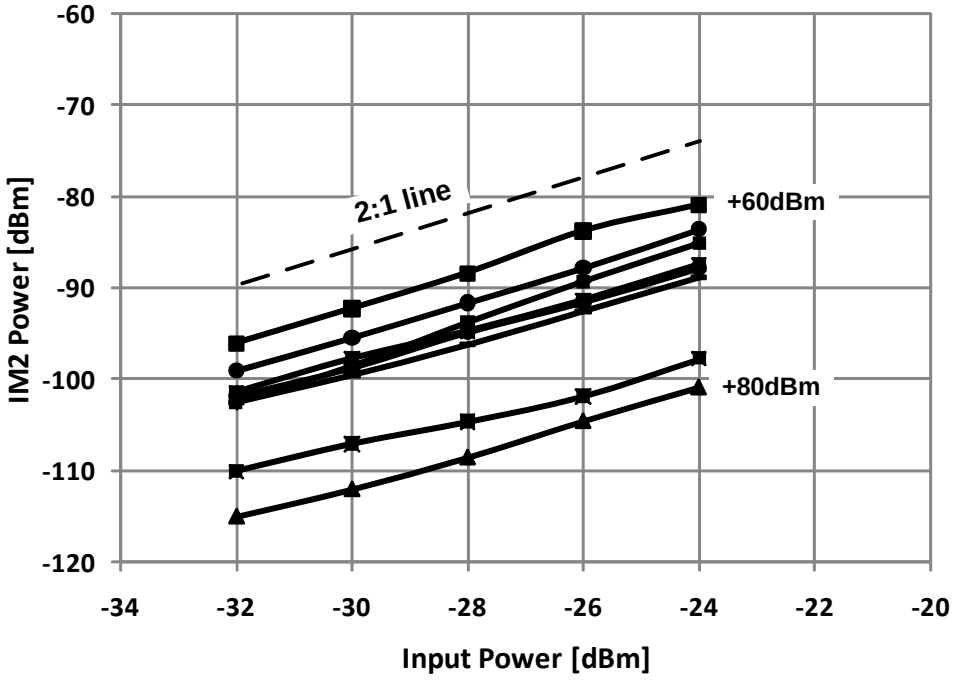

Figure 3.23: Measured IM_2 power from -32dBm to -24dBm at 2GHz.

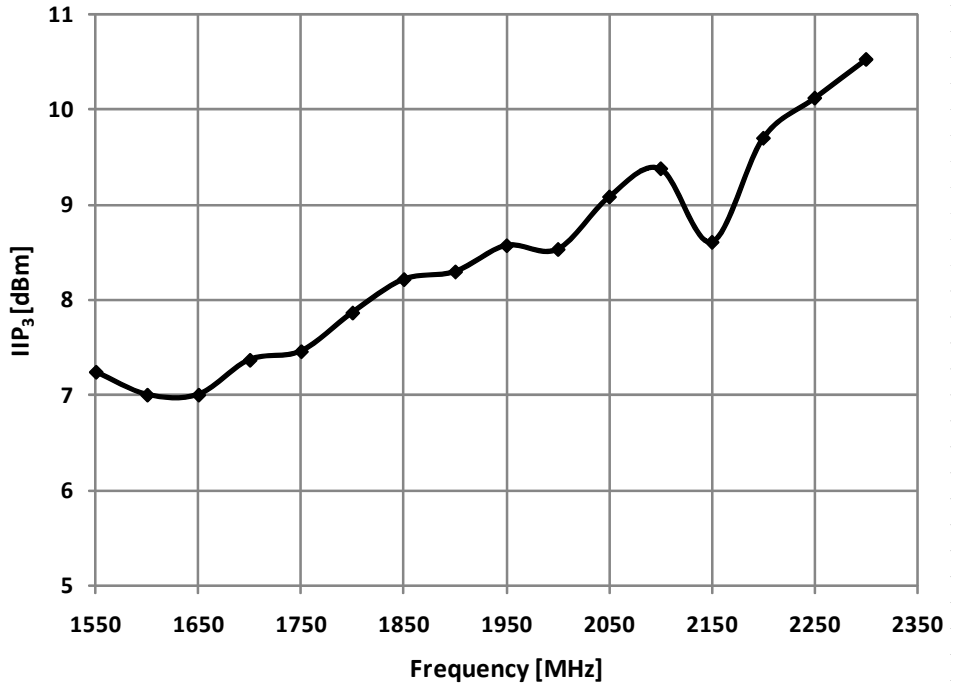

Figure 3.24: Measured IIP_3 performance over operation bandwidth.

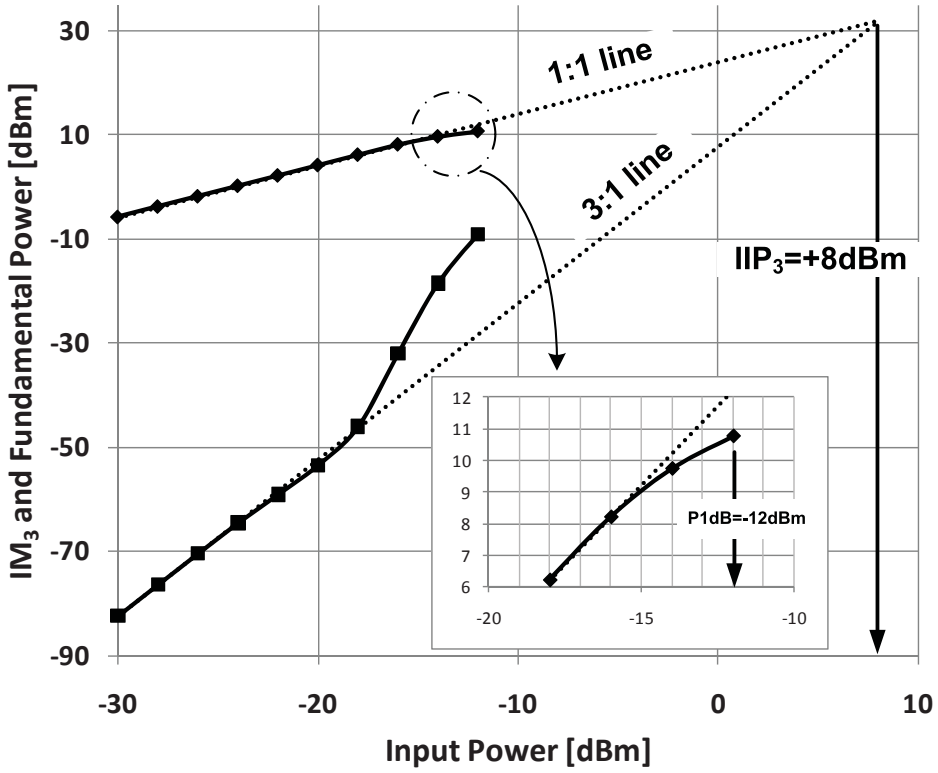

Figure 3.25: Measured $\mathrm{IM_3}$ and fundamental tone power from -30dBm to -12dBm at 2GHz.

at 2GHz LO frequency is measured, and shown in Fig. 3.23. Again, seven different devices are measured and each device is depicted with different lines in Fig. 3.23.

The $\mathrm{IIP_3}$ performance is measured and shown to be better than 7dBm over the band. Two -30dBm inputs at 1.25MHz and 2.05MHz offset from the LO frequency are used. The resulting $\mathrm{IM_3}$ component will be at 450kHz, which is in-band. The measured $\mathrm{IIP_3}$ results over the band are shown in Fig. 3.24. The $\mathrm{IM_3}$ power and P1dB performances at 2GHz are measured and shown in Fig. 3.25. The P1dB is -12dBm. The mixer starts to show heavily nonlinear behavior at -18dBm of input power.

The Residual side-band (RSB) performance, representing the I and Q channel balance, is measured, and is better than 35dB.

The performance summary for the mixer is summarized in Table 3.1. The current consumption is 5mA for both I/Q channels including the TIA stage from a 2V power

Table 3.1: Degenerated Passive Mixer Measurement Results

Performances	Measurement	Unit
Frequency	1.55-2.3	GHz
S_{11}	$\leq$ -10	dB
Gain	22.5-25	dB
Noise Figure	7.7-9.5	dB
IIP_2	$\geq 60^a$	dBm
IIP_3	≥ 7	dBm
LO leakage	$\leq$ -90	dBm
Input P1dB	-12	dBm
Power	10(mixer+TIA)	mW
Technology	0.18μm CMOS	

[a] at 2GHz, un-calibrated

supply.

3.5 Conclusion

An improved resistively degenerated wide-bandwidth (1.55GHz-2.2GHz) passive downconverter is introduced and analyzed. The circuit includes an input transconductance stage, a resistively degenerated passive mixer, and a TIA.

The complementary input g_{m} boosting method is used in addition to cross-coupled inputs to increase the effective g_{m}. A degeneration resistance is added to a conventional passive mixer, and we demonstrate that this leads to improved NF and IIP_2 performance. The analytical results show good agreement with simulated results, and design guidelines are proposed for minimizing noise and distortion in the circuit. Thanks to the proposed architecture, the fabricated passive mixer shows a low noise figure of less than 9.5dB with more than +50dBm of un-calibrated IIP_2 performance. This chapter has been published in part in the following publications:

1. N. Kim, V. Aparin, and L. E. Larson, "A resistively degenerated wide-band passive mixer with low noise figure and +60dBm IIP_2 in 0.18μm CMOS," *Proc. IEEE RF Integrated Circuits Symp., RFIC*, 2008, pp. 185-188.

2. N. Kim, V. Aparin, and L. E. Larson, "A resistvely degenerated wideband passive

mixer with low noise figure and high IIP_2," *IEEE Trans. Microw. Theory Tech.*, vol. 58, no. 4, pp. 820-830, Apr. 2010

Chapter 4

SAW-less Receiver with Highly Linear Embedded Filtering Passive Mixer

To avoid TB and Tx IM_2 issues in a SAW-less receiver, the leaked Tx signal should be rejected before the mixer, as it is explained in chapter 1. As introduced in chapter 1, there are some non-SAW methods of rejecting the Tx signal. But practical issues prevent these methods from being used widely. A new Tx rejection method, known as an embedded filtering passive (EFP) mixer, is introduced in this chapter, which requires no additional inductance nor active circuits. Though this method provides Tx rejection, it still requires a highly linear LNA due to the TB performance specification.

In a SAW-less receiver, the mixer becomes the critical component in terms of the linearity performance of the receiver. Both sensitivity and STD performance can be degraded if the linearity performance of the mixer is poor. In addition, the phase noise requirement of the VCO at the jammer offset becomes more stringent. Therefore, the overall area and power consumption of the receiver has to be increased due to the VCO phase noise requirement.

The flicker noise (1/f) of the mixer can corrupt the integrated noise, but the passive mixer will not introduce significant flicker noise, since there is no dc current [54]. A current output passive mixer has well-known transimpedance amplifier (TIA) noise amplification issues [58]. The noise amplification problem can be overcome by increasing the output impedance of the mixer. The mixer output impedance seen by the TIA is dominated by the switched-capacitor resistance, operating at LO frequency. The

switched-capacitor resistance is inversely proportional to the operating frequency and the switched-capacitor value. A large portion of the capacitance is from the LNA output stage. Therefore, the mixer output impedance can be increased if the capacitance associated with LNA output can be removed. The method described in chapter 3 is useful when a non-inductive load is used at the LNA output. In chapter 3, a degeneration resistance is used to effectively reduce the parasitic capacitance. But the parasitic capacitance associated with the LNA output can also be tuned out in an inductive load LNA, due to LC resonance. Therefore, the noise amplification issue will not be significant, if the LNA uses an inductive load.

The low impedance of the mixer input ensures that the RF current flows to the mixer input with minimal loss. Hence, there will be almost no voltage signal swing at the LNA output due to the low impedance provided by the mixer. The nonlinearity of the mixer plays a role after the Tx signal is down-converted.

4.1 Problem of Conventional CMOS Passive Mixer + TIA Design

One of the problems of using a conventional passive mixer with a TIA at the output is illustrated in Fig. 4.2. At a relatively high downconverted IF frequency (like Tx signal), the finite OTA gain-bandwidth causes a large signal swing at the TIA input, which introduces nonlinearity from both the mixer and the TIA.

In addition, the finite OTA gain-bandwidth and non-zero output impedance creates out-of-band gain peaking, as explained in chapter 3. This out-of-band peaking reduces the Tx filtering and causes additional TB contribution from TIA stage in a SAW-less receiver. These issues will be worse if the parasitic input capacitance of the OTA is large, but the input capacitance cannot be easily reduced in narrow-band communication systems, due to the flicker noise issue. The non-ideal transimpedance function are derived in chapter 3 and are given in Equation (3.31). The input impedance of the TIA

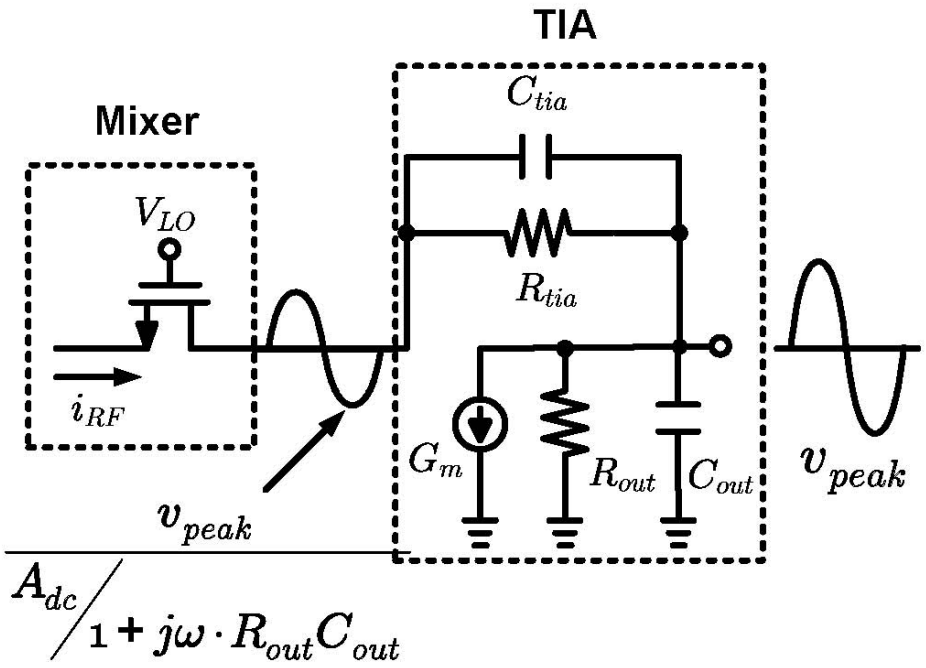

Figure 4.1: TIA non-ideal input impedance issue.

can be given as

$$Z_{\mathrm{in,TIA}}(j\omega) = \frac{Z_{\mathrm{out}}(j\omega) + Z_{\mathrm{f}}(j\omega)}{j\omega \cdot C_{\mathrm{gs}} \cdot [Z_{\mathrm{out}}(j\omega) + Z_{\mathrm{f}}(j\omega)] + A(j\omega) + 1} \tag{4.1}$$

The non-ideal transimpedance effect and non-ideal input impedance focused at Tx offset are illustrated in Fig. 4.2. The out-of-band peaking nearly doubles the voltage swing at the TIA output, and the input impedance at 45MHz is more than double its low frequency value. Even if the OTA has a high gain-bandwidth product, it has to provide tremendous current into the feedback capacitor to avoid introducing nonlinearity caused by incomplete capacitor charging, if no Tx rejection prior to the TIA is provided.

4.2 Embedded Filtering Passive Mixer

To avoid the issues due to the non-ideal effects of the OTA, the high-frequency Tx signal should be rejected before it reaches the TIA. The simplified schematic of the

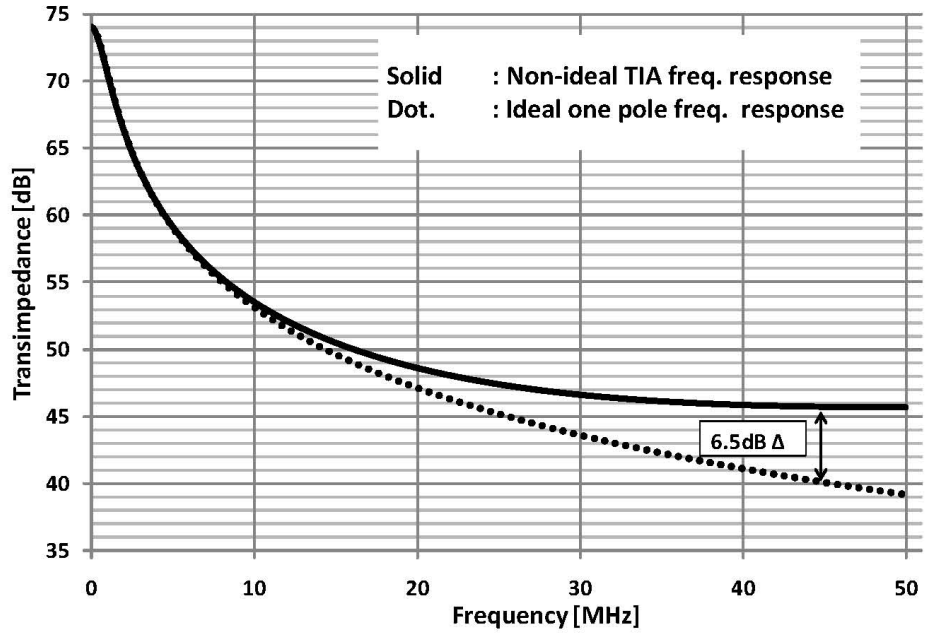

(a) Non-ideal transfer function

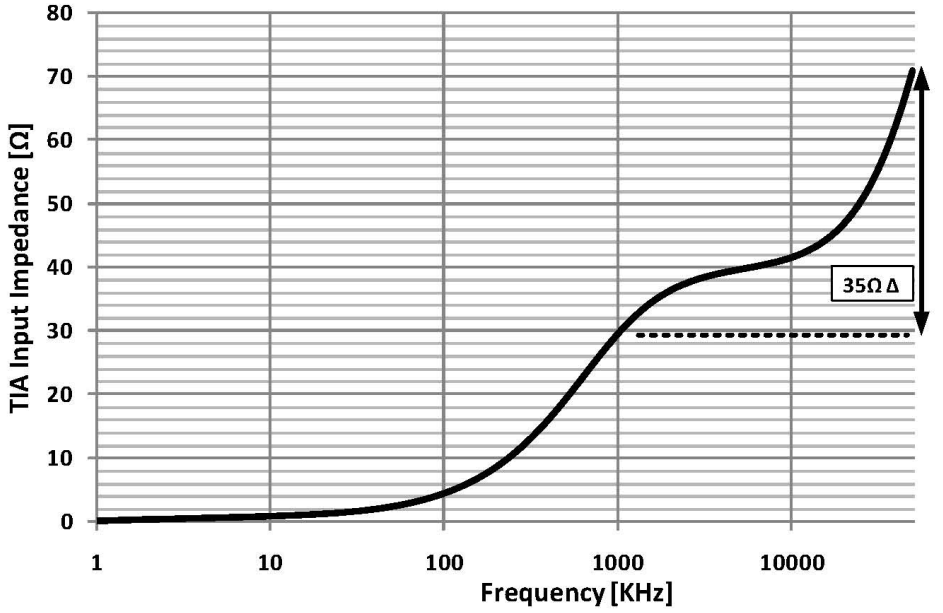

(b) TIA input impedance

Figure 4.2: Calculated TIA non-ideal effects. (a) Non-ideal transfer function. (b) Non-idel input impedance.

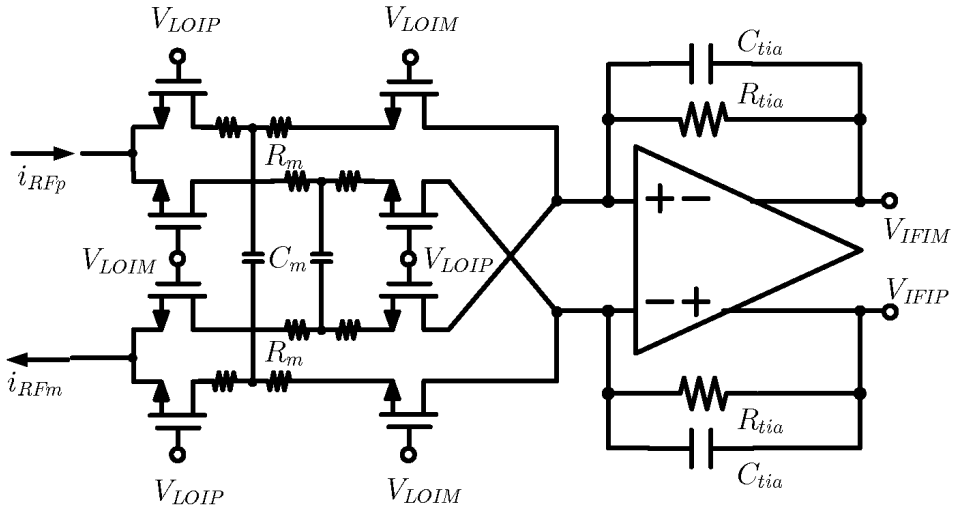

Figure 4.3: Simplified schematic of the proposed EFP mixer.

embedded filtering passive mixer (EFP mixer), which avoids these problems, is shown in Fig. 4.3. The EFP mixer has two switches connected in series, and each switch is controlled by opposite phases of the local oscillator (LO) signal. In between the switches is an RC filter, which determines the bandwidth of the filtering. It is a simple current filter circuit, as shown in Fig. 4.4, if the frequency conversion operation is removed. The RF current $(i_{\mathrm{RF}}(t))$ from the LNA flows into the first set of switches, which performs frequency conversion with $\phi_1(t)$, and the down-converted current will go into C_{m}. This current can be described by

$$\begin{aligned} i_{\mathrm{C_m}}(t) &\approx G_{\mathrm{m,LNA}} \cdot A_{\mathrm{rf}} \cdot \cos(\omega_{\mathrm{rf}} t) \cdot \phi_1(t) \\ &= G_{\mathrm{m,LNA}} \cdot A_{\mathrm{rf}} \cdot \cos(\omega_{\mathrm{rf}} t) \\ &\times \left[\frac{1}{2} + \sum_{n=0}^{\infty} \frac{2}{\pi} \cdot \left[\frac{(-1)^n}{2n+1} \cos\left((2n+1) \cdot \omega_{\mathrm{LO}} \cdot t\right) \right] \right] \end{aligned} \tag{4.2}$$

where $G_{\mathrm{m,LNA}}$ is the effective transconductance of the LNA, A_{rf} is the voltage amplitude of the input signal at the LNA input, ω_{rf} is the RF input frequency, and ω_{LO} is the local oscillation frequency. The resistor to the left of C_{m} is used for balancing purposes between positive and negative signal paths. As explained in chapter 3, this resistor will help to reduce the mismatches between two paths, improving IIP_2. Since the voltage on the capacitor is the integration of the current, the voltage on C_{m} due to $i_{\mathrm{C_m}}(t)$ can be

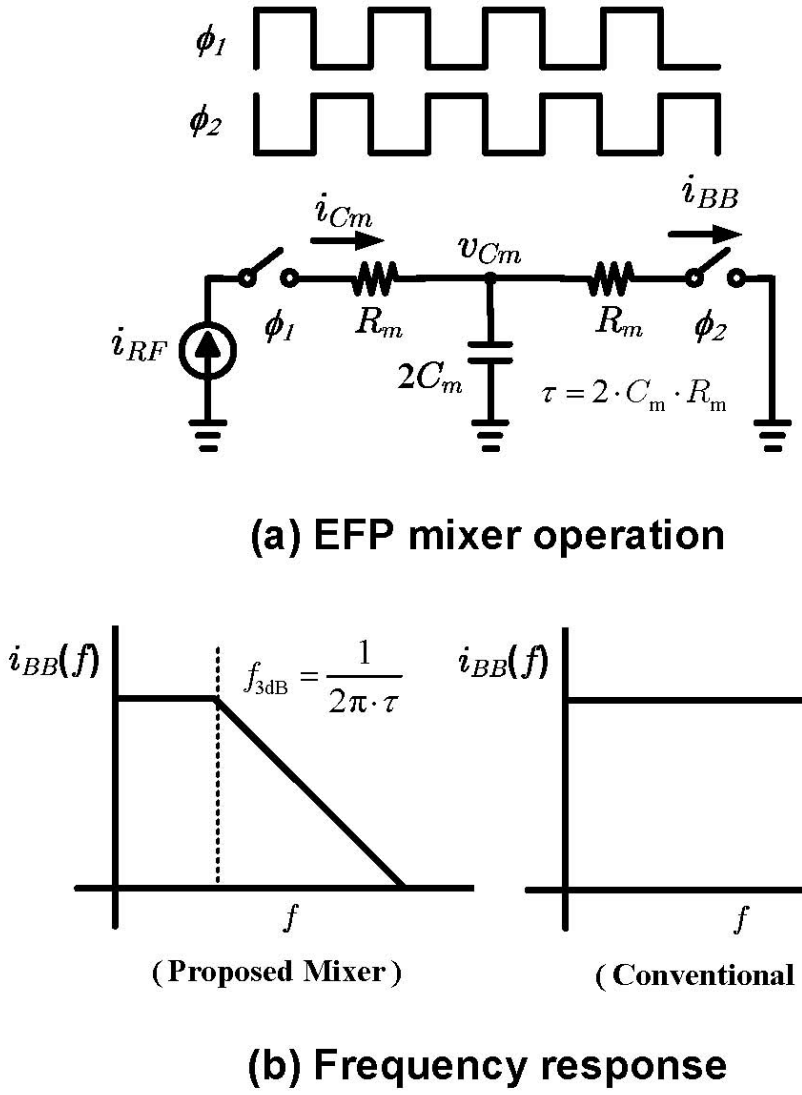

Figure 4.4: Theory of the EFP mixer. (a) Conceptual operation. (b) Frequency response.

described by

$$
\begin{aligned}
&v_{\mathrm{C_m}}(t) \\
&= \frac{G_{\mathrm{m,LNA}} \cdot A_{\mathrm{rf}}}{C_{\mathrm{m}}} \cdot \int \cos\left(\omega_{\mathrm{rf}} t\right) \cdot \left[\frac{1}{2} + \sum_{n=0}^{\infty} \frac{2}{\pi} \cdot \left[\frac{(-1)^n}{2n+1} \cos\left((2n+1) \cdot \omega_{\mathrm{LO}} \cdot t\right)\right]\right] dt \\
&= \frac{G_{\mathrm{m,LNA}} \cdot A_{\mathrm{rf}}}{C_{\mathrm{m}}} \cdot \left[\frac{\sin\left(\omega_{\mathrm{rf}} t\right)}{2\omega_{\mathrm{rf}}} + \sum_{n=0}^{\infty} \frac{1}{\pi} \cdot \frac{(-1)^n}{2n+1} \cdot \left[\frac{\sin\left(\left[(2n+1) \cdot \omega_{\mathrm{LO}} - \omega_{\mathrm{rf}}\right] \cdot t\right)}{\left[(2n+1) \cdot \omega_{\mathrm{LO}} - \omega_{\mathrm{rf}}\right]}\right.\right. \\
&\left.\left. + \frac{\sin\left(\left[(2n+1) \cdot \omega_{\mathrm{LO}} + \omega_{\mathrm{rf}}\right] \cdot t\right)}{\left[(2n+1) \cdot \omega_{\mathrm{LO}} + \omega_{\mathrm{rf}}\right]}\right]\right]
\end{aligned} \tag{4.3}
$$

Note that the terms with n>0 will have large amplitude reduction due to integration and so (4.3) can be approximated by

$$
\begin{aligned}
&v_{\mathrm{C_m}}(t) \\
&\approx \frac{G_{\mathrm{m,LNA}} \cdot A_{\mathrm{rf}}}{C_{\mathrm{m}}} \cdot \left[\frac{\sin\left(\omega_{\mathrm{rf}} t\right)}{2\omega_{\mathrm{rf}}} + \frac{1}{\pi} \cdot \left[\frac{\sin\left(\left[\omega_{\mathrm{LO}} - \omega_{\mathrm{rf}}\right] \cdot t\right)}{\omega_{\mathrm{LO}} - \omega_{\mathrm{rf}}} + \frac{\sin\left(\left[\omega_{\mathrm{LO}} + \omega_{\mathrm{rf}}\right] \cdot t\right)}{\omega_{\mathrm{LO}} + \omega_{\mathrm{rf}}}\right]\right]
\end{aligned} \tag{4.4}
$$

In the next LO phase, when $\phi_2(t)$ is high, C_{m} discharges into the TIA with a time constant of $\tau = 2C_{\mathrm{m}} \cdot R_{\mathrm{m}}$, in a similar manner to the SCR-DAC [73]. The EFP mixer operation is shown in Fig. 4.5, with the example of a 1GHz f_{LO}, 900MHz f_{RF}, and the resulting 100MHz baseband signal. As can be seen, the output current of the EFP mixer is similar to a Return-to-Zero Sample-and-Hold (RZ S/H) [74], except an exponential decay occurs when ϕ_2 is high. This can be modeled by modifying the sampling pulse to

$$
h\left(t\right) = e^{-t/\tau} \cdot \sum_{n=-\infty}^{\infty} \left[\mathrm{u}\left(t - nT_{\mathrm{LO}}\right) - \mathrm{u}\left(t - (n+1/2) \cdot T_{\mathrm{LO}}\right)\right] \tag{4.5}
$$

The Laplace transform of (4.5) is

$$
H\left(s\right) = \frac{1 - e^{-(s+1/\tau)\frac{T_{\mathrm{LO}}}{2}}}{s + 1/\tau} \tag{4.6}
$$

which adds an additional low-pass term to the mixer transfer function. This sampling pulse is convolved in the time domain with the sampled baseband signal on C_{m} during ϕ_1 from (4.4), so the complete transfer function at the mixer output, from RF input

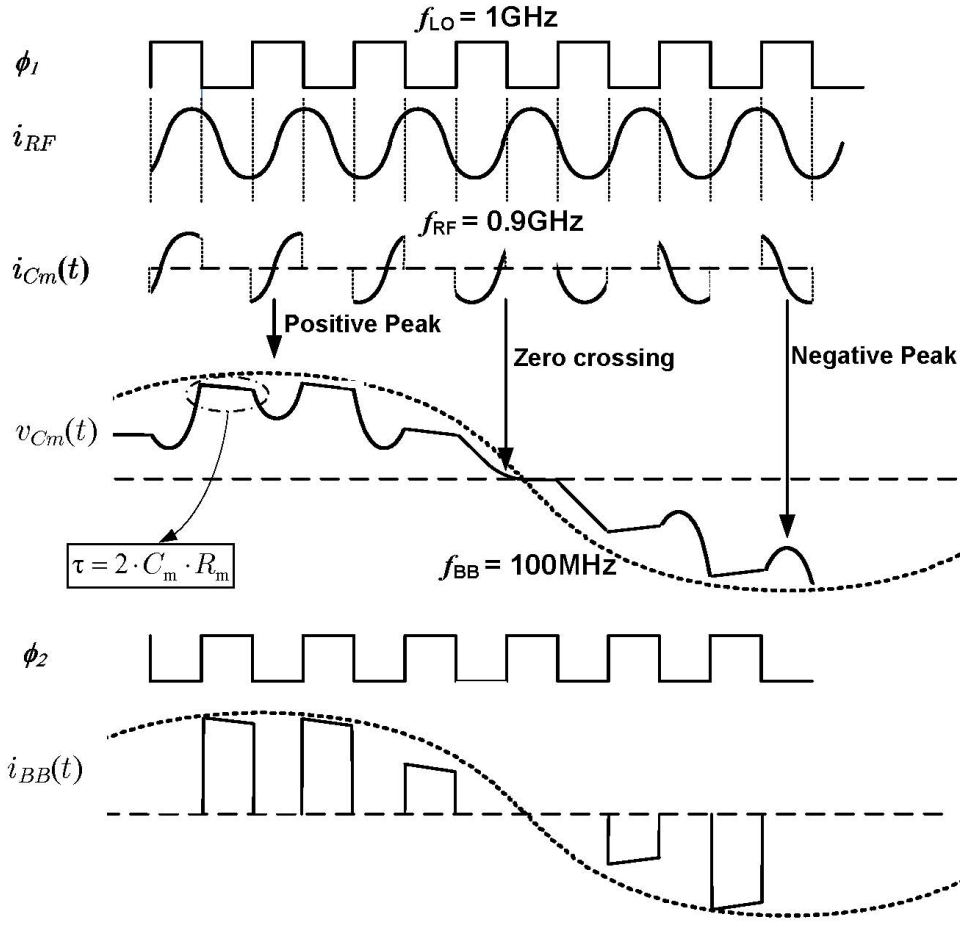

Figure 4.5: Illustration of EFP mixer operation.

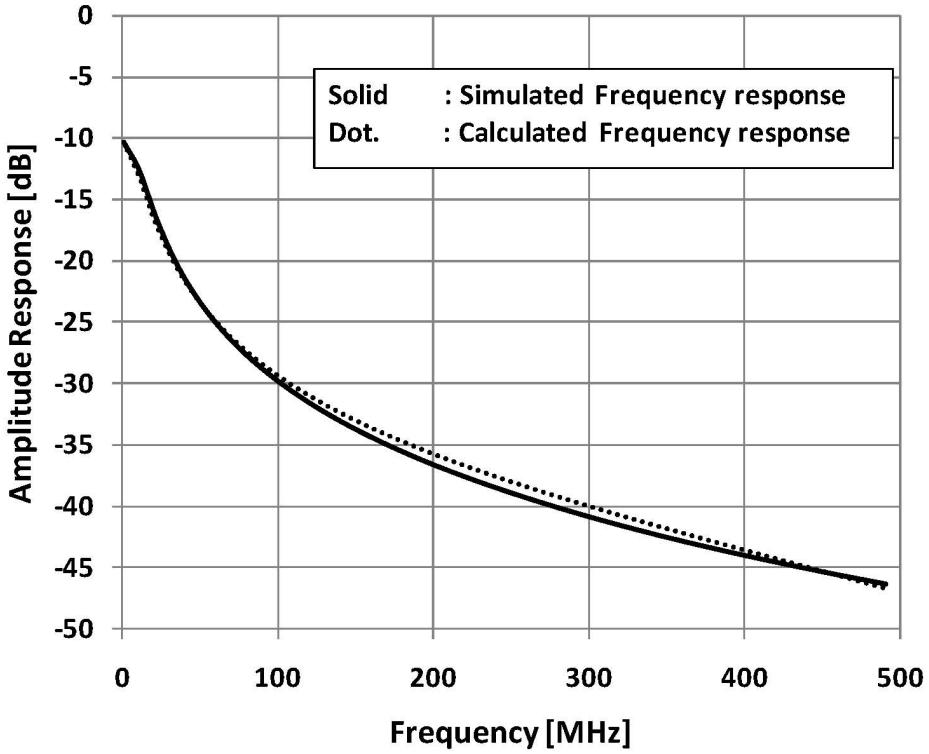

Figure 4.6: Calculated and simulated EFP mixer frequency response.

voltage to baseband current output, is approximately

$$|H_{\mathrm{EFP}}(s)| \approx \left| \frac{1 - e^{-(s+1/\tau)\frac{T_{\mathrm{LO}}}{2}}}{\left(s + 1/\tau\right)^2} \right| \cdot \frac{G_{\mathrm{m,LNA}}}{\pi \cdot C_{\mathrm{m}}} \cdot \frac{1}{R_{\mathrm{m}}} \cdot \frac{2}{T_{\mathrm{LO}}} \tag{4.7}$$

The calculated frequency amplitude response of (4.7) and simulated response of the mixer are both shown in Fig. 4.6, and the agreement is excellent.

4.3 SAW-less Receiver Design

The block diagram of the complete receiver is shown in Fig. 4.7. The receiver consists of an LNA, EFP mixer, TIA, LO input buffer, LO divider, and mixer LO buffer. The detail schematics for LNA and mixer are shown in Fig. 4.8. As explained in chapter 2, the LNA has two operation modes, low-linearity and high-linearity. The difference

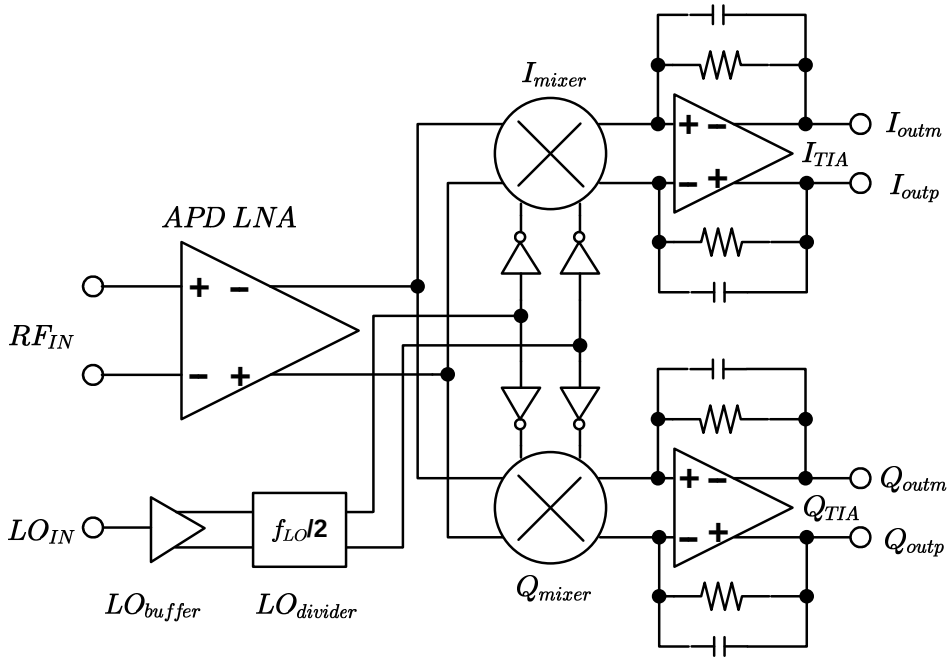

Figure 4.7: Block diagram of the designed receiver.

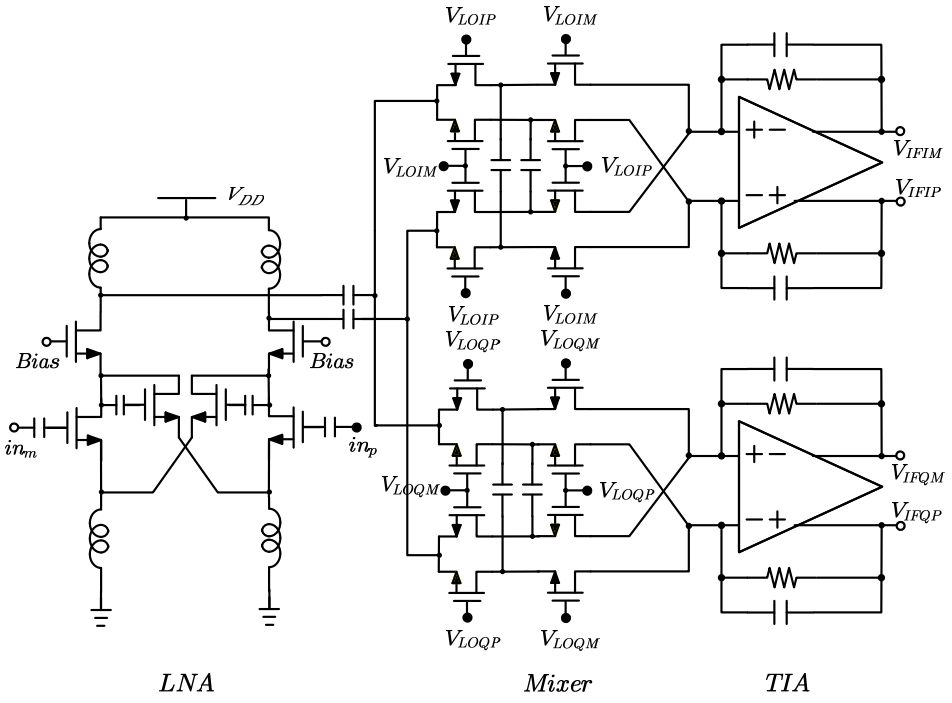

Figure 4.8: Detail schematics for LNA and mixer.

of the noise performance between the two modes is 0.1dB. But the effective transconductance is different by 2.9dB. This could cause a significant NF difference in the entire receiver chain. The LNA is designed to have 1.5dB NF in the low-linearity mode at 880MHz. The overall receiver NF difference between the two modes can be calculated with 1.5dB of LNA noise, since the noise from the mixer is the same in both modes.

$$NF_{\mathrm{HL-LL}} = \frac{\overline{i^2_{\mathrm{nsLL,o}}} + \frac{\overline{i^2_{\mathrm{ndLL,o}}}\cdot 10^{-2.9/10} + \frac{g_{\mathrm{m,3}}}{g_{\mathrm{m,1}}}\cdot\overline{i^2_{\mathrm{ndLL,o}}}\cdot 10^{-2.9/10} + \overline{i^2_{\mathrm{nm,o}}}}{10^{-2.9/10}}}{\overline{i^2_{\mathrm{nsLL,o}}} + \overline{i^2_{\mathrm{ndLL,o}}} + \overline{i^2_{\mathrm{nm,o}}}} \tag{4.8}$$

where $NF_{\mathrm{HL-LL}}$ is the receiver noise difference (in dB) between the two modes, $\overline{i^2_{\mathrm{nm,o}}}$ is the mixer output noise, and the second term in the bracket represents the additional noise due to the LNA $g_{\mathrm{m,3}}$ canceller. Equation (4.8) applies to both conventional and EFP mixer receiver cases. The calculated NF difference, with an 8-to-1 transconductance ratio between the main and auxiliary path, is 0.6dB. The simulated frequency responses of the conventional and EFP mixer receiver at the TIA output are shown in Fig. 4.9. The response is normalized to show the rejection difference. Note the 10dB improved rejection of the Tx leakage signal.

4.4 SAW-less Receiver Measured Results

A die photograph of the receiver is shown in Fig. 4.10. It is fabricated in a 0.18μm 5-metal 1-poly Si CMOS process. It includes electrostatic discharge (ESD) for input and output pins, pads, and supply clamps. The total area including ESD, pads, and supply clamps is 2.25mm^2. As can be seen from Fig. 4.10, the active circuit area is less than 1.4mm^2. For comparison purpose, two receivers are fabricated, one using the suggested new approach and the other using the conventional mixer approach.

The measured frequency response for both receivers with the differing mixers is shown in Fig. 4.11. The measured gain performances are 42/44dB for EFP mixer and 44/46dB for conventional mixer in the low-linearity/high-linearity modes, respectively.

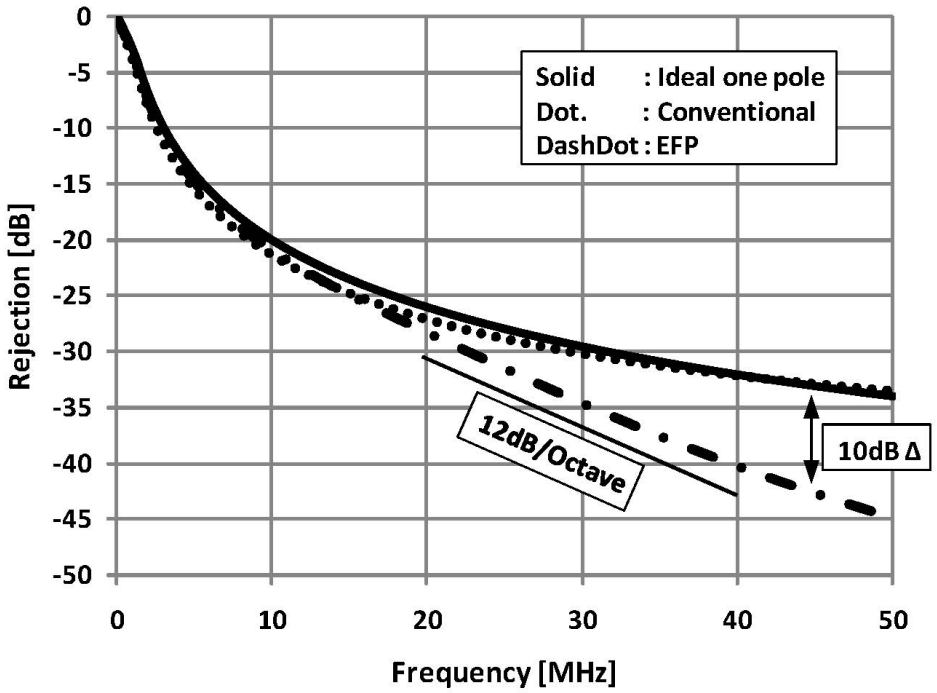

Figure 4.9: Simulated frequency responses of the conventional and proposed receiver.

The frequency response is normalized, since there is 2dB of gain difference. The TIA provides 1.5MHz of 3dB cutoff frequency and the EFP mixer is designed to have an additional pole at 10MHz. As can be seen, the proposed receiver has 15dB more Tx rejection at 45MHz compared to the conventional receiver. The graph contains an ideal single-pole ($f_{3\mathrm{dB}}$=1.5MHz) frequency response for comparison purpose. The difference between the ideal single-pole response and the measured result of the EFP mixer is 9dB. The conventional receiver shows 6dB worse response than the single-pole response due to the TIA non-ideal effect, which was not included in the simulation.

The measured TB performance of the proposed receiver is shown in Fig. 4.12. Two Tx tones, with -31dBm each at 45MHz offset, and a jammer at 1MHz offset with -30dBm of power are applied. With the high-linearity mode ON, the XMOD tone is at -65.8dBm, which implies 77.8dB of TB performance. With the APD cancellation path OFF, and where the Tx tone and jammer tone are backed-off by 2dB to accommodate the gain difference, the TB is 65.3dB. This difference between two modes implies two important facts. First, the APD method improves the TB by 12.5dB. Second, the

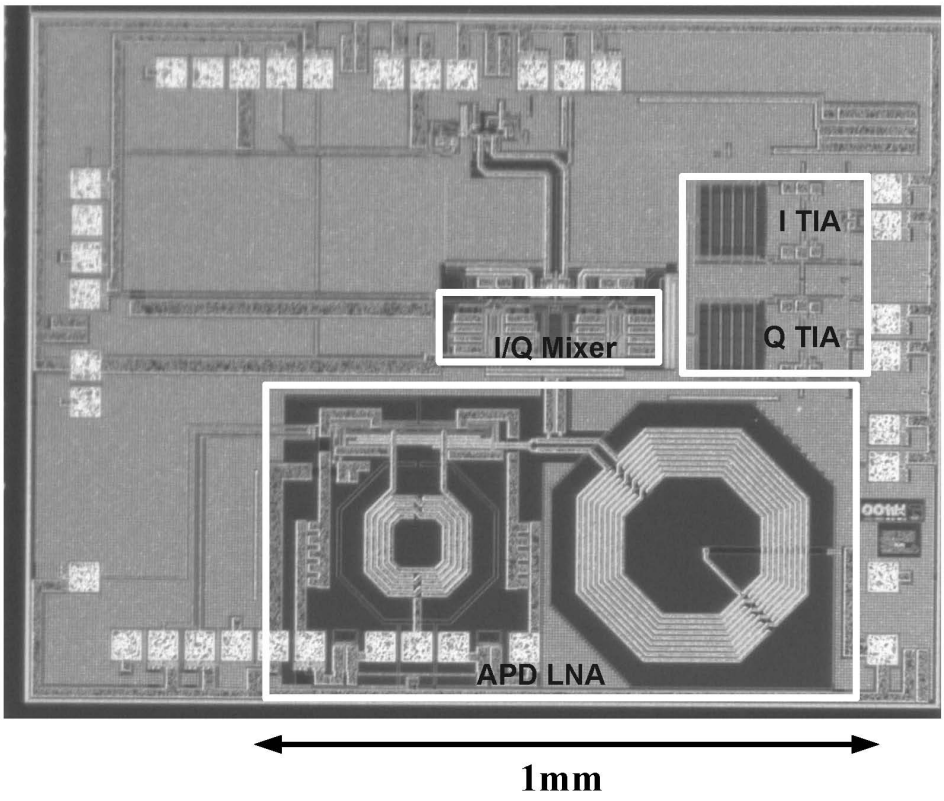

Figure 4.10: Die photograph of designed SAW-less receiver.

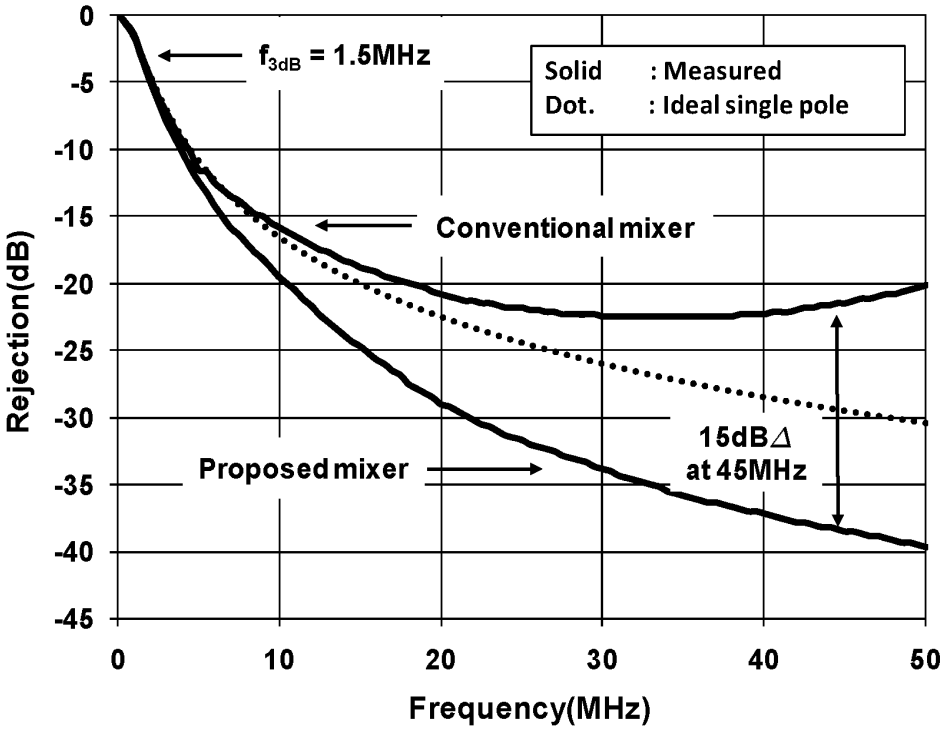

Figure 4.11: Measured frequency responses of the conventional and proposed receiver.

TB variation between two modes means that the mixer does not contribute any significant TB. Therefore, the additional rejection provided by the EFP mixer dramatically improves system linearity performance. The conventional receiver does not have TB variation between two modes, since its TB is limited by the mixer and TIA.

The average LNA input referred IIP_2 performance (measured over several devices) with the EFP mixer is +60dBm and +50dBm for the conventional double-balanced passive mixer. The measured IM_2 curve, with the input power sweeping at the Tx offset frequency, is shown in Fig. 4.13. The conventional receiver starts showing a 4-to-1 nonlinearity, which is strongly nonlinear behavior, beyond -30dBm input power. In contrast, the proposed EFP mixer starts showing strongly nonlinear behavior above -24dBm of input power. The conventional receiver has +48dBm of IIP_2 performance at -30dBm.

The overall performance comparison is shown in Table Table 4.1. Each receiver is measured in both modes, low-linearity and high-linearity, by turning the APD path

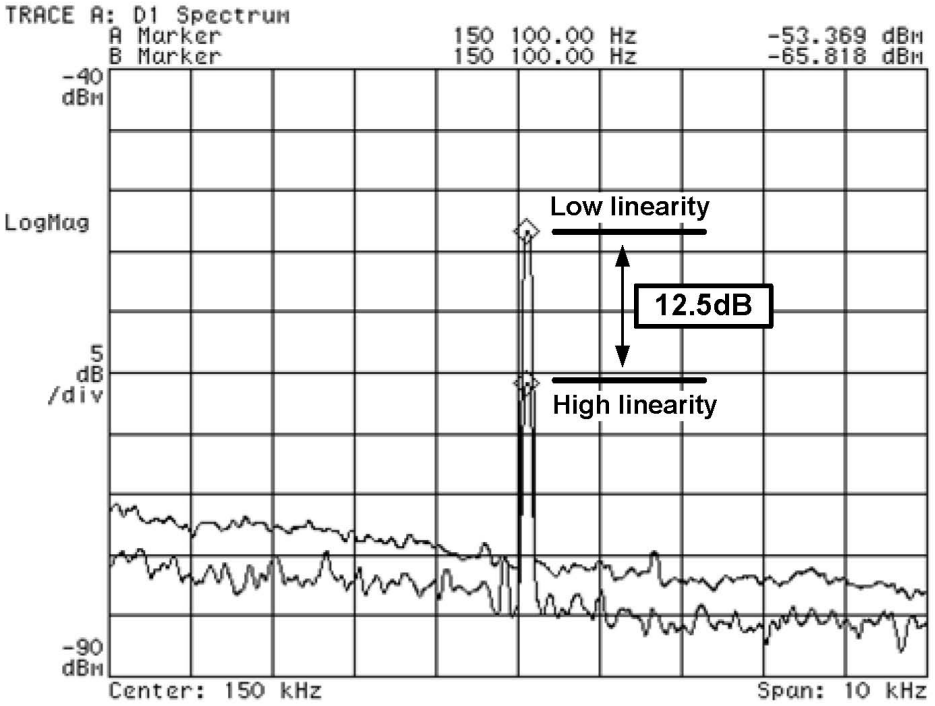

Figure 4.12: Measured XMD tone with/without cancellation path.

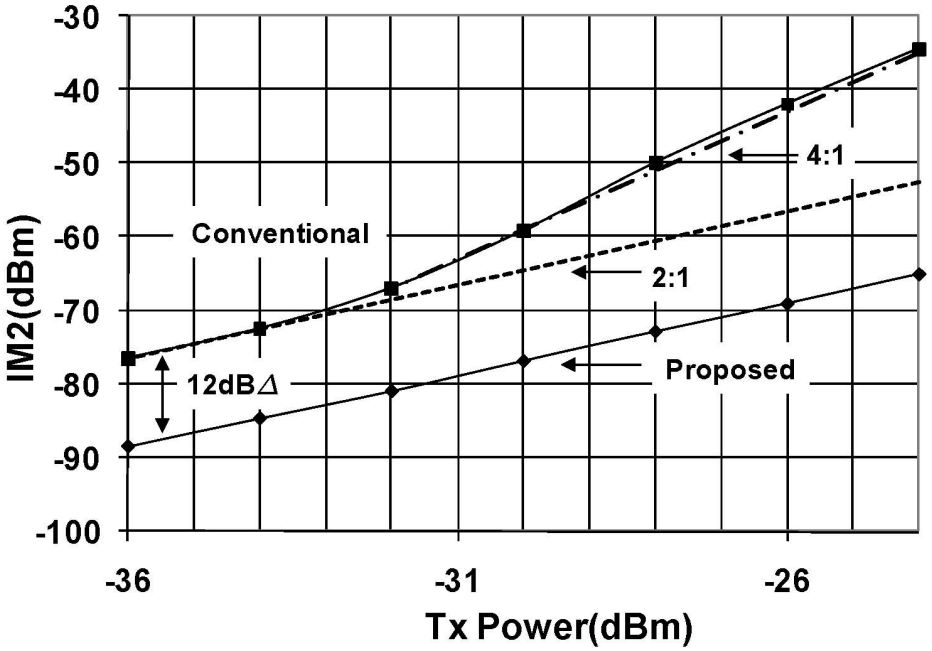

Figure 4.13: Measured IM_2 level with various input power for the conventional and proposed receiver.

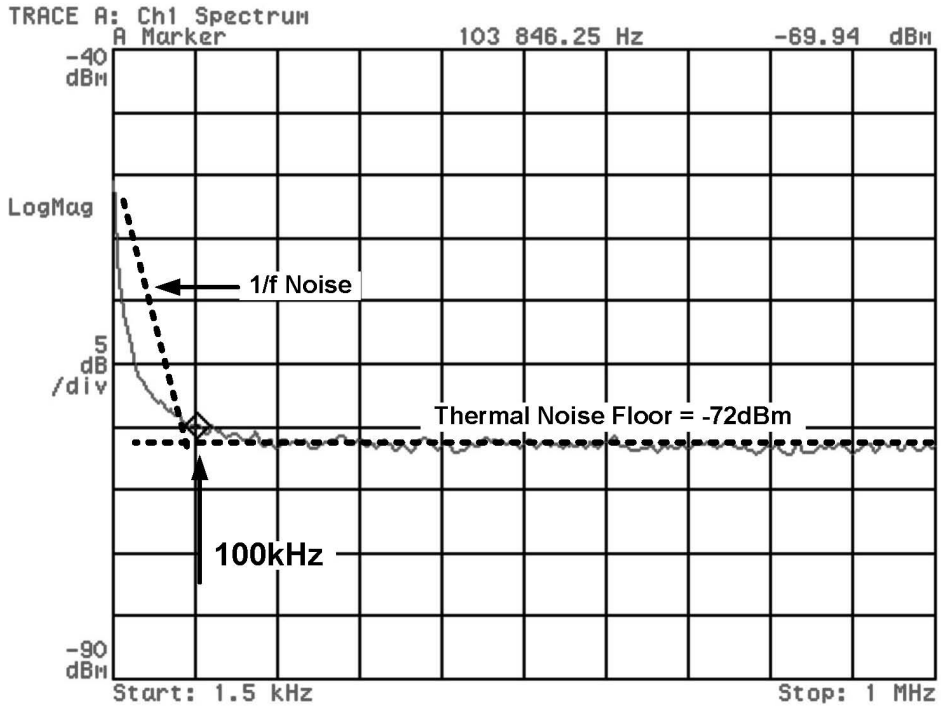

Figure 4.14: Measured 1/f noise corner.

ON/OFF. As explained in chapter 1, the Tx IIP_2 performance is important for the sensitivity performance in a SAW-less receiver system, while the TB performance is important for the STD test. Even though the NF performance is worse by 0.8dB to 1dB in the high-linearity mode, it does not degrade the STD performance excessively. The calculated NF degradation in the high-linearity mode was 0.6dB, but measured results show 0.8dB degradation in a conventional receiver and 1dB in the proposed receiver, respectively. This small difference is expected, since the calculation did not account for gate-induced noise and the resulting correlation noise change between the two modes. The proposed receiver has lower gain and higher NF than a conventional one, due to additional loss in the second set of switches. The measured noise power level at baseband is shown in Fig. 4.14. The 1/f noise corner is less than 100kHz thanks to the passive mixer architecture and wide size of the input FET in the TIA.

The total power consumption for the signal path is 18mA, 14mA for the APD LNA and 4mA for the I/Q TIAs. The mixers do not consume any power since they are

Table 4.1: SAW-less Receiver Measurement Results

Performances	Proposed Rx	Conventional Rx	Unit
Vdd	2.1	2.1	V
Idd	17/18[a]	17/18	mA
Frequency	894	894	MHz
VSWR	$\leq$ 2:1	$\leq$ 2:1	
Gain	44/42	46/44	dB
Noise Figure[b]	2.4/3.4	2.0/2.8	dB
IIP_2(at 45MHz)	+60/+65	+50/+55	dBm
Triple Beat	+65.3/+77.8	+47/+47	dB
Tx Rejection	37	22	dB

[a]Low-linearity/High-linearity
[b]Integrated over CDMA BW, DSB NF

passive.

4.5 Conclusion

A highly linear SAW-less receiver is introduced. The high IIP_2 of the receiver at the Tx offset is essential to avoid corrupting the system's sensitivity performance, and a high TB is required to avoid STD performance degradation due to transmitter leakage. A new passive mixer architecture, the embedded filtering passive (EFP) mixer, is introduced and analyzed. The performance comparisons between the two receivers, a receiver employing a conventional passive mixer and a receiver employing the EFP mixer, are examined. Thanks to the EFP mixer and the APD method in the LNA, the highly linear performance is achieved with low noise figure and power consumption. This chapter has been published in part in the following publications:

1. N. Kim, V. Aparin, and L. E. Larson, "A highly linear SAW-less CMOS receiver using a mixer with embedded Tx filtering for CDMA," *IEEE Custom Integrated Circuits Conf.*, CICC, 2008, pp. 729-732.

2. N. Kim, V. Aparin, and L. E. Larson, "A highly linear SAW-less CMOS receiver using a mixer with embedded Tx filtering for CDMA," *IEEE J. Solid-State Circuits*, vol. 44, no. 8, pp. 2126-2137, Aug. 2009

Chapter 5

Conclusion

To save overall manufacturing cost in modern handsets, removing the inter-stage SAW filter is inevitable. However, the leaked Tx signal in FDD system prevent SAW-less receivers from being widely used. This dissertation focuses on building a highly linear SAW-less receiver.

The system requirement without SAW filter is analyzed in terms of *Sensitivity* and *Single-Tone Desensitization*(STD) performances. The effect of the Tx IM_2 on the sensitivity is critical in a SAW-less receiver and the LNA input referred system IIP_2 has to be 20dB better (+55dBm) than the conventional zero-IF receiver. The receiver TB performance, which affects STD performance directly, has to be as same as the LNA only TB performance in the conventional zero-IF receiver.

To meet the SAW-less receiver system requirement, a highly linear LNA is required. Due to the standard requirement of high/low side jammer injection, the asymmetry IM_3 performance of LNA is analyzed and the root cause is explained. By employing Active-Post Distortion (APD) method, the designed LNA is linearized to meet required TB performance. Furthermore, the source cross-couple is introduced to improve the asymmetric IM_3 performance at the Tx offset. The detail analysis of noise figure, input impedance, and transconductance in both high-linearity and low-linearity mode are given.

Even if an LNA has good TB performance, the mixer and TIA can corrupt the TB performance as well as IIP_2 performance due to the amplified Tx signal through LNA. Passive mixers exhibit better linearity performance compared to active mixers.

Table 5.1: Compliance table for target vs measured performance

Performances	Proposed Rx	Target	Unit
Vdd	2.1	2.1	V
Idd	17/18[a]	N/A	mA
Frequency	US CELL band	US CELL band	
VSWR	$\leq$2:1	$\leq$2:1	
Gain	44/42	N/A	dB
Noise Figure[b]	2.4/3.4	2.0/3.0	dB
IIP_2(at 45MHz)	+60/+65	+55	dBm
Triple Beat	+77.8	+72	dB
Tx Rejection	37	N/A	dB

[a]Low-linearity/High-linearity
[b]Integrated over CDMA BW, DSB NF

But the inherent noise penalty is problem to use a passive mixer in narrow-band application. A resistvely degenerated passive mixer is introduced to overcome the noise penalty in conventional passive mixer. The output impedance of a passive mixer can be greatly improved by degeneration and the IIP_2 performance as well. The degenerated passive mixer with TIA shows better than +60dBm of un-calibrated IIP_2 performance and +7dBm of IIP_3 performance with 10mW of power consumption from 2V supply. The gain is higher than 22dB and the noise figure is lower than 9.5dB. A +60dBm of mixer IIP_2 is good performance but it gives only +45dBm LNA input referred IIP_2 performance, when the LNA gain is +15dB.

A new embedded filtering passive (EFP) mixer is introduced to overcome the limited IIP_2 and TB performance. The designed EFP mixer is based on the degenerated passive mixer, so that the benefits of degeneration penetrate into EFP mixer. Moreover, the embedded filtering characteristic provides addtional Tx rejection and improves the overall receiver linearity performances. A SAW-less receiver is manufactured with a highly linear cross-coupled APD LNA and EFP mixers for I/Q paths. The measured performances show better than +60dBm LNA input referred IIP_2 and +77dB of TB, while consuming only 17/18mA for low/high linearity mode from 2.1V supply. The performance compliance is given in Table 5.1.

Appendix A

Common-Source Amplifier Volterra Kernel Derivation

In this appendix, a complete derivation of the CS amplifier Volterra kernels is given. The KCL equations for each node of the circuit in Fig. 2.6 are

$$\frac{v_{\rm x}-v_{\rm g}}{Z_1(s)}-sC_{\rm gd}\cdot v_{\rm gd}-sC_{\rm gs}\cdot v_{\rm gs}=0 \tag{A.1a}$$

$$i_{\rm d}-sC_{\rm gd}\cdot v_{\rm gd}-i_{\rm out}=0 \tag{A.1b}$$

$$i_{\rm d}+sC_{\rm gs}\cdot v_{\rm gs}-\frac{Z_{\rm S}(s)}{v_{\rm s}}=0 \tag{A.1c}$$

where $i_{\rm d}$, $i_{\rm out}$, $v_{\rm gs}$, and $v_{\rm gd}$ are defined by (2.4), (2.5), (2.6a), and (2.6b), respectively. The solution of (A.1) for $v_{\rm x}$ is

$$v_{\rm x}=[(Z_1(s)+Z_{\rm S}(s))\cdot b(s)+1]\cdot v_{\rm gs}+Z_1(s)a(s)\cdot v_{\rm gd}+Z_{\rm S}(s)\cdot i_{\rm d} \tag{A.2}$$

where, $a(s)$=$sC_{\rm gd}$ and $b(s)$=$sC_{\rm gs}$. Now, the gate-drain voltage($v_{\rm gd}$) can be written as

$$v_{\rm gd}=\frac{[Z_{\rm S}(s)b(s)+1]\cdot v_{\rm gs}+[Z_{\rm S}(s)+Z_{\rm L}(s)]\cdot i_{\rm d}}{1+Z_{\rm L}(s)a(s)} \tag{A.3}$$

Inserting (2.5), (2.6a), and (2.6b) into (A.2) and (A.3) and exciting the circuit with a single tone, $v_{\rm x}=e^{st}$, the linear transfer function of $v_{\rm gd}$, $B_1(s)$, can be evaluated for e^{st} from (A.2) and (A.3).

$$B_1(s)=\frac{1-A_1(s)\cdot[b(s)\cdot(Z_1(s)+Z_{\rm S}(s))+g_1Z_{\rm S}(s)+1]}{Z_1(s)a(s)} \tag{A.4a}$$

$$B_1(s)=\frac{A_1(s)\cdot[Z_{\rm S}(s)b(s)+g_1\cdot(Z_{\rm S}(s)+Z_{\rm L}(s))+1]}{1+Z_{\rm L}(s)a(s)} \tag{A.4b}$$

Since (A.4a) and (A.4b) are two different expressions for $B_1(s)$ and both contain $A_1(s)$, the $A_1(s)$ can be derived by setting (A.4a) = (A.4b). So,

$$A_1(s) = \frac{1}{g_1 + g(s)} \cdot \frac{1 + Z_{\mathrm{L}}(s)a(s)}{Z_{\mathrm{x}}(s)}, \tag{A.5}$$

where

$$g(s) = \frac{1 + a(s) \cdot (Z_1(s) + Z_{\mathrm{L}}(s)) + b(s) \cdot (Z_1(s) + Z_{\mathrm{x}}(s))}{Z_{\mathrm{x}}(s)} \tag{A.6a}$$

$$Z_{\mathrm{x}}(s) = Z_{\mathrm{S}}(s) + a(s) \cdot Z_{123}(s) \tag{A.6b}$$

$$Z_{123}(s) = Z_1(s)Z_{\mathrm{L}}(s) + Z_{\mathrm{S}}(s)Z_{\mathrm{L}}(s) + Z_{\mathrm{S}}(s)Z_1(s) \tag{A.6c}$$

By following the same procedures with a two-tone excitation, $v_{\mathrm{x}} = e^{s_1 t} + e^{s_2 t}$, and evaluating for $e^{(s_1+s_2)t}$, the second-order Volterra kernels, $A_2(s_1, s_2)$ and $B_2(s_1, s_2)$, can be found as (A.7) and (A.8), respectively.

$$A_2(s_1, s_2) = \frac{-1}{g_1 + g(s_1 + s_2)} \cdot (g_2 A_1(s_1)A_1(s_2)) \tag{A.7}$$

$$\begin{aligned} &B_2(s_1, s_2) = \\ &\{A_2(s_1, s_2) \cdot [Z_{\mathrm{S}}(s_1 + s_2)b(s_1 + s_2) + g_1 \cdot (Z_{\mathrm{S}}(s_1 + s_2) + Z_{\mathrm{L}}(s_1 + s_2)) + 1] + \\ &g_2 A_1(s_1)A_1(s_2) \cdot [Z_{\mathrm{S}}(s_1 + s_2) + Z_{\mathrm{L}}(s_1 + s_2)]\} \,/\, \{1 + Z_{\mathrm{L}}(s_1 + s_2)a(s_1 + s_2)\} \end{aligned} \tag{A.8}$$

With a three-tone excitation, $v_{\mathrm{x}} = e^{s_1 t} + e^{s_2 t} + e^{s_3 t}$, and evaluating for $e^{(s_1+s_2+s_3)t}$, the third-order Volterra kernels, $A_3(s_1, s_2, s_3)$ and $B_3(s_1, s_2, s_3)$, can be found as (A.9) and (A.10), respectively.

$$A_3(s_1, s_2, s_3) = \frac{-1}{g_1 + g(s_{1,2,3})} \cdot \left[2g_2 \overline{A_1(s_1)A_2(s_2, s_3)} + g_3 A_1(s_1)A_1(s_2)A_1(s_3)\right], \tag{A.9}$$

$$\begin{aligned} &B_3(s_1, s_2, s_3) = \\ &\Big\{ - A_3(s_1, s_2, s_3) \cdot [b(s_{1,2,3}) \left(Z_1(s_{1,2,3}) + Z_{\mathrm{S}}(s_{1,2,3})\right) + g_1 Z_{\mathrm{S}}(s_{1,2,3}) + 1] \\ &- Z_{\mathrm{S}}(s_{1,2,3}) \cdot \left[2g_2 \overline{A_1(s_1)A_2(s_2, s_3)} + g_3 A_1(s_1)A_1(s_2)A_1(s_3)\right] \Big\} \Big/ \{Z_1(s_{1,2,3})a(s_{1,2,3})\} \end{aligned} \tag{A.10}$$

where $s_{1,2,3}$ means $s_1 + s_2 + s_3$. The overbar in (A.9) and (A.10) indicates the symmetrization of all possible permutations of the Laplace variables [48], i.e.

$$\overline{A_1(s_1)A_2(s_2,s_3)} = \frac{1}{3}\left[A_1(s_1)A_2(s_2,s_3) + A_1(s_2)A_2(s_1,s_3) + A_1(s_3)A_2(s_1,s_2)\right] \tag{A.11}$$

For the IM_3 test case, (A.11) can be simplified to (A.12), since $s_1 = s_2 = j\omega_2$ and $s_3 = -j\omega_1$ for $2\omega_2 - \omega_1$, and $s_1 = s_2 = j\omega_1$ and $s_3 = -j\omega_2$ for $2\omega_1 - \omega_2$, and

$$\overline{A_1(j\omega_2)A_2(j\omega_2,-j\omega_1)} = \frac{1}{3}\left[2A_1(j\omega_2)A_2(j\omega_2,-j\omega_1) + A_1(-j\omega_1)A_2(j\omega_2,j\omega_2)\right] \tag{A.12a}$$

$$\overline{A_1(j\omega_1)A_2(j\omega_1,-j\omega_2)} = \frac{1}{3}\left[2A_1(j\omega_1)A_2(j\omega_1,-j\omega_2) + A_1(-j\omega_2)A_2(j\omega_1,j\omega_1)\right] \tag{A.12b}$$

Inserting (A.5) and (A.7) into (A.12),

$$\overline{A_1(j\omega_2)A_2(j\omega_2,-j\omega_1)} = -\frac{1}{3}\cdot g_2 A_1^2(j\omega_2)A_1(-j\omega_1)\cdot \left[\frac{2}{g_1 + g(j\omega_2 - j\omega_1)} + \frac{1}{g_1 + g(j2\omega_2)}\right] \tag{A.13a}$$

$$\overline{A_1(j\omega_1)A_2(j\omega_1,-j\omega_2)} = -\frac{1}{3}\cdot g_2 A_1^2(j\omega_1)A_1(-j\omega_2)\cdot \left[\frac{2}{g_1 + g(j\omega_1 - j\omega_2)} + \frac{1}{g_1 + g(j2\omega_1)}\right] \tag{A.13b}$$

The third-order Volterra kernel, $A_3(j\omega_2, j\omega_2, -j\omega_1)$, can be expressed as

$$A_3(j\omega_2, j\omega_2, -j\omega_1) = \frac{-1}{g_1 + g(j\omega_{1,2,3})} A_1^2(j\omega_2)A_1(-j\omega_1)\cdot\epsilon\left(j\omega_2 - j\omega_1, j2\omega_2\right) \tag{A.14}$$

where

$$\epsilon\left(j\omega_2 - j\omega_1, j2\omega_2\right) = g_3 - \frac{2}{3}g_2^2\cdot \times \left[\frac{2}{g_1 + g(j\omega_2 - j\omega_1)} + \frac{1}{g_1 + g(j2\omega_2)}\right] \tag{A.15}$$

Commuting $j\omega_2$ with $j\omega_1$, the expression for $A_3(j\omega_1, j\omega_1, -j\omega_2)$ can be done due to the symmetrization of Volterra kernel.

Using (A.1b) with the equations above and the harmonic excitation method as before, the third-order Volterra kernel of the final output can be found.

$$C_3(j\omega_2, j\omega_2, -j\omega_1) = A_1^2(j\omega_2) \cdot A_1(-j\omega_1) \\ \times \left[\frac{1}{g_1 + g(j2\omega_2 - j\omega_1)} \cdot \frac{\alpha(j2\omega_2 - j\omega_1)}{Z_{\mathrm{x}}(j2\omega_2 - j\omega_1)} \right] \cdot \epsilon\left(j\omega_2 - j\omega_1, j2\omega_2\right) \tag{A.16}$$

where

$$\alpha(j\omega) = b(j\omega) \cdot [Z_1(j\omega) + Z_{\mathrm{S}}(j\omega)] + a(j\omega) Z_1(j\omega) + 1 \tag{A.17}$$

Appendix B

Common-Gate Amplifier Volterra Kernel Derivation

In this appendix, the complete derivation of the CG amplifier Volterra kernels will be given with the direct voltage method. The KCL equation for $v_{\rm s}$ in the circuit of Fig. 2.11(b) is

$$i_{\rm d} = \frac{v_{\rm s} - v_{\rm x}}{R_{\rm S}} + \left(sC_{\rm gs} + \frac{1}{Z_{\rm S}(s)} \right) \cdot v_{\rm s} \tag{B.1}$$

where, $i_{\rm d}$ can be defined by (2.4) and $v_{\rm gs} = -v_{\rm s}$ can be defined by (2.6a). Again, $i_{\rm out}(v_{\rm x})$ is expressed by (2.5). From (B.1), the expression of $v_{\rm gs}$ is given by

$$v_{\rm gs} = -v_{\rm s} = -\frac{v_{\rm x} + i_{\rm d} \cdot R_{\rm S}}{1 + a(s) \cdot R_{\rm S}} \tag{B.2}$$

where

$$a(s) = sC_{\rm gs} + \frac{1}{Z_{\rm S}(s)} \tag{B.3}$$

Inserting (2.4) and (2.6a) into (B.2) and following the same method used in the CS amplifier case, the $A_1(s), A_2(s_1, s_2)$ and $A_3(s_1, s_2, s_3)$ can be found.

$$A_1(s) = \frac{-1}{1 + R_{\rm S} \cdot [a(s) + g_1]} \tag{B.4a}$$

$$A_2(s_1, s_2) = A_1(s_1 + s_2) \cdot R_{\rm S} \cdot g_2 A_1(s_1) A_1(s_2) \tag{B.4b}$$

$$A_3(s_1, s_2, s_3) = A_1(s_{1,2,3}) \cdot R_{\rm S} \cdot \Big[2g_2 \cdot \overline{A_1(s_1) A_2(s_2, s_3)} + g_3 \cdot A_1(s_1) A_1(s_2) A_1(s_3) \Big] \tag{B.4c}$$

For the IM_3 calculation of the $2\omega_2-\omega_1$ case, substituting $s_1 = s_2 = j\omega_2$ and $s_3 = -j\omega_1$,

$$A_3(j\omega_2, j\omega_2, -j\omega_1) = A_1(j2\omega_2 - j\omega_1)\cdot R_{\mathrm{S}} \cdot A_1^2(j\omega_2)A_1(-j\omega_1)\cdot \times \epsilon(j\omega_2 - j\omega_1, j2\omega_2) \tag{B.5}$$

where

$$\epsilon(j\omega_2 - j\omega_1, j2\omega_2) = g_3 + \frac{2}{3}R_{\mathrm{S}} \cdot g_2^2 \left[2A_1(j\omega_2 - j\omega_1) + A_1(j2\omega_2)\right] \tag{B.6}$$

The symmetrization of the Volterra kernel holds in the CG case, as in the CS case. By commuting $j\omega_2$ with $j\omega_1$, $A_3(j\omega_1, j\omega_1, -j\omega_2)$ can be expressed.

By setting $i_{\mathrm{d}}(v_{\mathrm{gs}}) = i_{\mathrm{out}}(v_{\mathrm{x}})$, the third-order Volterra kernel of the output is

$$C_3(j\omega_2, j\omega_2, -j\omega_1) = A_1^2(j\omega_2) \cdot A_1(-j\omega_1) \times \left[1 + g_1 \cdot R_{\mathrm{S}} \cdot A_1(j2\omega_2 - j\omega_1)\right] \cdot \epsilon(j\omega_2 - j\omega_1, j2\omega_2) \tag{B.7}$$

Appendix C

Cross-coupled Differential APD LNA Channel Noise Transfer Function Derivation

In this appendix, The channel noise transfer function in the high-linearity mode will be derived from Fig. 2.19. The source voltage v_{s} can be expressed as a function of i_{out}.

$$v_{\mathrm{s}} = \frac{\left[1-\omega^2 C_{\mathrm{gs},1} L_{\mathrm{g}} + j\omega C_{\mathrm{gs},1} R_{\mathrm{S}}\right] \cdot \left[1 + 2 g_{\mathrm{m},3} Z_{\mathrm{L}}\left(j\omega\right)\right] \cdot j\omega L_{\mathrm{S}}}{1-\omega^2 C_{\mathrm{gs},1}\left(L_{\mathrm{S}}+L_{\mathrm{g}}\right) + j\omega C_{\mathrm{gs},1} R_{\mathrm{S}} + 2 j\omega L_{\mathrm{S}} g_{\mathrm{m},3}\left[1-\omega^2 C_{\mathrm{gs},1} L_{\mathrm{g}} + j\omega C_{\mathrm{gs},1} R_{\mathrm{S}}\right]} \times i_{\mathrm{out}} \tag{C.1}$$

Inserting (C.1) and $v_{\mathrm{gs},1} = i_{\mathrm{in}} \cdot \left(1 \Big/ j\omega \cdot C_{\mathrm{gs},1}\right)$ into the i_{out} nodal equation, the noise transfer function of M1's channel noise in the high-linearity mode can be obtained as

$$\overline{i^2_{\mathrm{ndHL,o}}} = \left| \frac{B\left(j\omega\right)}{\Delta(j\omega)\left(1+g_{\mathrm{m},3}Z_{\mathrm{L}}(j\omega)\right)+j\omega L_{\mathrm{S}}g_{\mathrm{m},3}\left[1-\omega^2 C_{\mathrm{gs},1}L_{\mathrm{g}}+g_{\mathrm{m},1}Z_{\mathrm{L}}(j\omega)+j\omega C_{\mathrm{gs},1}R_{\mathrm{S}}\right]} \right|^2 \times \overline{i^2_{\mathrm{nd}}} \tag{C.2a}$$

$$B\left(j\omega\right) = 1-\omega^2 C_{\mathrm{gs},1}\left(L_{\mathrm{S}}+L_{\mathrm{g}}\right)+j\omega C_{\mathrm{gs},1}R_{\mathrm{S}}+2j\omega L_{\mathrm{S}}g_{\mathrm{m},3}\cdot\left[1-\omega^2 C_{\mathrm{gs},1}L_{\mathrm{g}}+j\omega C_{\mathrm{gs},1}R_{\mathrm{S}}\right] \tag{C.2b}$$

$$\Delta\left(j\omega\right) = 1-\omega^2 C_{\mathrm{gs},1}\cdot\left(L_{\mathrm{s}}+L_{\mathrm{g}}\right)+j\omega\cdot\left(C_{\mathrm{gs},1}R_{\mathrm{s}}+L_{\mathrm{s}}g_{\mathrm{m},1}\right) \tag{C.2c}$$

Similarly, the noise transfer function of $i_{\mathrm{nd},3}$ and $i_{\mathrm{nd},4}$ can be obtained as

$$\overline{i^2_{\mathrm{nd3,o}}} = \left| \frac{B\left(j\omega\right)+k\left(j\omega\right)}{B\left(j\omega\right)\left(1+g_{\mathrm{m},3}\cdot Z_{\mathrm{L}}(j\omega)\right)-k\left(j\omega\right)\cdot\left[1+2g_{\mathrm{m},3}\cdot Z_{\mathrm{L}}\left(j\omega\right)\right]} \right|^2 \cdot \overline{i^2_{\mathrm{nd3}}} \tag{C.3a}$$

$$\overline{i^2_{\mathrm{nd4,o}}} = \left| \frac{k\left(j\omega\right)}{B\left(j\omega\right)\left(1+g_{\mathrm{m},3}\cdot Z_{\mathrm{L}}(j\omega)\right)-k\left(j\omega\right)\cdot\left[1+2g_{\mathrm{m},3}\cdot Z_{\mathrm{L}}\left(j\omega\right)\right]} \right|^2 \cdot \overline{i^2_{\mathrm{nd4}}} \tag{C.3b}$$

$$k\left(j\omega\right) = j\omega L_{\mathrm{s}}\cdot\left[g_{\mathrm{m},3}-g_{\mathrm{m},1}+g_{\mathrm{m},3}\cdot\left(j\omega\cdot C_{\mathrm{gs},1}\cdot R_{\mathrm{s}}-\omega^2\cdot C_{\mathrm{gs},1}\cdot L_{\mathrm{g}}\right)\right] \tag{C.3c}$$

References

[1] V. Aparin, G. J. Ballantyne, C. J. Persico, and A. Cicalini, "An integrated LMS adaptive filter of TX leakage for CDMA receiver front ends," *IEEE J. Solid-State Circuits*, vol. 41, no. 5, pp. 1171–1182, May 2006.

[2] V. Aparin, "A new method of TX leakage cancellation in W/CDMA and GPS receivers," in *Proc. IEEE RFIC Symp.*, 2008.

[3] Y. Wu, X. Ding, M. Ismail, and H. Olsson, "RF bandpass filter design based on CMOS active inductors," *IEEE Trans. Circuits Syst. II*, vol. 50, no. 12, pp. 942 – 949, Dec. 2003.

[4] H. Khatri, P. S. Gudem, and L. E. Larson, "A SAW-less CMOS CDMA receiver with active Tx filtering," in *Proc. IEEE CICC*, 13-16 2009, pp. 379 –382.

[5] *Recommended Minimum Performance Standards for cdma2000 Spread Spectrum Mobile Stations, 3GPP2 C.S0011-B, 2002*.

[6] V. Aparin, N. Kim, G. Brown, Y. Wu, A. Cicalini, S. Kwok, and C. Persico, "A fully-integrated highly linear zero-IF CMOS cellular CDMA receiver," in *IEEE ISSCC Dig. Tech. Papers*, 2005, pp. 324 – 325.

[7] B. Razavi, "Design considerations for direct-conversion receivers," *IEEE Trans. Circuits Syst. II*, vol. 44, no. 6, pp. 428–435, Jun. 1997.

[8] H. Waite, P. Ta, J. Chen, H. Li, M. Gao, C. S. Chang, Y. S. Chang, W. Redman-White, O. Charlon, Y. Fan, R. Perkins, D. Brunel, E. Soudee, N. Lecacheur, and S. Clamagirand, "A CDMA 2000 zero-IF receiver with low-leakage integrated front-end," *IEEE J. Solid-State Circuits*, vol. 39, no. 7, pp. 1175–1179, Jul. 2004.

[9] V. Aparin and L. Larson, "Analysis and reduction of cross-modulation distortion in CDMA receivers," *IEEE Trans. Microw. Theory Tech.*, vol. 51, no. 5, pp. 1591–1602, May 2003.

[10] T. Werth, C. Schmits, R. Wunderlich, and S. Heinen, "An Active Feedback Interference Cancellation Technique for Blocker Filtering in RF Receiver Front-Ends," *IEEE J. Solid-State Circuits*, vol. 45, no. 5, pp. 989 –997, May 2010.

[11] A. Safarian, A. Shameli, A. Rofougaran, M. Rofougaran, and F. De Flaviis, "Integrated Blocker Filtering RF Front Ends," in *Proc. IEEE RFIC Symp.*, 3-5 2007, pp. 13 –16.

[12] H. Darabi, "A blocker filtering technique for saw-less wireless receivers," *IEEE J. Solid-State Circuits*, vol. 42, no. 12, pp. 2766 –2773, Dec. 2007.

[13] A. Mirzaei and H. Darabi, "A low-power wcdma transmitter with an integrated notch filter," *IEEE J. Solid-State Circuits*, vol. 43, no. 12, pp. 2868 –2881, Dec. 2008.

[14] H. Khatri, P. S. Gudem, and L. E. Larson, "Integrated RF interference suppression filter design using bond-wire inductors," *IEEE Trans. Microw. Theory Tech.*, vol. 56, no. 5, pp. 1024–1034, May 2008.

[15] T. Soorapanth and S. Wong, "A 0-dB IL 2140±30 MHz bandpass filter utilizing Q-enhanced spiral inductors in standard CMOS," *IEEE J. Solid-State Circuits*, vol. 37, no. 5, pp. 579 –586, May 2002.

[16] F. Dulger, E. Sanchez-Sinencio, and J. Silva-Martinez, "A 1.3-V 5-mW fully integrated tunable bandpass filter at 2.1 GHz in 0.35μm CMOS," *IEEE J. Solid-State Circuits*, vol. 38, no. 6, pp. 918 – 928, Jun. 2003.

[17] W. Kuhn, F. Stephenson, and A. Elshabini-Riad, "Dynamic range of high-Q OTA-C and enhanced-Q LC RF bandpass filters ," in *Proceedings of the 37th Midwest Symposium on Circuits and Systems*, vol. 2, 3-5 1994, pp. 767 –771 vol.2.

[18] *CDMA 2000 Standard TIA/EIA IS-2000 Series Rev. A.*

[19] B. Razavi, *RF Microelectronics*. Prentice Hall, 1998.

[20] T. H. Lee, *The Design of CMOS Radio-Frequency Integrated Circuits*. Cambridge University Press, 1998.

[21] A. Parsa and B. Razavi, "A new transceiver architecture for the 60-GHz band," *IEEE J. Solid-State Circuits*, vol. 44, no. 3, pp. 751–762, Mar. 2009.

[22] S. Pinel, S. Sarkar, P. Sen, B. Perumana, D. Yeh, D. Dawn, and J. Laskar, "A 90nm CMOS 60GHz radio," in *IEEE ISSCC Dig. Tech. Papers*, 2008, pp. 129 – 130.

[23] P. Gray and R. Meyer, "Future directions in silicon ICs for RF personal communications," in *Proc. IEEE CICC*, 1998, pp. 83 – 90.

[24] A. Liscidini, M. Brandolini, D. Sanzogni, and R. Castello, "A 0.13μm CMOS front-end, for DCS1800/UMTS/802.11b-g with multiband positive feedback low-noise amplifier," *IEEE J. Solid-State Circuits*, vol. 41, no. 4, pp. 981–989, Apr. 2006.

[25] J. Goo, H. Ahn, D. Ladwig, Z. Yu, T. Lee, and R. Dutton, "A noise optimization technique for integrated low-noise amplifiers," *IEEE J. Solid-State Circuits*, vol. 37, no. 8, pp. 994–1002, Aug. 2002.

[26] D. Shaeffer and T. Lee, "A 1.5-V, 1.5-GHz CMOS low noise amplifier," *IEEE J. Solid-State Circuits*, vol. 32, no. 5, pp. 745–759, May 1997.

[27] T. Nguyen, C. Kim, G. Ihm, M. Yang, and S. Lee, "CMOS low-noise amplifier design optimization techniques," *IEEE Trans. Microw. Theory Tech.*, vol. 52, no. 5, pp. 1433–1442, May 2004.

[28] N. Kim, L. Larson, and V. Aparin, "A highly linear SAW-less CMOS receiver using a mixer with embedded Tx filtering for CDMA," *IEEE J. Solid-State Circuits*, vol. 44, no. 8, pp. 2126–2137, Aug. 2009.

[29] B. Toole, C. Plett, and M. Cloutier, "RF circuit implications of moderate inversion enhanced linear region in MOSFETs," *IEEE Trans. Circuits Syst. I*, vol. 51, no. 2, pp. 319–328, Feb. 2004.

[30] R. Baki, T. Tsang, and E.-G. M.N., "Distortion in RF CMOS short-channel low-noise amplifiers," *IEEE Trans. Microw. Theory Tech.*, vol. 54, no. 1, pp. 46–56, Jan. 2006.

[31] X. Wei, G. Niu, Y. Li, M. Yang, and S. Taylor, "Modeling and characterization of intermodulation linearity on a 90-nm RF CMOS technology," *IEEE Trans. Microw. Theory Tech.*, vol. 57, no. 4, pp. 965–971, Apr. 2009.

[32] P. Wambacq, G. Gielen, P. Kinget, and W. Sansen, "High-frequency distortion analysis of analog integrated circuits," *IEEE Trans. Circuits Syst. II*, vol. 46, no. 3, pp. 335–345, Mar. 1999.

[33] N. Kim, V. Aparin, K. Barnett, and C. Persico, "A cellular-band CDMA 0.25 μ CMOS LNA linearized using active post-distortion," *IEEE J. Solid-State Circuits*, vol. 41, no. 7, pp. 1530–1534, Jul. 2006.

[34] V. Aparin and L. Larson, "Modified derivative superposition method for linearizing FET low-noise amplifiers," *IEEE Trans. Microw. Theory Tech.*, vol. 53, no. 2, pp. 571–581, Feb. 2005.

[35] B. Kim, J. Ko, and K. Lee, "Highly linear CMOS RF MMIC amplifier using multiple gated trasistors and its Volterra series analysis," in *IEEE MTT-S Int. Microw. Symp. Dig.*, 2001, pp. 515 – 518.

[36] H. Zhang, X. Fan, and E. Sanchez-Sinencio, "A low-power, linearized, ultra-wideband LNA design technique," *IEEE J. Solid-State Circuits*, vol. 44, no. 2, pp. 320–330, Feb. 2009.

[37] S. Ganensan, E. Sanchez-Sinencio, and J. Silva-Martinez, "A highly linear low-noise amplifier," *IEEE Trans. Microw. Theory Tech.*, vol. 54, no. 12, pp. 4079–4085, Dec. 2006.

[38] W. Chen, G. Liu, B. Zdravko, and A. Niknejad, "A highly linear broadband CMOS LNA employing noise and distortion cancellation," *IEEE J. Solid-State Circuits*, vol. 43, no. 5, pp. 1164–1176, May 2008.

[39] C. Wang, G. Vaidyanathan, and L. Larson, "A capacitance-compensation technique for improved linearity in CMOS class-AB power amplifiers," *IEEE J. Solid-State Circuits*, vol. 39, no. 11, pp. 1927–1937, Nov. 2004.

[40] V. Aparin, G. Brown, and L. Larson, "Linearization of CMOS LNA's via optimum gate biasing," in *IEEE Int. Symp. Circuits Syst.*, 2004, pp. 748 – 751.

[41] H. Park and S. Hong, "Characterization and modeling of intermodulation distortion asymmetry in HBT using large-signal model," in *IEEE MTT-S Int. Microw. Symp. Dig.*, 2003, pp. 773 – 776.

[42] I. Takenaka, K. Ishikura, H. Takahashi, K. Hasegawa, K. Asano, and N. Iwata, "Improvement of intermodulation distortion asymmetry characteristics with wideband microwave signals in high power amplifiers," *IEEE Trans. Microw. Theory Tech.*, vol. 56, no. 6, pp. 1355–1363, Jun. 2008.

[43] J. Kenney and P. Fedorenko, "Identification of RF power amplifier memory effect origins using third-order intermodulation distortion amplitude and phase asymmetry," in *IEEE MTT-S Int. Microw. Symp. Dig.*, 2006, pp. 1121 – 1124.

[44] N. Carvalho and J. Pedro, "Two-tone asymmetry in microwave power amplifiers," in *IEEE MTT-S Int. Microw. Symp. Dig.*, 2000, pp. 445 – 448.

[45] P. Colantonio, F. Giannini, E. Limiti, and A. Nanni, "Investigation of IMD asymmetry in microwave FETs via Volterra series," in *Gallium Arsenide and Other Semiconductor Application Symposium, 2005. EGAAS 2005. European*, Oct. 2005, pp. 53 – 56.

[46] P. Wanbacq and W. Sansen, *Distortion Analysis of Analog Integrated Circuits*. Kluwer Academic Piblishers, 1998.

[47] S. Mass, *Nonlinear Microwave Circuits*. Artech house, 1988.

[48] M. Schetzen, *The Volterra and Wiener Theories of Nonlinear Systems*. Wiley, 1980.

[49] T. Kim, "A common-gate amplifier with transconductance nonlinearity cancellation and its high-frequency analysis using the Volterra series," *IEEE Trans. Microw. Theory Tech.*, vol. 57, no. 6, pp. 1461–1469, Jun. 2009.

[50] A. Abidi, "Direct-conversion radio transceivers for digital communications," *IEEE J. Solid-State Circuits*, vol. 30, no. 12, pp. 1390–1410, Dec. 1995.

[51] D. Manstretta, R. Castello, and F. Svelto, "Low 1/f noise CMOS active mixers for direct conversion," *IEEE Trans. Circuits Syst. II*, vol. 48, no. 9, pp. 846–850, Sep. 2001.

[52] H. Darabi and J. Chiu, "A noise cancellation technique in active RF-CMOS Mixers," *IEEE J. Solid-State Circuits*, vol. 40, no. 12, pp. 2628–2632, Dec. 2005.

[53] T. Melly, A. Porret, C. Enz, and E. Vittoz, "An analysis of flicker noise rejection in low-power low-voltage CMOS mixers," *IEEE J. Solid-State Circuits*, vol. 36, no. 1, pp. 102–109, Jan. 2001.

[54] A. van der Ziel, *Noise in Solid State Devices and Circuits*. New York:Wiley, 1986.

[55] D. Shaeffer and T. Lee, "A 1.5V, 1.5-GHz CMOS low noise amplifier," *IEEE J. Solid-State Circuits*, vol. 32, no. 5, pp. 745–759, May 1997.

[56] H. Darabi and A. Abidi, "Noise in RF-CMOS mixers: a simple physical model," *IEEE J. Solid-State Circuits*, vol. 35, no. 1, pp. 15–25, Jan. 2000.

[57] J. Crols and M. Steyaert, "A 1.5V highly linear CMOS downconversion mixer," *IEEE J. Solid-State Circuits*, vol. 30, no. 7, pp. 736–742, Jul. 1995.

[58] W. Redman-White and D. Leenaerts, "1/f Noise in passive CMOS mixers for low and zero IF integrated receivers," in *Proc. 27th Eur. Solid-State Circ. Conf.*, 2001, pp. 18–20.

[59] R. Bagheri, A. Mirzaei, S. Chehrazi, M. Heidari, M. Lee, M. Mikhemar, W. Tang, and A. Abidi, "An 800-MHz-6-GHz software-defined wireless receiver in 90-nm CMOS," *IEEE J. Solid-State Circuits*, vol. 41, no. 12, pp. 2860–2876, Dec. 2006.

[60] S. Zhou and M.-C. Chang, "A CMOS passive mixer with low flicker noise for low-power direct-conversion receiver," *IEEE J. Solid-State Circuits*, vol. 40, no. 5, pp. 1084–1093, May 2005.

[61] B. Cook, A. Berny, A. Molnar, S. Lanzisera, and K. Pister, "Low-power 2.4-GHz transceiver with passive Rx front-end and 400-mV supply," *IEEE J. Solid-State Circuits*, vol. 41, no. 12, pp. 2757–2766, Dec. 2006.

[62] J. Zhan, B. R. Carlton, and S. S. Taylor, "Low-Cost Direct Conversion RF Front-Ends in Deep Submicron CMOS," in *Proc. IEEE RFIC Symp.*, 2007.

[63] F. Behbahani, Y. Kishigami, J. Leete, and A. Abidi, "CMOS mixers and polyphase filters for large image rejection," *IEEE J. Solid-State Circuits*, vol. 36, no. 6, pp. 873–887, Jun. 2001.

[64] T. Nguyen, V. Krizhanovskii, J. Lee, S. Han, S. Lee, N. Kim, and C. Pyo, "A low power RF direct-conversion receiver/transmitter for 2.4-GHz-band IEEE 802.15.4 standard in 0.18-μ m CMOS technology," *IEEE Trans. Microw. Theory Tech.*, vol. 54, no. 12, pp. 4062–4071, Dec. 2006.

[65] M. Valla, G. Montagna, R. Castello, R. Tonietto, and I. Bietti, "A 72-mW CMOS 802.11a direct conversion front-end with 3.5dB NF and 200-kHz 1/f noise corner," *IEEE J. Solid-State Circuits*, vol. 40, no. 4, pp. 970–977, Apr. 2005.

[66] N. Kim, V. Aparin, and L. Larson, "A resistively degenerated wide-band passive mixer with low noise figure and +60dBm IIP2 in 0.18μ m CMOS," in *Proc. IEEE RFIC Symp.*, 2008.

[67] D. Manstretta, M. Brandolini, and F. Svelto, "Second-order intermodulation mechanisms in CMOS downconverters," *IEEE J. Solid-State Circuits*, vol. 38, no. 3, pp. 394–406, Mar. 2003.

[68] C. Galup-Montoro, M. Schneider, H. Klimach, and A. Arnaud, "A compact model of MOSFET mismatch for circuit design," *IEEE J. Solid-State Circuits*, vol. 40, no. 8, pp. 1649–1657, Aug. 2005.

[69] W. Zhuo, S. Shekhar, S. Embabi, J. Gyvez, D. Allstot, and E. Sanchez-Sinencio, "A capacitor cross-coupled common-gate low-noise amplifier," *IEEE Trans. Circuits Syst. II*, vol. 52, no. 12, pp. 875–879, Dec. 2005.

[70] S. Wang, A. Niknejad, and R. Brodersen, "Design of a sub-mW 960-MHz UWB CMOS LNA," *IEEE J. Solid-State Circuits*, vol. 41, no. 11, pp. 2449–2456, Nov. 2006.

[71] N. Poobuapheun, W.-H. Chen, Z. Boos, and A. Niknejad, "A 1.5V 0.7-2.5-GHz CMOS quadrature demodulator for multiband direct-conversion receivers," *IEEE J. Solid-State Circuits*, vol. 42, no. 8, pp. 1669–1677, Aug. 2007.

[72] W. Mumford and E. H. Scheibe, *Noise Performance Factors in Communication Systems*. Horizon House-Microwave, 1967.

[73] M. Ortmanns, F. Gerfers, and Y. Manoli, "A continuous-time $\sum \Delta$ modulator with reduced sensitivity to clock jitter through SCR feedback," *IEEE Trans. Circuits Syst. I*, vol. 52, no. 5, pp. 875–884, May 2005.

[74] R. Baker, *CMOS Mixed-Signal Circuit Design*. New York:Wiley-Interscience, 2002.